Technische Universität Dresden
Bereich Mathematik und Naturwissenschaften
Fakultät Physik

Institut für Kern- und Teilchenphysik
Experimentelle Teilchenphysik

Master-Arbeit
zur Erlangung des Hochschulgrades
Master of Science
im Studiengang
Master-Studiengang Physik

Search for a light CP-odd Higgs boson decaying into a pair of tau-leptons

vorgelegt von
Jannik Friese
geboren am 08.04.1996 in Halberstadt

eingereicht am 30.09.2022

Erstgutachter: Prof. Dr. Arno Straessner
Zweitgutachter: Prof. Dr. Dominik Stöckinger

Abstract

This thesis presents an analysis for the search of a light CP-odd Higgs boson at the ATLAS detector. The Higgs boson is part of an additional Higgs doublet, which was introduced with the two-Higgs-Doublet Model (2HDM). This is an extension of the Standard Model of particle physics and could explain the deviation between theoretical predictions and experimental measurements of the anomalous magnetic moment of the muon.

In this connection the decay $A \to \tau\tau$ with Higgs masses between $m_A = 20\,\mathrm{GeV}$ and $m_A = 90\,\mathrm{GeV}$ is considered. In the analysis only the decay of the two τ leptons into one electron and one muon is analyzed, since this grants a large suppression of background proccesses.

The utilized data was recorded by the ATLAS detector in Run-2 of the LHC. Here an integrated luminosity of $139\mathrm{fb}^{-1}$ was achieved.

This thesis presents a data-driven method to estimate QCD background. Additionally the application of neral networks for event classification was implemented. This classification aims to optimize the signal-to-background ratio.

Zusammenfassung

Diese Arbeit stellt eine Analyse zur Suche eines leichten CP ungeraden Higgs Bosons am ATLAS Detektor vor. Das gesuchte Higgs Teilchen ist Teil eines zusätzlichen Higgs Dubletts, welches im Rahmen des Zwei-Higgs-Dublett Modells (2HDM) eingeführt wurde. Dieses ist eine Erweiterung des Standard Models der Teilchenphysik und könnte die Abweichung zwischen theoretischer Vorhersage und experimentellen Messung des anormalen magnetischen Moment des Myons erklären.

Hierbei wird der Zerfall $A \to \tau\tau$ des zusätzlichen Higgs Teilchen betrachtet mit Massen von $m_A = 20\,\mathrm{GeV}$ bis $m_A = 90\,\mathrm{GeV}$. Beim Zerfall der τ Leptonen wird der Endzustand von einem Elektron und ein Myon analysiert, da dies eine starke Untergrundunterdrückung gewährt.

Die verwendeten Daten wurden mithilfe des ATLAS Detektors während des Run-2 des LHC aufgenommen. Dabei wurde eine integrierte Luminosität von $139\mathrm{fb}^{-1}$ erreicht.

In dieser Arbeit wurde eine datengetriebene Untergrundabschätzung des QCD Untergrundes entwickelt. Außerdem wurde die Anwendung von neuronalen Netzen zur Eventklassifizierung implementiert. Diese Klassifizierung dient dazu weitere Verbesserungen des Signal zu Untergrund Verhältnisses zu erzielen.

Contents

1. Introduction

The field of modern particle is a rather new field of physics. Its foundation was set by J.J. Thompson and other physicists. They were responsible for the discovery of the first elementary particle, the electron in 1897 [1]. Further measurements of its charge were done by R.A. Milikan and H.Fletcher in 1909 [2]. The second subatomic particle, the muon, was discovered 40 years after the discovery of the electron [3]. Again almost 40 years later the third lepton was observed at the Stanford Linear Accelerator Center (SLAC) in 1975 [4].

Meanwhile the theoretical foundation for modern particle physics was set by the theory of relativity [5] and quantum electrodynamics (QED) [6–8]. A. Salam, S. Weinberg and S.L. Glashow based their work on this theoretical framework and developed the theory of weak nuclear interactions in the 1960s [9–11]. This work suggested the existence of the gauge bosons $W^\pm$ and Z^0, which were later discovered by the UA1 and UA2 experiments in the 80s [12, 13].

But still the masses of the gauge bosons could not be explained by the underlying theory. The solution was given by P. Higgs, R. Brout and F.Englert with the development of the Brout-Englert-Higgs mechanism [14, 15].

Another field of discovery was the theory of quantum chromodynamics (QCD). This development was almost parallel to the development of the Higgs mechanism and was able to explain the strong interaction between quarks and gluons [16, 17].

A combination of all these theories was put together in form of the Standard Model of particle physics (SM). This theory is able to explain three out of four fundamental forces in physics: the electromagnetic, the weak and the stron interaction. But it is still unable to describe the force of gravitation.

Up to today the Standard Model is not disproven by any experiment. Its parameters were precisely measured in multiple experiments. The discovery of the Higgs boson 2012 was the last missing particle of the complete content of the Standard Model. But there are still some challenges the Standard Model faces. One of which is the deviation of the anomalous magnetic moment of the muon. To explain phenomena like this the physics beyond the Standard model have to be assumed.

One extension of this theory is the two-Higgs-Doublet-Model (2HDM), which adds a second Higgs doublet to the theory. As a consequence four additional Higgs bosons occur. One of these is the CP-odd A boson. Because of the rare production and decay processes of these additional bosons, particle colliders with a high luminosity and high center-of-mass energy are required in combination with high resolution detectors. The LHC at CERN is powerful enough to produce a total (Run-2) luminosity of $139\,\mathrm{fb}^{-1}$ at a center-of-mass energy of $13\,\mathrm{TeV}$.

This thesis shows the search of the CP-odd A boson, which was developed by previ-

ous theses of P. Moder, T. Kreße and X. Sonntag [18–20]. It adds a tool to determine QCD background and introduces a multivariate analysis in form of a parameterized neural network (PNN).

To give an overview of the full analysis a theoretical overview is given in Chapter 2. Here the focus lies on the Higgs mechanism and parameter constraints on the A boson. Afterwards the experimental setup at CERN is explained in Chapter 3.

Chapter 4 describes the generation of Monte Carlo samples, as well as the acquisition of data by the ATLAS detector. The actual analysis is presented in Chapter 5. Here the relevant background processes are shown together with the signal process. In Chapter 6 a summary is given on how to apply PNNs on the data, which is to be analyzed. In the end a final conclusion and an outlook for future improvements can be seen in Chapter 7.

Within the whole thesis natural units were used.

2. Theory

To understand the proccesses and the analysis at the ATLAS detector, it is necessary to give a theoretical foundation.

In this chapter it is explained, how the flavour-aligned 2HDM predicts the CP-odd Higgs boson (Sec. 2.2.2). The flavour-aligned 2HDM works as an extension of the Standard Model of particle physics. An explanation of the Standard Model, with a deeper look into the Higgs Sector, is given in the next section.

In particle physics methods of statistics need to be used to analyze the high event-numbers. These methods are explained afterwards.

2.1. The Standard Model of Particle Physics

The Standard Model of particle physics is a quantum field theory based on the gauge symmetry group: $\mathrm{SU(3)}_C \times \mathrm{SU(2)}_L \times \mathrm{U(1)}_Y$, consisting of three sub-groups. The $\mathrm{SU(3)}$ corresponds to the strong interaction [21, 22]. This interaction acts in between colour-charged particles. The electroweak interactions, which are formalized as a unification of the electromagnetic [23–25] and weak interactions [9, 10, 26] are based on the $\mathrm{SU(2)}_L \times \mathrm{U(1)}_Y$.

Particles get split into two main categories: fermions with half-integer spin and bosons with integer spin. Spin-1 bosons act as carriers for the three interactions: photons for the electromagnetic interaction, W- and Z-bosons for the weak interaction and gluons for the strong interaction.

Alltogether there are overall 18 particles predicted by the Standard Model. The fermions consist of six quarks and six leptons. Only the quarks carry a colour charge, while both quarks and leptons carry an electroweak charge. See Fig. 2.1 for the whole particle content [27, 28].

In the following sections only the electroweak sector will be explained in detail [30, 31].

2.1.1. The Electroweak theory

As mentioned before the electroweak interaction is based on the $\mathrm{SU(2)}_L \times \mathrm{U(1)}_Y$ symmetry group with the resulting Lagrangian:

$$\mathcal{L}_{\mathrm{SU(2)}_L \times \mathrm{U(1)}_Y} = \mathcal{L}_{gauge} + \mathcal{L}_{Higgs} + \mathcal{L}_f + \mathcal{L}_{Yuk} \tag{2.1}$$

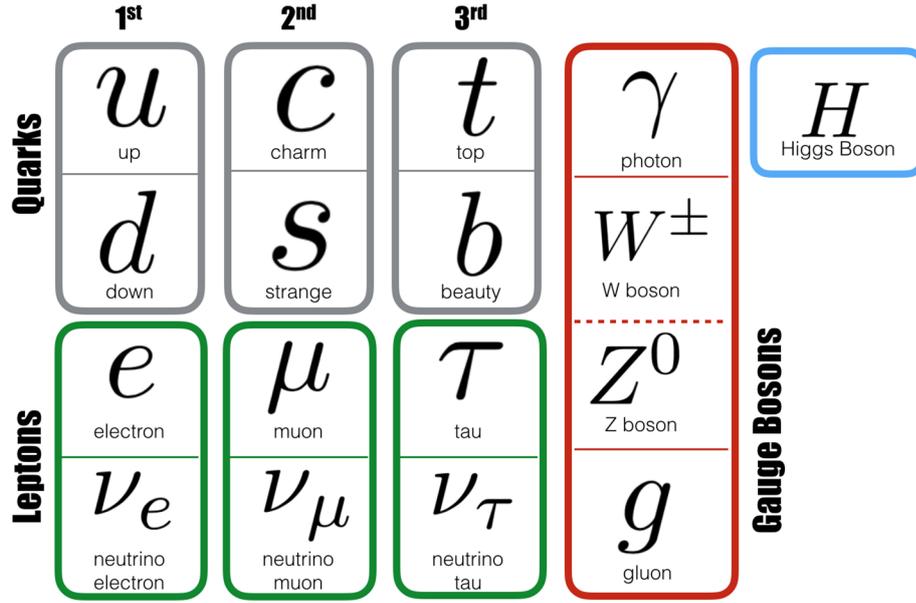Firstly the fermion term $\mathcal{L}_f$ is analysed.

Figure 2.1.: Particle Content of the Standard Model [29]

$$\mathcal{L}_f = \bar{L}i\gamma_\mu D^\mu L + \bar{e}_R i\gamma_\mu D^\mu e_R + \bar{Q}i\gamma_\mu D^\mu Q + \bar{u}_R i\gamma_\mu D^\mu u_R + \bar{d}_R i\gamma_\mu D^\mu d_R \qquad (2.2)$$

with $L = (\nu_e, e)_L^T$ and $Q = (u,d)_L^T$ being the left-handed lepton- and quark doublets with the weak isospin T. ν_e are the different neutrinos, e are the leptons (electrons, muons and taus), u the uptype quarks (up, charm and top) and d the downtype quarks (down, strange and bottom). Within Eq. 2.2 these terms have to be summed over all possible fermion generations.

In the part of the Lagrangian for the right-handed fermions neutrinos do not appear, as they do not exist in the original SM at all.

The weak isospin T is 0 for singlets and $1/2$ for doublets. This defines the third component of the weak isospin T_3 to be $+1/2$ for the first particle of a fermion doublet and $-1/2$ for the second particle of a fermion doublet. Together with the electromagnetic charge Q, T_3 defines the weak hypercharge Y:

$$Q = T_3 + Y \qquad (2.3)$$

The Lagrangian from Eq. 2.2 has to be invariant under $\mathrm{SU(2)}_L \times \mathrm{U(1)}_Y$ gauge transformations:

$$L \rightarrow L' = e^{i\alpha(x)Y_L} \cdot e^{i\sum_a \Theta_a(x)T^a} L \qquad (2.4)$$

$$e_R \rightarrow e'_R = e^{i\alpha(x)Y_R} e \qquad (2.5)$$

with $\alpha(x)$ and $\Theta_a(x)$ being gauge functions, $Y_{L,R}$ the weak hypercharges of left- or right-handed fermions and T^a the generators of $\mathrm{SU}(2)_L$.
These generators are given by

$$T^a = \frac{\sigma^a}{2} \tag{2.6}$$

with σ^a being the Pauli matices:

$$\sigma^1 = \begin{pmatrix} 0 & 1 \\ 1 & 0 \end{pmatrix}, \sigma^2 = \begin{pmatrix} 0 & -i \\ i & 0 \end{pmatrix}, \sigma^3 = \begin{pmatrix} 1 & 0 \\ 0 & -1 \end{pmatrix}. \tag{2.7}$$

To keep the Lagrangian invariant under these transformations the covariant derivatives D^μ are used:

$$D^\mu L = (\partial^\mu + ig_W T^a W_A^\mu + ig_Y Y_L B^\mu)L \tag{2.8}$$

$$D^\mu e_R = (\partial^\mu + ig_Y Y_R B^\mu)e_R \tag{2.9}$$

This introduces the gauge fields W_a^μ and B^μ. These are related to the vector fields $W^{\pm\mu}$, Z^μ and A^μ, which represent the gauge bosons $W^\pm$, Z^0 and γ of the electroweak interaction.

$$W^{\pm\mu} = \frac{1}{\sqrt{2}}(W_1^\mu \mp iW_2^\mu) \tag{2.10}$$

$$\begin{pmatrix} A^\mu \\ Z^\mu \end{pmatrix} = \begin{pmatrix} \cos\Theta_W & \sin\Theta_W \\ -\sin\Theta_W & \cos\Theta_W \end{pmatrix} \begin{pmatrix} B^\mu \\ W_3^\mu \end{pmatrix} \tag{2.11}$$

Within this equation Θ_W is the weak mixing angle, that combines the coupling constants for the weak interaction g_W and g_Y.

$$\cos\Theta_W = \frac{g_W}{\sqrt{g_W^2 + g_Y^2}} \tag{2.12}$$

2.1.2. The Brout-Englert-Higgs Mechanism in the Standard Model

In Sec. 2.1.1 the fermion term and the gauge term have been analysed. But in Eq. 2.1 two additional terms appear. Without these terms all fermions and bosons appear massless. This assumption is easily dismissed by experimental evidence of massive particles, especially the gauge boson masses have been measured at $m_W = 80.4$ GeV and $m_Z = 91.2$ GeV [32].
The introduction of simple mass terms would break the gauge invariance proposed in Eq. 2.4 and Eq. 2.5. To solve the problem of gauge boson masses an additional complex scalar Higgs field isodoublet Φ has to be introduced together with a potential $V(\Phi)$ [14, 15, 31].

$$\Phi = \begin{pmatrix} \Phi_+ \\ \Phi_0 \end{pmatrix} \tag{2.13}$$

Also the Higgs Lagrangian is added.

$$\mathcal{L}_{Higgs} = (D_\mu \Phi)^\dagger (D^\mu \Phi) - V(\Phi^\dagger \Phi) \tag{2.14}$$

with the Higgs potential:

$$V(\Phi) = \mu^2 \Phi^\dagger \Phi + \lambda (\Phi^\dagger \Phi)^2 \tag{2.15}$$

Here the parameter λ is the quartic Higgs self coupling strength and is real and positive, whereas μ^2 is real but can be positve or negative. In the positive case the ground state of the Higgs field is at $\Phi = 0$. This case is not very interesting since no elementary particle would gain would be massive that way. To produce massive gauge bosons the negative case has to be analysed. With $\mu^2 < 0$ the Higgs potential is shaped like a "Mexican hat" as shown in Fig. 2.2. Since there is an infinite number of possible ground states, the SU(2) × SU(1) symmetry is spontaneously broken as soon as one ground state is chosen.
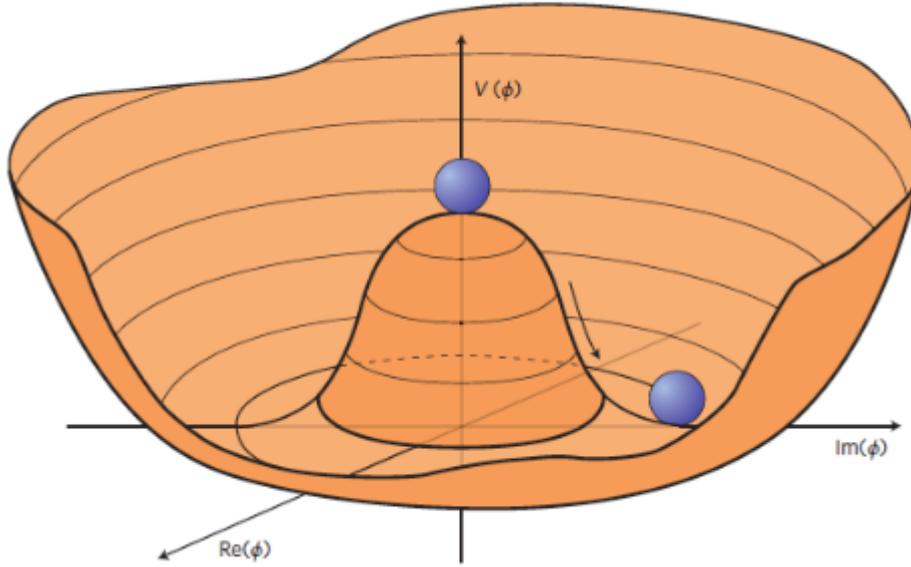

Figure 2.2.: Higgs potential for the case $\mu^2 < 0$. Once a ground state with the lowest energy at the bottom of the potential is chosen, the rotational symmetry is broken. [33]

For further analyses the ground state can be chosen without loss of generality to be

$$\langle 0| \, \Phi \, |0\rangle = \frac{1}{\sqrt{2}} \begin{pmatrix} 0 \\ v \end{pmatrix} \tag{2.16}$$

with the vacuum expectation value (VEV) v, wich relates to the parameters λ and μ^2 from the Higgs potential through $\frac{v^2}{2} = \frac{-\mu^2}{2\lambda}$. The ground state is invariant under $U(1)_Q$ gauge transformations, which represents the gauge group of quantum electrodynamics (QED).

After an expansion of the Higgs field around its VEV with a field $H(x)$ like

$$\langle 0| \, \Phi \, |0\rangle = \frac{1}{\sqrt{2}} \begin{pmatrix} 0 \\ v + H(x) \end{pmatrix} \tag{2.17}$$

the Higgs Lagrangian $\mathcal{L}_{Higgs}$ changes due to the covariant derivative.

$$\begin{aligned}
\mathcal{L}_{Higgs} &= \frac{1}{8}|g_W W_\mu^3 - g_y B_\mu|^2 \, (v + H(x))^2 + \frac{1}{8} g_W^2 |W_\mu^1 - i W_\mu^2|^2 \, (v + H(x))^2 \\
&\quad + \frac{1}{2}|\partial_\mu H(x)|^2 + V(\Phi) \\
&= \frac{v^2}{8}\left(g_W^2 + g_Y^2\right) Z_\mu Z^\mu \left(1 + \frac{H(x)}{v}\right)^2 + \frac{v^2}{4} g_W^2 W_\mu^+ W^{-\mu} \left(1 + \frac{H(x)}{v}\right)^2 + 0 \cdot A_\mu A^\mu \\
&\quad + \frac{1}{2}|\partial_\mu H(x)|^2 + V(\Phi)
\end{aligned} \tag{2.18}$$

This Lagrangian contains bilinear terms, which can be interpreted as mass terms, for all gauge bosons.

$$\begin{aligned}
m_A &= 0 \\
m_W &= \frac{g_W v}{2} \\
m_Z &= \frac{v}{2}\sqrt{g_W^2 + g_Y^2} \\
m_H &= \sqrt{2\lambda} v
\end{aligned} \tag{2.19}$$

By this procedure the gauge boson masses are generated. But there still have to be mass terms for the fermions. This is done by coupling the Higgs field Φ to the fermion fields. This is done by the Yukawa term in the SM Lagrangian.

$$\begin{aligned}
\mathcal{L}_{Yuk} &= \lambda_l \bar{L} \Phi e_R + \lambda_d \bar{Q} \Phi d_R + \lambda_u \bar{Q} \Phi^c u_R + \text{h.c.} \\
&= \lambda_l \frac{v + H}{\sqrt{2}}(\bar{e}_R e_L + \bar{e}_L e_R) + ...
\end{aligned} \tag{2.20}$$

with the coupling constants $\lambda_{l,d,u}$ for the fermions and the charge conjugate of the Higgs field $\Phi^c = i\sigma^2 \Phi^*$. In this part of the Lagrangian only particles with both a left- and a right-handed component couple to the Higgs field. This may hint, that

neutrinos may not gain their masses via the Higgs mechanism.
As a result the fermion masses follow.

$$m_{l,u,d} = \frac{\lambda_{l,u,d}v}{\sqrt{2}} \tag{2.21}$$

2.1.3. Symmetry and symmetry violation in the SM

CP-symmetry is a symmetry under CP transformation, which is a combination of the parity (P) and the charge (C) transformation. The parity operator mirrors the spacial coordinates:

$$P\Psi(x,y,z) = \Psi(-x,-y,-z) \tag{2.22}$$

This means the parity operator has an eigenvalue $\lambda_P = \pm 1$, because after applying it twice, the original state is restored.

$$P^2\Psi(x,y,z) = P\Psi(-x,-y,-z) = \Psi(x,y,z) \tag{2.23}$$

Fermions hold an intrinsic parity of $+1$ while anti-fermions hold a parity of -1. The parity of bosons depend on their state and spin as shown in Tab. 2.1.

state	spin $|\vec{s}|$	parity
scalar	0	+1
pseudoscalar	0	−1
vector	1	−1
pseudovector	1	+1

Table 2.1.: Parity eigenvalues of bosons depending on their state and spin. These values are only correct for a an angular momentum of $\vec{l} = 0$. for a nonzero angular momentum the total angular momentum $\vec{j} = \vec{l} + \vec{s}$ needs to be considered.

In 1957 C.S. Wu investigated the angle of the spin orientation of a cobalt-60 nucleus and an emmited electron, produced by β^--decay. This was the first evidence of parity violation in the SM.
To tackle this problem the charge conjugation operator C is used. this operator flips the charge of a state, resulting in the corresponding anti-state:

$$C|\Psi\rangle = |\bar{\Psi}\rangle \tag{2.24}$$

Because after applying this operator twice the initial state is obtained, the eigenvalues are again $\lambda_C = \pm 1$. But the CP symmetry is still not conserved in the SM. This was refuted by experiments on neutral kaon systems in 1964.
To save symmetry conservation, another transformation is added towards the CP operators. This is time reversal with the operator T. The CPT theorem states that the combination of those three transformations leads to a fundamental exact symmetry. This theorem was not refuted in any experiments.

2.2. Physics beyond the SM

2.2.1. Motivation

The SM is currently the most reliable theory, since it describes most of the phenomena in our universe correctly. But there are still some challenges the original SM can not explain. One of these are the aforementioned non-vanishing neutrino masses. Also only three out of the four fundamental forces are described in the SM. This missing force is gravity, which is not important in particle physics yet, since for it to be relevant the energies used in experiments need to get close to the *Planck scale*. The SM also does not explain the existence of so called dark matter, which mainly interacts with visible matter through the gravitational force.
This thesis focuses on another observation, which does not match SM predictions. Several measurements have shown a deviation of the anomalous magnetic moment of the muon

$$a_\mu = \frac{(g-2)_\mu}{2} \tag{2.25}$$

from Standard Model predictions.
This deviation is shown in Fig. 2.3. The experimental values were obtained by the Brookhaven National Laboratory (BNL) and the Fermi National Accelerator Laboratory (FNAL). The combination of these results deviates drastically from SM predictions [34]:

$$a_\mu^{Exp-SM} = 251(59) \times 10^{-11} \tag{2.26}$$

This corresponds to a significance of 4.2σ.

This hints at new ideas for physics beyond the SM, which get partly explained in the following sections.

2.2.2. The 2HDM

One of the simpler extensions to the SM is adding a second Higgs doublet. This creates the two Higgs doublet model (2HDM). This model could support supersymmetrical theories [35], since a second Higgs doublet is needed for supersymmetry. It could explain the baryon assymetry [36] or it potentially could explain the deviation of the anomalous magnetic moment of the muon.
As proposed additionally to the first Higgs doublet $\Phi_1 = \begin{pmatrix} \Phi_1^+ \\ \Phi_1^0 \end{pmatrix}$ from Sec. 2.1.2, a second one is introduced: $\Phi_2 = \begin{pmatrix} \Phi_2^+ \\ \Phi_2^0 \end{pmatrix}$.
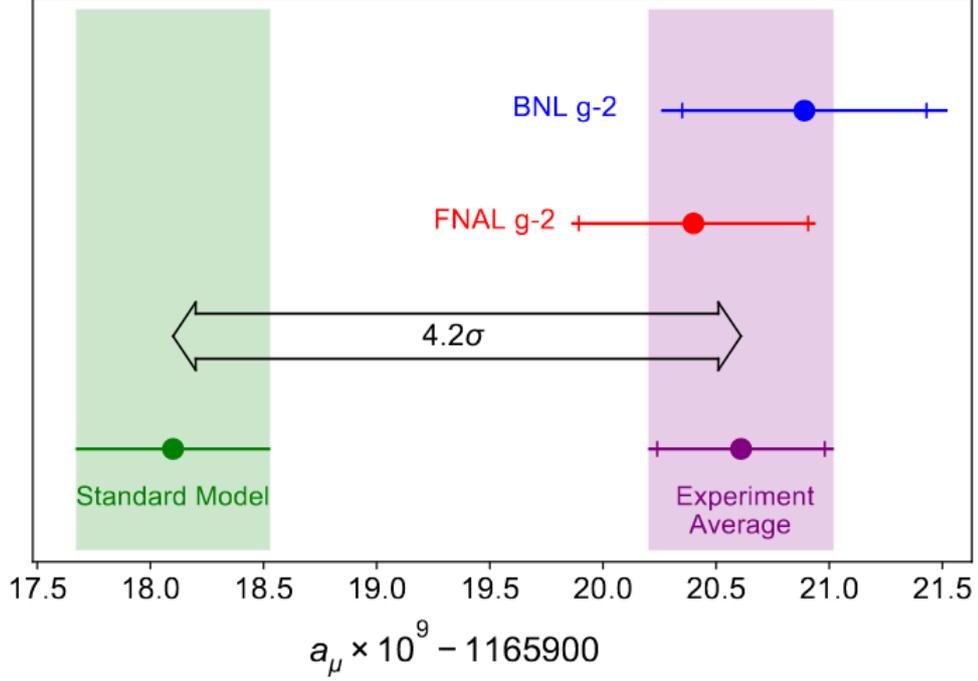
Figure 2.3.: Results of $g-2$ measurements from BNL E821 (blue), FNAL (red) and the combined average of $a_\mu = 116592061(41) \times 10^{-11}$, with a diference of 4.2σ towards the SM prediction [34]

Under CP symmetry conservation a new scalar potential arises:

$$V(\Phi_1, \Phi_2) = m_{11}^2 \Phi_1^\dagger \Phi_1 + m_{22}^2 \Phi_2^\dagger \Phi_2 - (m_{12}^2 \Phi_1^\dagger \Phi_2 + \text{h.c.}) + \frac{\lambda_1}{2}(\Phi_1^\dagger \Phi_1) + \frac{\lambda_2}{2}(\Phi_2^\dagger \Phi_2)$$
$$+ \lambda_3(\Phi_1^\dagger \Phi_1)(\Phi_2^\dagger \Phi_2) + \lambda_4(\Phi_1^\dagger \Phi_2)(\Phi_2^\dagger \Phi_1) + \frac{1}{2}[\lambda_5(\Phi_1^\dagger \Phi_2)^2 + \text{h.c.}]$$
$$+ [\lambda_6(\Phi_1^\dagger \Phi_1) + \lambda_7(\Phi_2^\dagger \Phi_2)]\Phi_1^\dagger \Phi_2 + \text{h.c.}]$$

$$(2.27)$$

m are mass parameters and λ other free parameters. Again choosing one of the minima at $\langle 0| \Phi_{1,2} |0\rangle = \frac{1}{\sqrt{2}}\begin{pmatrix} 0 \\ v_{1,2} \end{pmatrix}$ leads to the VEVs $v_{1,2}$, of the two Higgs doublets with the ration:

$$\tan\beta \equiv \frac{v_2}{v_1} \tag{2.28}$$

After a rotational transformation the doublets are redefined like:

$$H_1 = \cos\beta\Phi_1 + \sin\beta\Phi_2,$$
$$H_2 = -\sin\beta\Phi_1 + \cos\beta\Phi_2 \tag{2.29}$$

This means the second Higgs doublet H_2 obtains a VEV of zero and the first H_1 gets an SM-like VEV of $v = \sqrt{v_1^2 + v_2^2}$ [37].

From the first Higgs doublet the two Higgs bosons h and H are derived. The second one delivers the Higgs bosons A and $H^\pm$. This means there are overall five Higgs bosons, h and H are CP-even and neutral, while A is CP-odd and $H^\pm$ has an electromagnetic charge.

This general 2HDM still has the main problem of tree-level flavor-changing neutral currents (FCNCs). These should vanish under application of the Paschos-Glashow-Weinberg theorem [38], which means that charged right-handed fermions only couple to one of the doublets. To do this, discrete symmetries on the doublets have to be imposed. Four possible types of the 2HDM with vanishing FCNCs arise from the symmetry $Z_2 : \Phi_1 \to -\Phi_1; \Phi_2 \to \Phi_2$. These are depicted in Tab. 2.2.

Φ_1 couples in case of Type I to all fermions, in Type II to down-type quarks and charged leptons, in Type X only to charged leptons and in Type Y only to up-type quarks. For every type Φ_2 couples to the fermions which are not coupling to the first Higgs doublet.

Model	ζ_u	ζ_d	ζ_l
Type I	$\cot\beta$	$\cot\beta$	$\cot\beta$
Type II	$\cot\beta$	$-\tan\beta$	$-\tan\beta$
Type X	$\cot\beta$	$\cot\beta$	$-\tan\beta$
Type Y	$\cot\beta$	$-\tan\beta$	$\cot\beta$

Table 2.2.: Yukawa coupling parameters relative to the SM Yukawa couplings ζ_f for the different types of the 2HDM [39]

2.2.3. The flavour-aligned 2HDM

One way of finding a solution to the problem of FCNCs is the flavour-aligned 2HDM [40]. The FCNCs are generally caused by the two Yukawa matrices resulting from the two Higgs doublets. This flavour-aligned model aligns the two scalar doublets in the flavour space of the Yukawa couplings. This means the SM-like Higgs doublet obtains SM-like couplings, while the other doublet obtains couplings proportional to the SM couplings. The proportionality constants are the coupling parameters ζ_u, ζ_d and ζ_l.

The flavour aligned 2HDM includes the four types shown in Tab. 2.2 as special cases. This means constraints onto the coupling parameters. For example in the Type X model the coupling constants ζ_l and $\zeta_{u,d}$ cannot be large at the same time, since $\zeta_u = -\frac{1}{\zeta_l} = \frac{1}{\tan\beta}$.

The maximal contributions of this model towards the anomalous magnetic moment of the muon have been calculated for the maximal up-type coupling parameter not excluded by parameter constraints [39] and are shown in Fig. 2.4. The yellow band shows the 1σ range of the BNL measurements, while the red, blue and grey regions show the resulting a_μ for different lepton coupling parameters ζ_l. This was done

for different heavy Higgs boson masses, ranging from 150 GeV to 300 GeV, because of its effect on the up-type quark coupling parameter. This resulting contribution is shown as a distribution depending on the mass of the A boson. The sharp rise at low m_A can be explained due to collider limits. After the peak a_μ is suppressed with a factor in the order of $\frac{1}{m_A^2}$.

From these figures one can conclude, that the deviation of the anomalous magnetic moment is best explained by high lepton and up-type coupling parameters ζ_l and ζ_u. This is incompatible with Type II and Type X, because Type II forces a proportionality to $\cot\beta$ and Type X to $\tan\beta$ as mentioned before. Type Y is strongly constrained by data from $b \to s\gamma$ measurements [41]. This constraint is effective for every value of $\tan\beta$, since the product $|\zeta_u\zeta_d| = \cot\beta\tan\beta = 1$ can not be small. In Type I this product could be small, but this would also mean a small lepton coupling parameter ζ_l. So every type of this model fails at explaining the deviation of the anomalous magnetic moment of the muon. To fix this issue, independent couplings need to be introduced to the flavour-aligned 2HDM, which is implemented in the general flavour-aligned 2HDM.

2.2.4. Parameter constraints and resulting production and decay of the CP-odd Higgs boson

The flavour-aligned 2HDM is only an extension to the SM and therefore the newly introduced particle content from it is strongly limited by previous measurements agreeing with the SM. A detailed look on parameter constraints can be found in [39].

Most upper limits derive from processes with the same initial and final state as observed SM processes, as the contributions from newly added particles should not be large to agree with measurements within their uncertainty bands. One example is the decay of the SM-like Higgs boson into two CP-odd A bosons $h \to AA$. This branching ratio must be small, since SM-like Higgs boson decays have been studied to a large extend [42].

At first upper limits on the lepton coupling parameter ζ_l or to be more precise its absolute value $|\zeta_l|$ is calculated. These limits are shown in Fig. 2.5. These limits derive from constraints from the leptonic decay of the Z boson and the decay $\tau \to \mu\nu_\tau\bar{\nu}_\mu$, since loop contributions from the additional heavy Higgs bosons have to be suppressed. Also $|\zeta_l|$ is constrained by collider limits. Especially for A boson masses $m_A < 20$ GeV the process $ee \to \tau\tau(A) \to \tau\tau(\tau\tau)$, shown in Fig. 2.6, dominates the upper limit. The measurement of this process was done by the DELPHI collaboration [43] at the Large Electron-Positron Collider (LEP). All these constraints lead to the limits depicted in Fig. 2.5.

The next parameter to obtain upper limits for, is the up-type coupling parameter. These constraints arise from B-physics and LHC data. The main B-physics constraints come from the processes $b \to s\gamma$ and $B_s \to \mu^+\mu^-$. Feynman diagrams of these processes can be found in Fig. 2.7. The upper limits produced by these con-
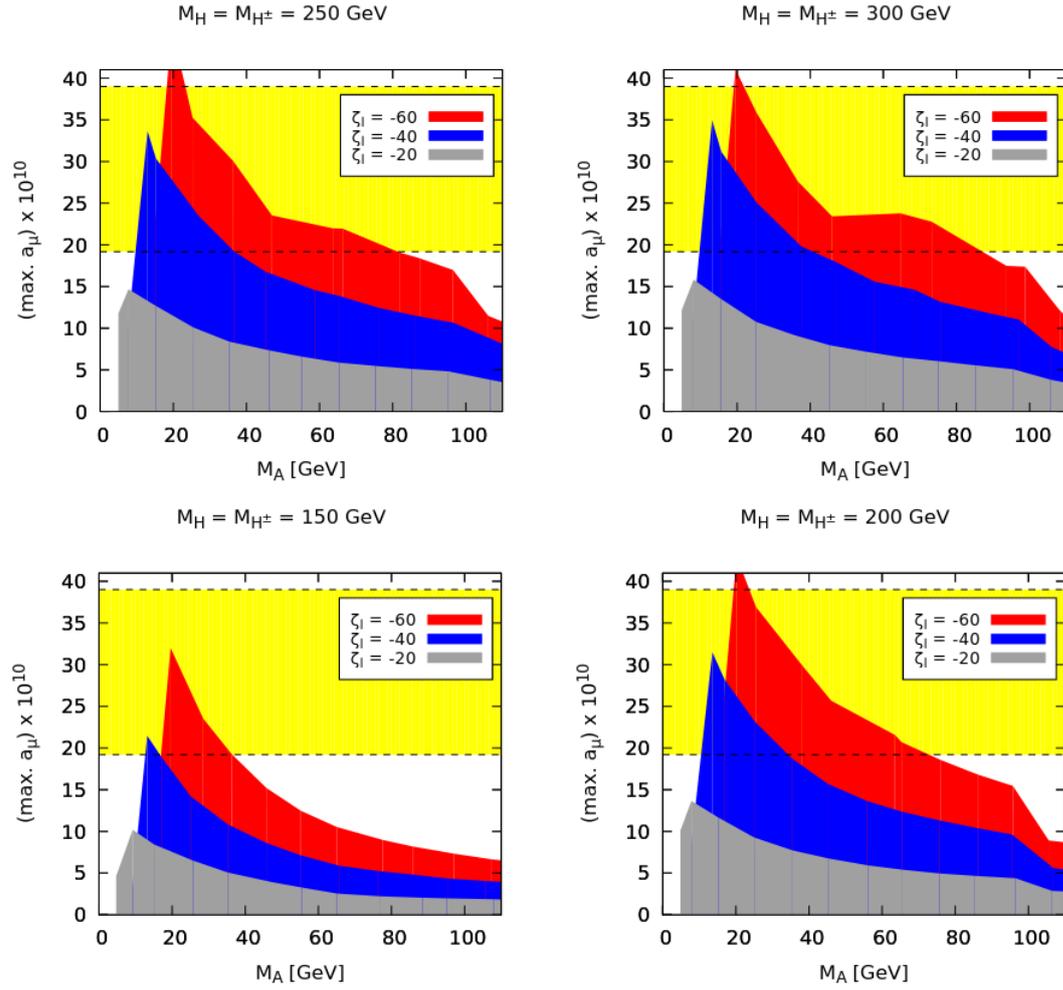
Figure 2.4.: Contribution of the flavor aligned 2HDM to a_μ for four different heavy Higgs masses (m_H and $m_{H^\pm}$) in between 150 and 300 GeV. Also three different lepton coupling strengths are shown over the mass of the A boson m_A. The yellow band shows the measurements of the anomalous magnetic moment of the muon with a deviation of 1σ. These plots do not contain measurements from FNAL [39].

straints are shown in Fig. 2.8. The green region shows the 2σ region of an allowed set of ζ_u-ζ_d plane. This leads to an upper limit of $|\zeta_u| < 0.5$.

For $m_a > m_Z$ the process $pp \to A \to \tau\tau$ dominates the constraints on the up-type coupling parameter, leading to a limit of $|\zeta_u| < 0.2$. The process $pp \to H \to \tau\tau$ sets limits for low A boson masses. The observation of these processes were done by the CMS detector [44]. The maximum allowed ζ_u arising from these decays are shown
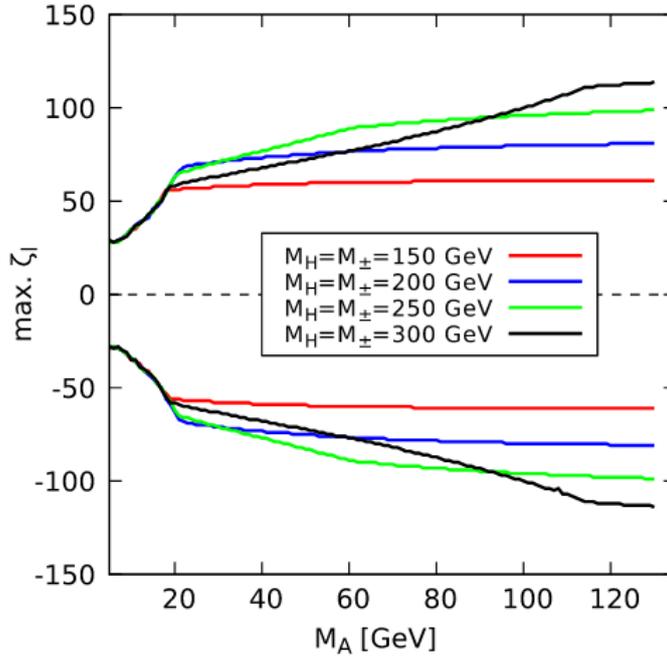
Figure 2.5.: Upper limits on $|\zeta_l|$ as a function of the A boson mass for different heavy Higgs boson masses [39].
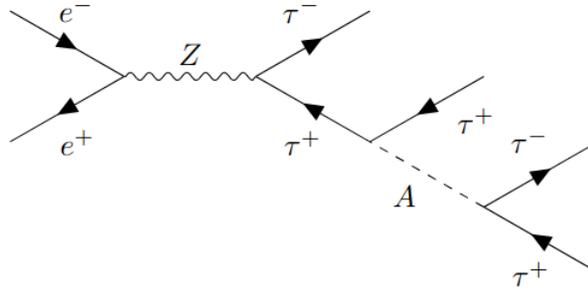

Figure 2.6.: Feynmann diagram of the process $ee \to \tau\tau(A) \to \tau\tau(\tau\tau)$ [18].

in Fig. 2.9. These peak at $m_A < \frac{m_H}{2}$ and around m_Z, which can be explained by the decay $H \to AA$.

With all these constraints, the main production and decay channels are relatively clearly defined. As a result of the high up-type and low down-type coupling parameter the A boson is produced almost exclusively via gluon fusion and a top-quark loop. Because of the large lepton coupling parameter and the mass dependency of the coupling, the A boson decays predominantly into a pair of τ-leptons. See
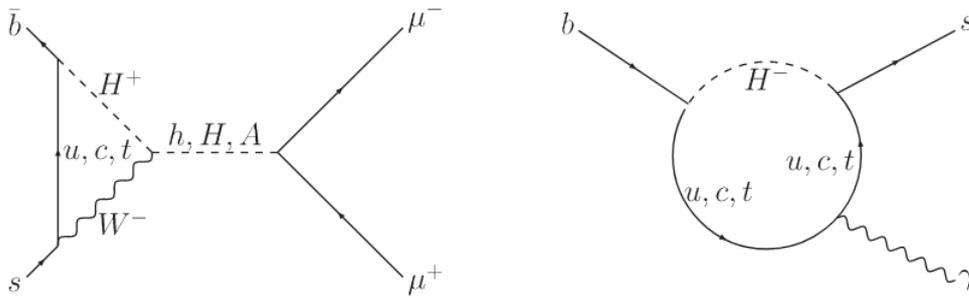
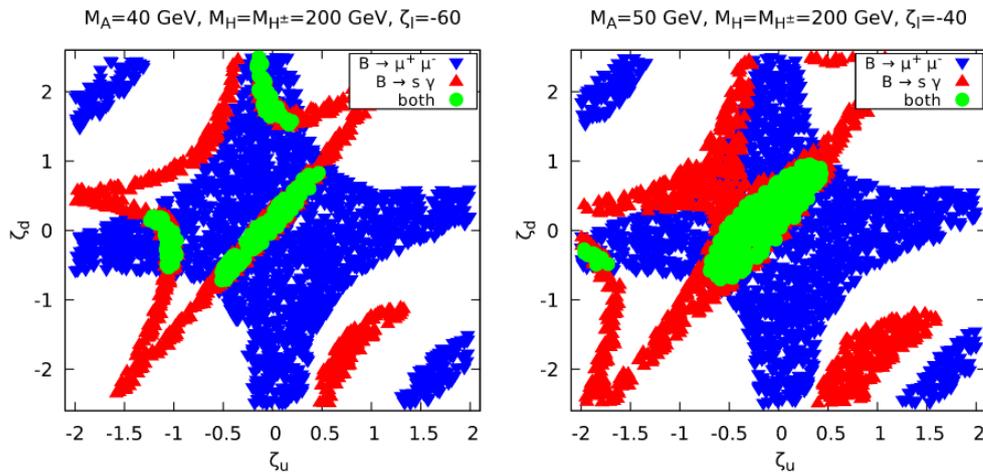Figure 2.7.: Feynman diagrams of the processes $B_s \to \mu^+\mu^-$ (left) and $b \to s\gamma$ (right) [39].

Figure 2.8.: Allowed ζ_u and ζ_d ranges with constraints from $B_s \to \mu^+\mu^-$ (blue), $b \to s\gamma$ and their combination (green). The values for m_A and ζ_l are fixed in these plots. $m_A = 40$ GeV and $\zeta_l = -60$ (left) or $m_A = 50$ GeV and $\zeta_l = -40$ (right), while the heavy Higgs masses are fixed in both plots at $m_H = m_{H^\pm} = 200$ GeV [39].

Fig. 2.10 for the Feynman diagram of the production and decay of the A boson.
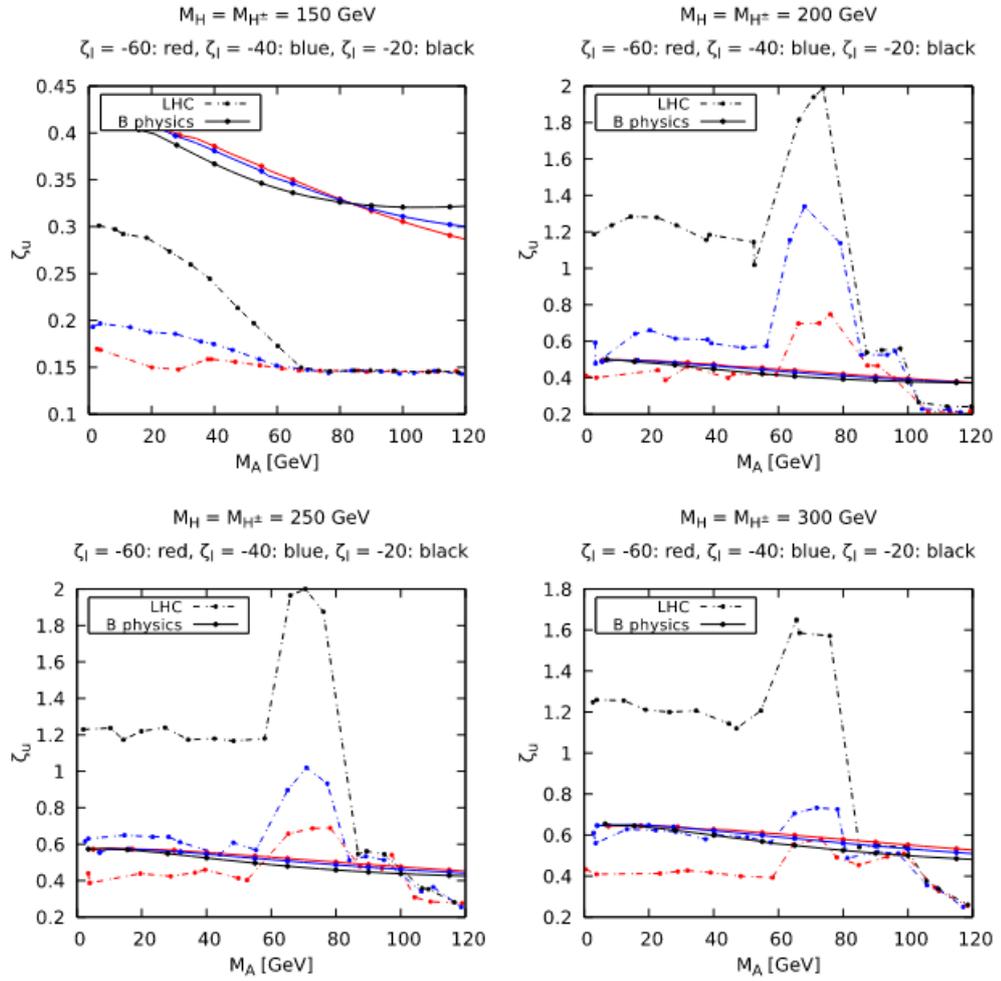
Figure 2.9.: Upper limits on the up-type coupling parameter ζ_u as a function of the A boson mass m_A with fixed values for $m_H = m_{H^\pm}$ and ζ_l. The solid line comes from B-physics and the dashed line from LHC data. [39].
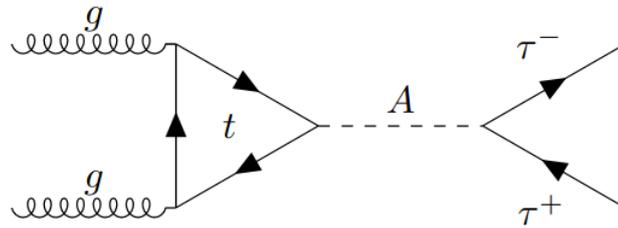

Figure 2.10.: Feynman diagram of the production and decay of the A boson [18].

2.3. Statistical analysis

Since all processes in particle physics are of probabilistic nature and the analysis of which needs a large amount of data, statistical methods need to be applied. This section explains the formalism of searching for new particles and of setting upper limits, which was also used to obtain the parameter limits from Sec. 2.2.4. This method is explicitly explained in [45].

The main method for searching a new particle is the test of hypotheses. Here two hypotheses are defined. One is the null hypothesis H_0, containing all known background processes from the SM. H_0 is then testet against the so called signal hypothesis H_1. This contains both background and signal processes. The signal is obtained from the light CP-odd Higgs boson predicted by the general flavour-aligned 2HDM as shown in Sec. 2.2.4.

To obtain upper limits on the production cross-section the roles of these hypotheses are swapped. Here the p-value is calculated. The p-value is a quantity describing the agreement between the two hypotheses. If the p-value drops below a certain threshhold, hypotheses will be discarded. In the particle physics community this threshold is set to $p = 5.7 \times 10^{-7}$.

2.3.1. Theory of limit setting

To obtain upper limits, a profile likelihood ratio test is used. Therefore all events are accumulated in a histogram with N bins. The histogram is called $n = (n_1, ..., n_N)$, with n_i being the number of events in bin i. With expected signal events in bin i s_i and expected background events b_i in bin i the overall number of events can be written as:

$$E[n_i] = \mu s_i + b_i \tag{2.30}$$

Here μ is the signal strength parameter, which usually lies in between 0 and 1. 0 is the background-only hypothesis and 1 the nominal signal hypothesis. When assuming a Poisson distribution, the product of all bins leads to the likelihood function.

$$L(\mu) = \prod_{j=1}^{N} \frac{(\mu s_j + b_j)^{n_j}}{n_j!} e^{-(\mu s_j + b_j)} \tag{2.31}$$

To take systematic uncertainties into account, a set of k nuisance parameters $\theta = (\theta_1, ..., \theta_k)$ is introduced. With a control distribution $m = (m_1, ..., m_M)$ another expected event number per bin can be calculated:

$$E[m_i] = u_i(\theta) \tag{2.32}$$

u_i are calculated bin entries depending on θ. With the probability density function $f_{u_i}(m_i, \theta)$ (PDF) of $u_i(\theta)$ the likelihood function gets expanded:

$$L(\mu, \theta) = L(\mu) f_{u_i}(m_i, \theta) \tag{2.33}$$

μ is then tested by the profile likelihood ratio:

$$\lambda(\mu) = \frac{L(\mu, \hat{\hat{\theta}})}{L(\hat{\mu}), \hat{\theta}} \tag{2.34}$$

Here $\hat{\mu}$ and $\hat{\theta}$ are the maximum-likelihood estimators (MLEs) and $\hat{\hat{\theta}}$ is the nuisance parameter, where the likelihood function is maximal for each μ.

Since negative values of $\hat{\mu}$ would imply a negative signal strength, the profile likelihood ratio has to be modified:

$$\tilde{\lambda} = \begin{cases} \frac{L(\mu, \hat{\hat{\theta}})}{L(\hat{\mu}, \hat{\theta})} & , \hat{\mu} \geq 0, \\ \frac{L(\mu, \hat{\hat{\theta}}}{L(0, \hat{\theta})} & , \hat{\mu} < 0 \end{cases} \tag{2.35}$$

This is used afterwards to obtain a test statistic:

$$\tilde{t}_\mu = -2 \ln \tilde{\lambda}(\mu) \tag{2.36}$$

With this the p-value can be calculated:

$$p_\mu = \int_{\tilde{t}_{\mu,obs}}^{\infty} f(\tilde{t}_\mu) d\tilde{t}_\mu \tag{2.37}$$

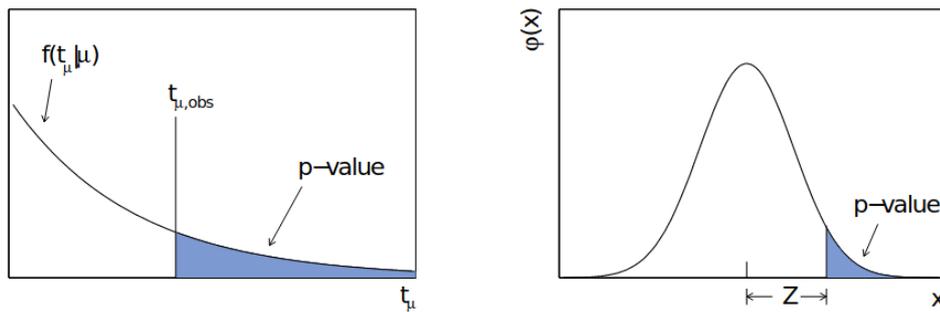Fig. 2.11 shows an illustration of how the p-value works on a test statistic and how it is related to the significance Z.

Figure 2.11.: Illustration of the p-value with regards to the observed test statistic $t_{\mu,obs}$ (left) and its relation to the significance Z of a standard normal distribution (right) [45].

In practice the PDFs are usually unknown. In particle physics these are mostly obtained by pseudo-experiments like the Monte Carlo method. This method generates random data from a given probability function. Since this method uses a lot of computing time, a different approach may be desired. To achieve this, Wilks' theorem [46] is applied in combination with the Wald approximation [47]. This changes Eq. 2.36 for a Gaussian distributed $\hat{\mu}$ and its standard deviation σ:

$$\tilde{\lambda} = \begin{cases} \frac{(\mu-\hat{\mu})^2}{\sigma^2} & ,\hat{\mu} \geq 0, \\ \frac{\mu^2}{\sigma^2} - \frac{2\mu\hat{\mu}}{\sigma^2} & ,\hat{\mu} < 0 \end{cases} \tag{2.38}$$

This leads to a PDF with the mean value μ' of $\hat{\mu}$:

$$f(\tilde{t}_{\mu'}) = \frac{1}{2} \frac{1}{\sqrt{2\pi}} \frac{1}{\sqrt{\tilde{t}_\mu}} \exp\left[-\frac{1}{2}\left(\sqrt{\tilde{t}_\mu} + \frac{\mu-\mu'}{\sigma}\right)^2\right]$$
$$+ \begin{cases} \frac{1}{2} \frac{1}{\sqrt{2\pi}} \frac{1}{\sqrt{\tilde{t}_\mu}} \exp\left[-\frac{1}{2}\left(\sqrt{\tilde{t}_\mu} + \frac{\mu-\mu'}{\sigma}\right)^2\right] & ,\tilde{t}_\mu \leq \frac{\mu^2}{\sigma^2}, \\ \frac{1}{\sqrt{2\pi}\left(\frac{2\mu}{\sigma}\right)} \exp\left[-\frac{1}{2} \frac{\left(\sqrt{\tilde{t}_\mu} - \frac{\mu-\mu'}{\sigma}\right)^2}{\left(\frac{2\mu}{\sigma}\right)^2}\right] & ,\tilde{t}_\mu > \frac{\mu^2}{\sigma^2} \end{cases} \tag{2.39}$$

This method requires less computing time to obtain the PDFs with σ and μ' provided by measurements [45].

While only one parameter has been considered so far, models like the 2HDM depend on a set of parameters. This requires the approach of setting upper limits on these parameters. Above these limits the parameters are excluded with a given confidence level. This method is done similarly to obtaining the p-value with a modified test statistic $\tilde{t}_\mu$ from Eq. 2.36 that vanishes for $\hat{\mu} > \mu$:

$$\tilde{q}_\mu = \begin{cases} -2\ln\frac{L(\mu,\hat{\hat{\theta}})}{L(0,\hat{\hat{\theta}}(0))} & ,\hat{\mu} < 0, \\ -2\ln\frac{L(\mu,\hat{\hat{\theta}})}{L(\hat{\mu},\hat{\theta})} & ,\hat{\mu} \geq 0, \\ 0 & ,\hat{\mu} > \mu \end{cases} \tag{2.40}$$

Setting $\tilde{q}_\mu$ to zero for $\hat{\mu} < \mu$ makes the predictions in this intervall more compatible with μ than the obtained data. This makes sure this intervall is not included in the rejected parameter region. The p-value is again defined by using Wilks' theorem and the Wald approximation like in Eq. 2.38.

$$\tilde{q}_\mu = \begin{cases} \frac{\mu^2}{\sigma^2} - \frac{2\mu\hat{\mu}}{\sigma^2} & ,0 < \hat{\mu}, \\ \frac{(\mu-\hat{\mu})^2}{\sigma^2} & ,0 \leq \hat{\mu} \leq \mu, \\ 0 & ,\hat{\mu} > \mu \end{cases} \tag{2.41}$$

This leads to the PDF:

$$f(\tilde{q}_\mu|\mu') = \Phi\left(\frac{\mu'-\mu}{\sigma}\right)\delta(\tilde{q}_\mu)$$

$$+ \begin{cases} \frac{1}{2}\frac{1}{\sqrt{2\pi}}\frac{1}{\sqrt{\tilde{q}_\mu}}\exp\left[-\frac{1}{2}\left(\sqrt{\hat{t}_\mu}+\frac{\mu-\mu'}{\sigma}\right)^2\right] & , 0 < \tilde{q}_\mu \le \frac{\mu^2}{\sigma^2}, \\ \frac{1}{\sqrt{2\pi}\left(\frac{2\mu}{\sigma}\right)}\exp\left[-\frac{1}{2}\frac{\left(\sqrt{\hat{t}_\mu}-\frac{\mu-\mu'}{\sigma}\right)^2}{\left(\frac{2\mu}{\sigma}\right)^2}\right] & , \tilde{q}_\mu > \frac{\mu^2}{\sigma^2} \end{cases} \quad (2.42)$$

with Φ as the cumulative function of the Gaussian distributions. Again the standard deviation σ and the mean value $\hat{\mu}$ are obtained from data. The calculated p-value from Eq. 2.37 describes the the probability of obtaining the observed or (in regard to the signal) more extreme data assuming the null hypothesis holds. To produce the confidence level (CL), which excludes values defeating the threshold, a threshold parameter α has to be set. This refutes a hypothesis for $p_\mu < \alpha$. This parameter is usually set to be $\alpha = 0.05$ corresponding to a 2σ deviation. The CL is then defined as:

$$\mathrm{CL}_{s+b} = 1 - \alpha \quad (2.43)$$

The subscript $s + b$ means, the limit for the signal-and-background hypothesis is viewed. For small signal expectations and large background uncertainties this limit can be too strong. The normalized CL_s is introduced in order to reduce this effect. This is an approximation of the signal-only hypothesis [48]:

$$\mathrm{CL}_s = \frac{\mathrm{CL}_{s+b}}{\mathrm{CL}_b}, \quad (2.44)$$

which leads to a transformed p-value:

$$p'_\mu = \frac{p_\mu}{1 - p_b} \quad (2.45)$$

with

$$p_b = 1 - \int_{\tilde{q}_\mu,obs}^{\infty} f(\tilde{q}_\mu|0,\hat{\hat{\theta}}(0,obs))d\hat{q}_\mu. \quad (2.46)$$

2.3.2. Expected limits

The before mentioned calculations use measured data to calculate the limits. But until the analysis is in a ready-to-use state, the measured data is usually blinded to prevent a biased analysis.
This means expected upper limits are calculated until the unblinding, using an artificial dataset, called Asimov data set [49]. This data pseudo data is defined in

a way that the true parameter values are obtained, if the likelihood is maximized. This is done, if the Asimov data $n_{i,A}$ and $m_{i,A}$ are set to the expected values

$$n_{i,A} = E[n_i] = \mu' s_i + b_i, \quad m_{i,A} = E[m_i] = u_i(\theta). \tag{2.47}$$

The method of the last section is then applied and the Asimov likelihood L_A and its profile likelihood ratio $\tilde{\lambda}_A(\mu)$ can be calculated, using the the Asimov standard deviation of $\hat{\mu}$:

$$\sigma_A = \frac{\mu - \mu'}{\sqrt{\tilde{q}_{\mu,A}}}. \tag{2.48}$$

with $\tilde{q}_{\mu,A} = -2\ln\tilde{\lambda}_A(\mu)$ corresponding to the median of the probability density $f(\tilde{q}_\mu|0)$. The calculated limits from the obtained CL_s shows the lowest possible upper limit, if the data would follow the the predicted background hypothesis. The error bands $\pm N\sigma$ are obtained by varying $\hat{\mu}$ by $N\sigma_A$ around the mean value μ'. Since lower expected parameter limits indicate a higher sensitivity towards signal detection, this is a tool for comparing different analyses.

3. The LHC and the ATLAS experiment

While this thesis focuses on the analyses of experimental data, the data have to be acquired. Particle colliders provide this kind of data. The LHC [50] is the largest particle collider in the world. At this collider this search for the CP-odd Higgs boson is performed.

This chapter gives an overview of the experimental setup used for data acquisition. The LHC produces and accelerates hadronic particle beams, which collide at several points at the LHC. At one of these point the ATLAS detector is located.

3.1. LHC

The LHC is located at the European Organization for Nuclear Research (CERN) accelerator complex. It consists of a ring of superconducting magnets measuring 27 km in diameter. The proton-proton center-of-mass energy is currently set to be at $\sqrt{s} = 13$ TeV. These energies are achieved by many accelerator before the before mentioned accelerator ring. This complex injects the hadron beams into the LHC via two transfer tunnels.

The mean number of generated events is given by:

$$N_{event} = L\sigma_{event} \tag{3.1}$$

with σ_{event} as the cross-section of the studied process and the luminosity under assumption of a Gaussian beam distribution:

$$L = \frac{N_b^2 n_b f_{rev} \gamma_r}{4\pi \epsilon_n \beta*} F \tag{3.2}$$

where N_b is the number of particles per bunch, n_b the number of bunches, f_{rev} the revolution frequency, γ_r the relativistic gamma factor, ϵ_n the normalized tranverse beam emittance, $\beta*$ the beta function at the point of the collision and F the geometric luminosity reduction factor, which is caused by the crossing angle at the collision point [50].

Fig. 3.1 shows the CERN accelerator complex. It shows the two high-luminosity experiments, ATLAS [52] and CMS [53] aswell as two low-luminosity experiments LHCb [54] for B-physics experiments and TOTEM [55] for small angle proton detection from elastic scattering. Also the ALICE experiment [56], which operates with ion beams, is located at CERN.

To reach such high luminosities, large beam intensities are required, which is achieved
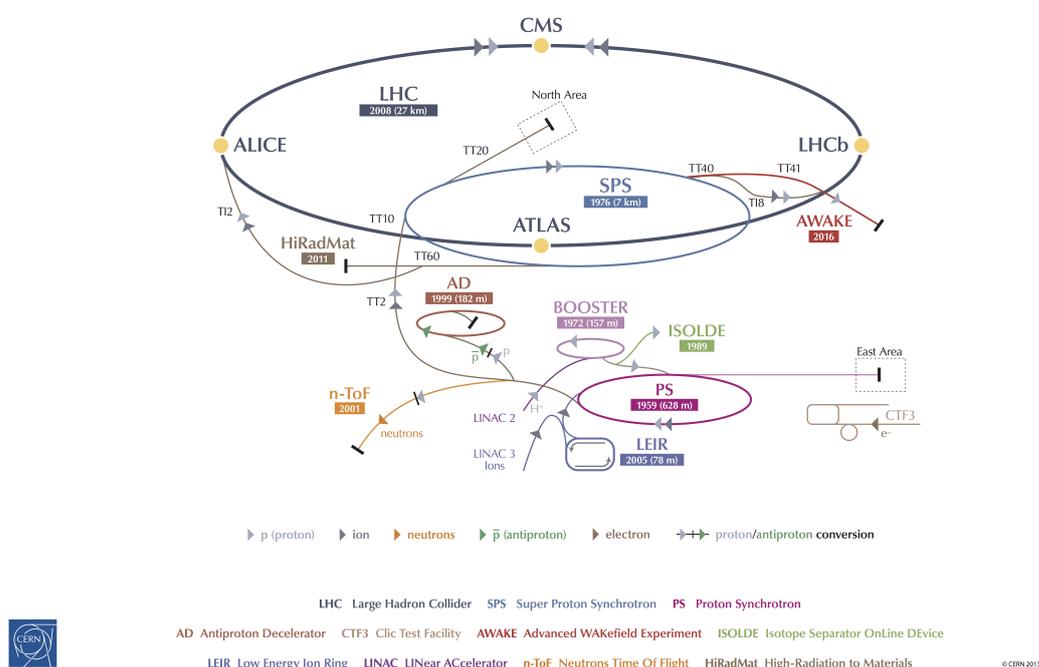
Figure 3.1.: The CERN accelerator complex [51]

by a proton-proton collider with two seperate accelerator rings in opposite magnetic fields. Because of space issues, since the LEP tunnel is also located at CERN, the magnets are helium-cooled twin bore magnets consisting of two beam channels in the same mechanical structure. The peak dipole field of 8.33 T allows a proton energy of up to 7TeV. This corresponds to a center-of-mass energy of 14TeV. With the help of this accelerator a new Higgs boson was discovered 2012 by both, ATLAS and CMS [44, 57].

In between 2013 to 2015 the LHC was shut down, as several improvements were made. As a result Run-2 delivered a luminosity of 139 fb^{-1}.

3.2. The ATLAS detector

The ATLAS detector is built in a cylindrical shape around one of the collision points. Its length is 44m and the diameter is 25m. The detector consists of different layers and detection systems as shown in Fig. 3.2. These layers and systems are explained in this section.
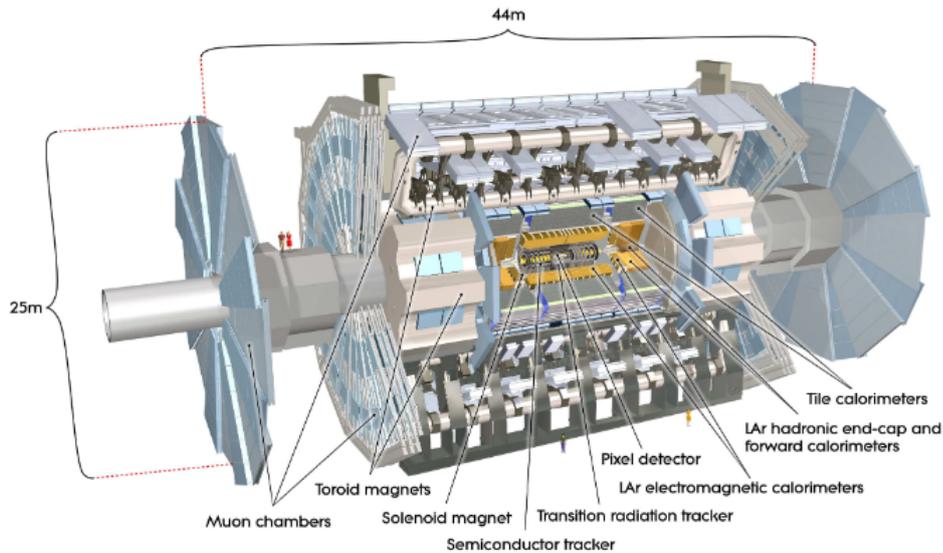
Figure 3.2.: View of the different layers of the ATLAS detector [58]

3.2.1. The ATLAS coordinate system

Within the ATLAS experiment a right-handed Cartesian coordinate system with its origin at the point of proton-proton collisions is defined. The x-axis points towards the center of the accelerator ring, the y-axis points upwards and the z-axis points along the beam-line [58].

The transverse plane perpendicular towards the beam is defined by the polar coordinates r and ϕ. The azimuthal angle ϕ is the angle towards the x-axis. The second angle towards the z-axis is the polar angle θ, which is normally expressed though the pseudorapidity:

$$\eta = -\ln\tan\frac{\theta}{2}. \tag{3.3}$$

As a consequence the pseudorapidity ranges from 0 (perpendicular to the beam-line) to $\pm\infty$ (parallel to the beam-line).

Particularly for this analyses the angular distance in the $\eta - \phi$ space is defined:

$$\Delta R = \sqrt{(\Delta\eta)^2 + (\Delta\phi)^2}. \tag{3.4}$$

Since the momenta of the colliding partons are not known exactly, momentum conservation can only be used in the transverse plane. As a result all transverse momenta $p_T = \sqrt{p_x^2 + p_y^2}$ sum up to zero. This leads to the missing transverse momentum E_t^{miss}, which is caused by particles not detected such as neutrinos:

$$E_t^{miss} = |-\sum \vec{p_T}|. \tag{3.5}$$
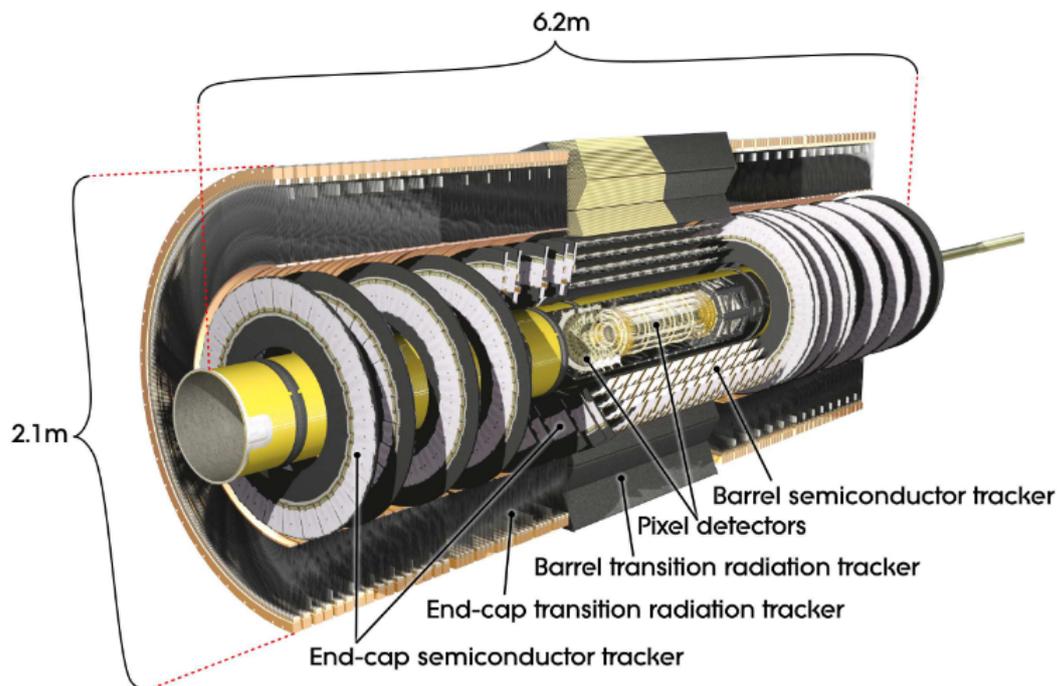
3.2.2. The inner Detector

Figure 3.3.: Cut-away view of the inner detector [58]

The cylindrically shaped inner detector has a diameter of 2.1 m with three sub-detectors: the pixel detector, Semiconductor Tracker (SCTs) and Transition Radiation Trackers (TRTs). A cut-away view of the inner detector is shown in Fig. 3.3. The inner detector is highly sensitive on momentum, charge and trajectories of charged particles above a certain p_T-threshold (0.5 GeV), since it is located right next to the collision point. For this purpose a magnetic field of 2 T is applied on the whole inner detector. This field is proveided by a superconducting solenoid [59].
The trajectory of charged particles is therefore bent by the Lorentz force. From the resulting bending radius the p_T of the particle can be calculated.
Precision tracking detectors cover the area of $|\eta| < 2.5$. These are built either concentrically around the beam axis (barrel region) or discoidally perpendicular to the beam axis (end cap region) [58].

Pixel Detector

As the pixel detector is located closest to the interaction point, it has the highest granularity. It possesses 1744 identical pixel sensors with 47 232 pixels each. Those are arranged in three layers, resulting in about 80 million readout channels. The pixels consist of doped silicon semiconductor detectors with a size of 50×400 m^2 in

the $(R - \phi) \times z$-space. Charged particles create electron-hole pairs in the semiconductor detectors. With this an accuracy of 10 m in the transverse plane and 115 m along the beam axis is reached.

Within the shutdown phase a fourth barrel layer was added to the detector, in order to improve the perfomance. This Insertable B-Layer (IBL) was inserted to decrease the distance between the detector and the collision point, which increases the impact parameter reconstruction and tracking precision [60, 61].

Semiconductor Tracker

The adjacent Semiconductor Tracker (SCT) is again using doped silicon as active material. With four double layers of silicon micro-strips in the barrel region and nine disk layers for each of the tow end-caps it consists of 6.3 million readout channels. The strip pitch of 80 m means an accuracy worse than the pixel detector of 17 m in the $(R - \phi)$ plane and 580 m in the z space for the end-cap region. Again an area $\eta < 2.5$ is covered [58].

Transition Radiation Tracker

The TRT is the most outer part of the inner detector, delivering a continuous tracking system. 300,000 drift tubes with a diameter of 4 mm are build in this part of the detector. These are filled with an active gas mixture.

To measure transition radiaton of relativistic charged particles traversing between media of different dielectric constants, the straws are embedded in polypropylene foils and fibers with different refraction indices. As a particle propagates through the TRT, the particle and the transition radiation ionize the active gas mixture. The signal is then produced with the help of an electric field, produced by a negatively charged straw tube wall, consisting of gold-plated tungsten wire. This part of the detector possesses and accuracy of 130 m per straw. The transition radiation depends on the Lorentz factor γ. Since electrons are relatively light, the resulting signal is stronger than those of hadrons of the same momentum [58, 62, 63].

3.2.3. The calorimeter system

To determine the energy of particles, calorimeters are used. The particles deposit energy in the active detector material, which can then be read out.

Electromagnetic calorimeters are able to measure the energy of particles interacting via the electromagnetic force, like electrons or photons. Hadronic calorimeters measure the energy of particles interacting via the strong force like hadrons. The cut-away view of the calorimeter systems is shown in Fig. 3.4.

Liquid Argon Electromagnetic Calorimeter

The electromagnetic calorimeter uses liquid argon as active material and thus it is called liquid argon (LAr) detector. This part of the detector is again divided into a
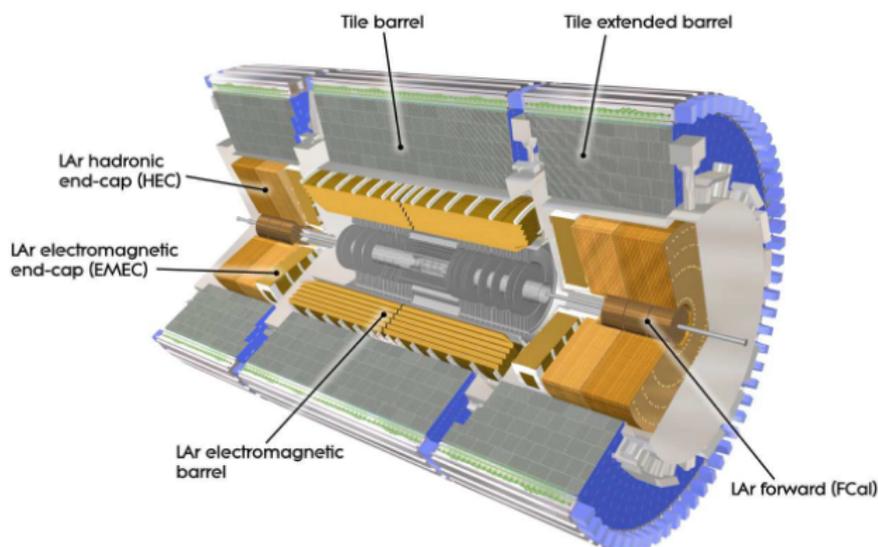
Figure 3.4.: Cut-away view of the calorimeter system [58]

barrel and two end-cap parts. The parrel region covers an area of $|\eta| < 1.475$ and the end-cap parts cover the area for $1.375 < |\eta| < 3.2$. It covers the full ϕ-region without cracks, due to its accordion-like shape.

Copper readout electrodes are located between absorber plates, made of lead. Electrons with great momentum traverse through the lead and emit radiation (bremsstrahlung). The emitted photons create electron-positron pairs, which will again emit radiation. As this process creates EM showers, the energy of the electrons will decrease, until it is low enough to ionize the liquid argon. Again an electromagnetic field is applied to copper electrodes. This makes the ionisation electrons drift towards the electrodes and the total energy can be calculated with the sum of the energy of all electrons and positrons of the shower [64, 65].

Hadronic calorimeters

The hadronic calorimeters follow a similar principle as the EM calorimeter. Here hadronic showers are created by collision of the hadrons with the nuclei of the absorber material. The signal is again created by ionization in the active material. Since not all hadrons are electrically charged, not every particle of the shower ionizes the active material and therefore leaves a signal. This limits its precision.

This part of the calorimeter consists of sub-detectors. Outside the EM calorimeter barrel the tile calorimeter is located. The absorber material is steel and the active material are scintillating tiles. This covers an area of $|\eta| < 1.7$ [66].

The second hadronic calorimeter is the LAr hadronic calorimeter. It consists of an end-cap part, with a range of $1.5 < |\eta| < 3.2$ and a forward part, with a range of

$3.1 < |\eta| < 4.9$. The active medium LAr fills $8.5\,\mathrm{mm}$ gaps between its copper plates [64].
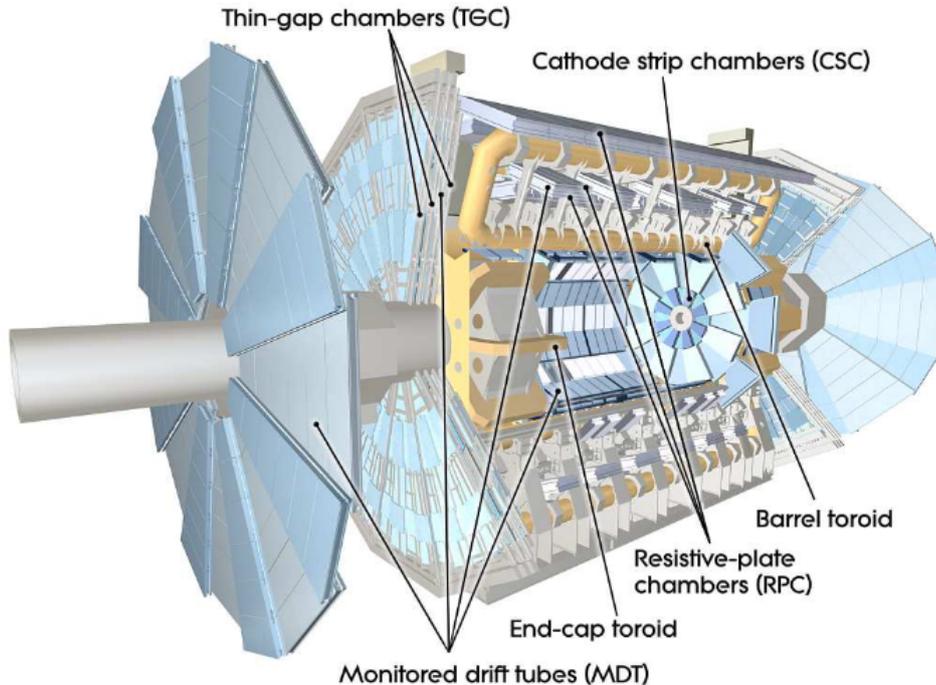
3.2.4. The muon spectrometer

Figure 3.5.: Cut-away view of the muon system [58]

As muons are around 200 times heavier than electrons, they do not deposit all of their energy in the electromagnetic calorimeter. This is why muons pass most of the detector layers undetected. To measure their tracks, the muon spectrometer was installed. In Fig. 3.5.

The different trigger and tracking chambers of the muon spectrometer are embedded in a magnetic field, caused by three air-core superconducting toroid magnets. Again the muon trajectories are bent by the Lorentz force. For $|\eta| < 1.4$ large barrel toroid magnets deflect the muons. For $1.6 < |\eta| < 2.7$ two small end-cap magnets do the same. In the region inbetween a combination of both deflect the muons. Four different types of chambers measure the properties of the muon tracks (Monitored Drift Tube Chambers (MDTs), Cathode Strip Chambers (CSCs) Resistive Plate Chambers (RPCs) and Thin Gap Chambers (TGCs)). The trajectory coordinates and the momentum of the muons are measured in MDTs and CSCs. The CSCs cover an area of $2.0 < |\eta| < 2.7$.

The RPC in the barrel region and the TGC in the end-cap region contribute to the

muon trigger system for $|\eta| < 2.4$ [67].

3.2.5. The ATLAS Trigger and Data Acquisition system

A huge amount of data, obtained from the ATLAS detector, has to be processed, due to collisions every 25ns. To decide wether the data is useable the Trigger and Data Acquisition system (TDAQ) is installed. It is impossible to record and save every event, since the data size of one event is around $1.3\,\mathrm{MB}$. This means the processing would require a bandwidth of $50\,\mathrm{TB/s}$. The trigger system consists of two levels. The hardware-based Level-1 trigger (L1) searches for high transverse momentum, high missing transverse and total transverse energy particles. This level consists of three different systems. The L1 calorimeter system (L1Calo) processes information from both calorimeters. The L1 muon trigger system (L1Muon) uses information from the RPCs and TGCs. The last systems are the L1 topological trigger modules (L1Topo) have been added for Run-2 in order to examine topological structures. This information is then forwarded towards the central trigger processor (CTP). In the end the event rate is reduced to $100\,\mathrm{kHz}$.

The second level is the High Level Trigger (HLT). This trigger is software based and therefore can use more information previously processed by the detector. This reduces the data rate to about $1\,\mathrm{kHz}$. The resulting events are then written out to the storage system. The whole TDAQ system is shown in Fig. 3.6.
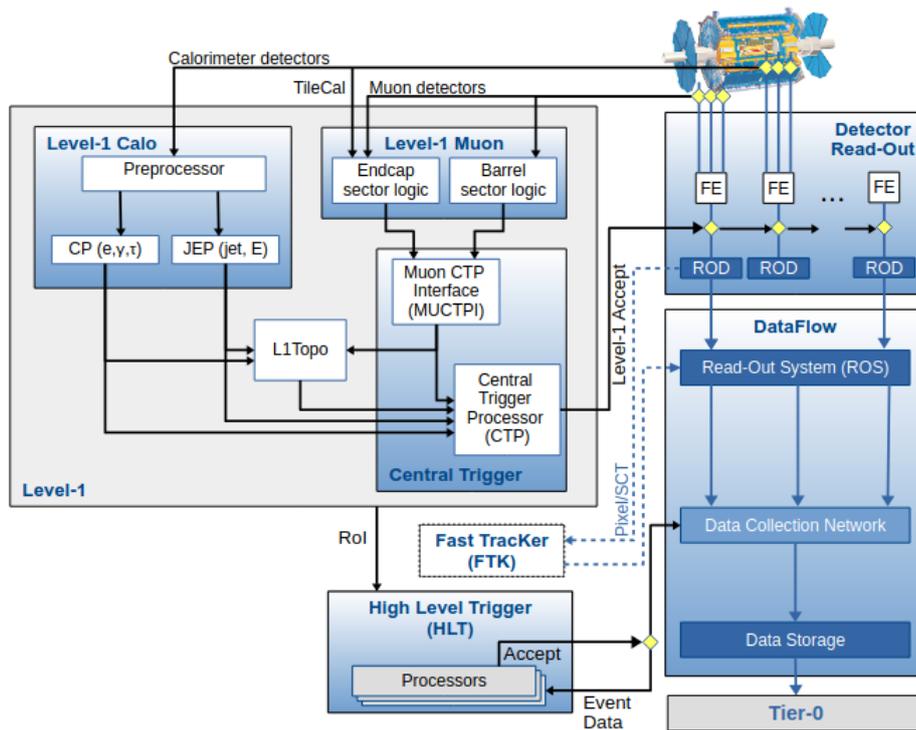
Figure 3.6.: Overview of the Run-2 trigger system [**Collaboration_2020**]

4. Data samples and generation of Monte Carlo samples

The data used in this thesis was acquired during the LHC Run-2 from 2015 to 2018. Fig. 4.1 shows the cumultive luminosity over that time period. Data with approved quality is depicted as blue area. This means an integrated luminosite of $139\,\mathrm{fb}^{-1}$ is reached at a center-of-mass energy of $13\,\mathrm{TeV}$.
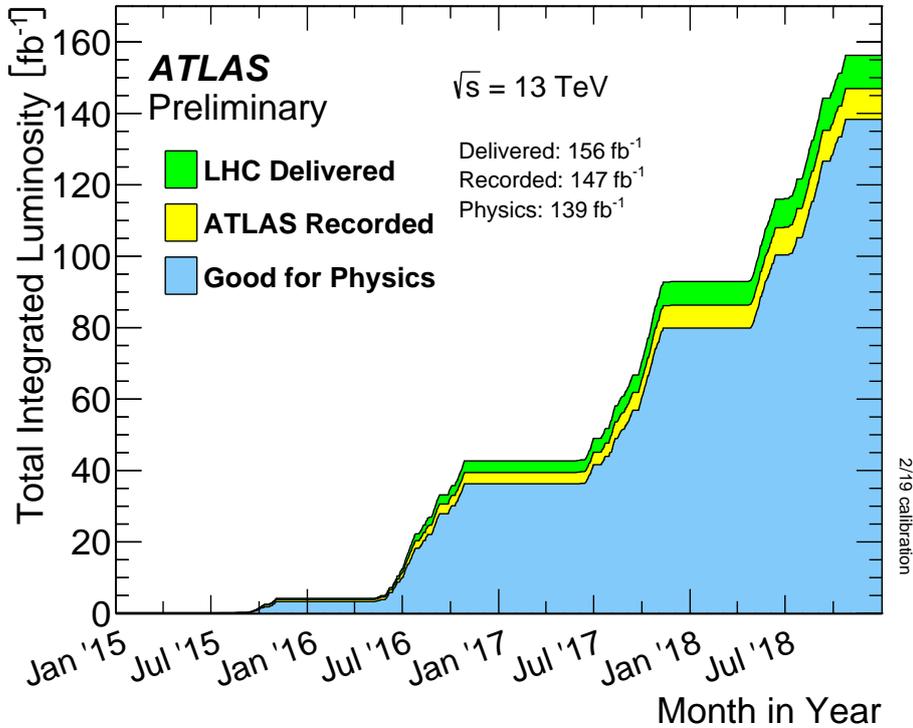

Figure 4.1.: Cumulative luminosity delivered by the LHC (green), recorded by the ATLAS detector (yellow) and good quality data (blue) for stable *pp* collisions at $13\,\mathrm{TeV}$ center-of-mass energy (Run-2) [68].

To generate accurate prediction of event topologies, distributions and scattering cross-sections, Monte Carlo generators are used. As each particle involved in the process has approximately ten degrees of freedom like mass, momentum and lifetime, thousands of kinematic options are possible. To achieve this (pseudo)random

numbers are used to reproduce the quantum machanical likelihoods [69]. This section analizes the differen subprocess of the event generation.
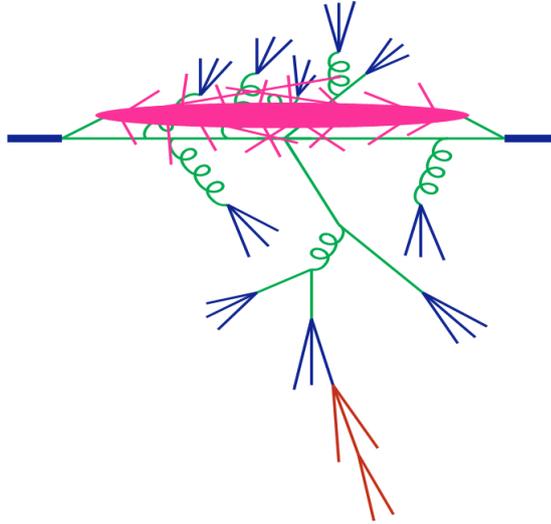

Figure 4.2.: Diagram depicting the structure of a *pp* collision with different colours indicating the different stages of the event generation [70].

Fig. 4.2 illustrates a *pp* collision with the different stages of the Monte Carlo event generation dipicted with different coulours.

The hard scattering is the interaction of the partons insidde the protons. These are simulated by PDFs describing the distribution of partons after the collision via perturbation theory.

Parton showers are illustrated in green. This event generator phase describes the processes the incoming and outgoing partons go through. Because of the colour charges gluons are radiated creating the parton showers.

The confinement of partons is described by hadronization models resulting in hadrons, wich can be measured by the detector. This stage of the event generation is coloured blue.

The underlying event and the pile-up is illustrated in pink. Underlying events are summaries of secondary reactions of the proton remnants. Because of the limited detector readout speed and the high collision rate, additional processes are detected as pile-up. This can be in-time pile-up or out-of-time pile-up. The in-time pile-up occurs, when multiple *pp* collisions happen in the same bunch-crossing. Out-of-time pile-up happens, when other bunch-crossings happen temporally close to the actual collision and are detected, because of the detector readout time. Thus pile-up profiles have to be simulated. These are different for each data-taking period, because the LHC operating conditions are improved constantly. To take the pile-up into account pile-up reweighting is applied on the Monte Carlo samples [71].

The simulation of decaying unstable particles is coloured red [70].

This analysis uses `POWHEG-BOX` [72], `PYTHIA` [73] and `SHERPA` [74] as Monte Carlo generators. Tab. 4.1 lists the Monte Carlo generators used to generate the matrix element (ME) and the PS with for the different processes. A complete list of Monte Carlo samples is given in A.

Process	ME generator	PS generator
$A \to \tau\tau$	`PYTHIA v8.2`	
$H_{125} \to \tau\tau$	`POWHEG-BOX v2`	`PYTHIA v8.2`
$H_{125} \to WW$	`POWHEG-BOX v2`	`PYTHIA v8.2`
diboson (semi-leptonic)	`SHERPA v2.2.1`	
diboson (fully-leptonic)	`SHERPA v2.2.2`	
$Z \to ll$	`SHERPA v2.2.1`	
$W \to l\nu$	`SHERPA v2.2.1`	
$t\bar{t}$	`POWHEG-BOX v2`	`PYTHIA v8.2`
$singletop$	`POWHEG-BOX v2`	`PYTHIA v8.2`

Table 4.1.: List of Monte Carlo generators used for the simulation of the underlying processes of this analysis [75].

Additionally a pre-built derivation has to be uses to skim the obtained data, because the amount of unskimmed data would be too large. This analysis uses the `HIGG3D1` derivation, which only allows two leptons in the final state. This derivation introduces cuts on the lepton p_T and on η^e. If the subleading lepton is a muon, the cut is set to $p_{T,\mu}^{subleadlep} > 2\,\text{GeV}$. If it is an electron, it is set to $p_{T,e}^{\text{subleadlep}} > 4\,\text{GeV}$. The threshold for leading leptons is $p_T^{\text{leadlep}} > 17\,\text{GeV}$. The cut on the electron pseudorapidity is set to $|\eta^e| < 2.6$.

5. Analysis

This chapter presents the actual data analys. This thesis focuses heavily onto a data driven method to estimate background from QCD processes. The event selection and former improvement of signal-to-background ratios, were developed in previous studies [18–20]. The information on particle properties is taken from the Particle Data Group [32].

5.1. Signal process

The flavour-aligned 2HDM, explained in Sec. 2.2.2, introduces four additional Higgs bosons. This analysis searches for the decay of the CP-odd Higgs boson A, which could explain the anomalous magnetic moment of the muon. Fig. 2.4 shows that this explanation is most compatible for low A boson masses m_A. Because of this mass dependence the signal hypothesis in this analysis is set to be $20\text{GeV} < m_A < 90\text{GeV}$. Due to the parameter constraints from Sec. 2.2.4 the main production channel of the A boson is via gluon fusion and a top quark loop. The produced A boson decays almost exclusively into two τ-leptons, because of the high lepton coupling parameter ζ_l. These can decay either leptonically or hadronically. The different decay channels and their branching ratios (BR) are shown in Tab. 5.1.

Because of the low-mass hypthesis, low trigger thresholds are required. Since such low tau triggers do not exist within ATLAS, only leptonic decays are analysed. The sum of all BRs of the leptonic decay possibilities is 35.21%. Additionally, only one muon and one electron are allowed in the final state, since it suppresses the background contribution from $Z \to ee$ and $Z \to \mu\mu$ heavily. This leads to a final BR of 6.2%. In Fig. 5.1 the Feynman diagram of these processes are shown.

Decay mdoe	BR
$h^- n^0 \nu_\tau$ (1-prong with neutrals)	37.01%
$e^- \bar{\nu}_e \nu_\tau$	17.82%
$\mu^- \bar{\nu}_e \nu_\tau$	17.39%
$h^- h^- h^+ \nu_\tau$ (3-prong)	14.55%
$h^- \nu_\tau$ (1-prong with neutrals)	11.51%
others	1.72%

Table 5.1.: BRs of the decay channels of the τ-lepton. The sum of the BRs of the leptonic decay channels is 35.21%.
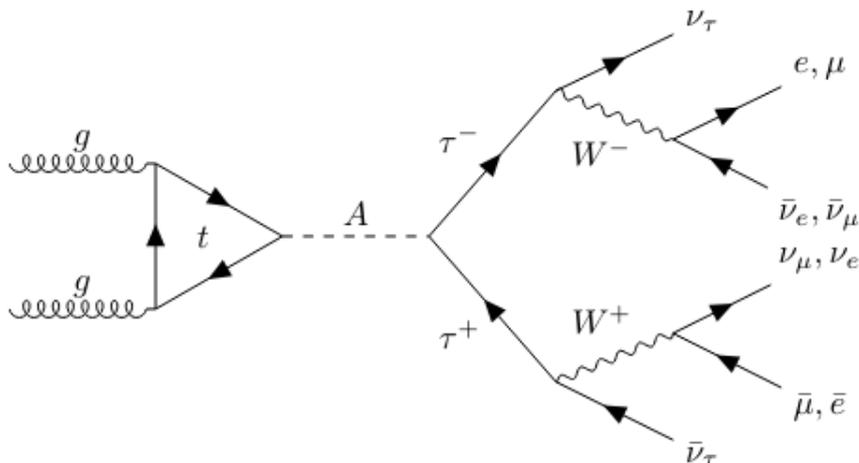
Figure 5.1.: Analyzed production and decay of the *A* boson [18]

5.2. Background processes

The exact contribution of background processes have to be estimated accurately to obtain a precise limit calculation. These contributions are mainly produced by Monte Carlo (MC) simulations.
The following sections describe the main background processes and how similar to the signal process they are.

5.2.1. $Z \to ll$

The *Z* boson decay is the most influential background process, because the *Z* boson is also electrically neutral like the *A* boson. Additionally, its mass ($m_z = 91.2$ GeV) is close to the underlying mass hypotheses. The decay $Z \to \tau\tau$ has the same final state as the signal process, which makes it nearly indistinguishable from the final state of the signal process.

$Z \to \mu\mu, Z \to ee$

This decay is shown in the Feynman diagram in Fig. 5.2. As there are no neutrinos in the final state of this decay, the missing transverse energy of this decay would be lower than in the signal process. Because this is heavily influenced by the kinematics of every particular decay, a stronger criterion is needed. This is achieved by allowing only one electron and muon in the final state, which supresses the same-flavour *Z* decay. This background reduction comes with a signal loss arising from the halved BR. Due to lepton or jet misidentification this background is still remaining, but largely supresses.
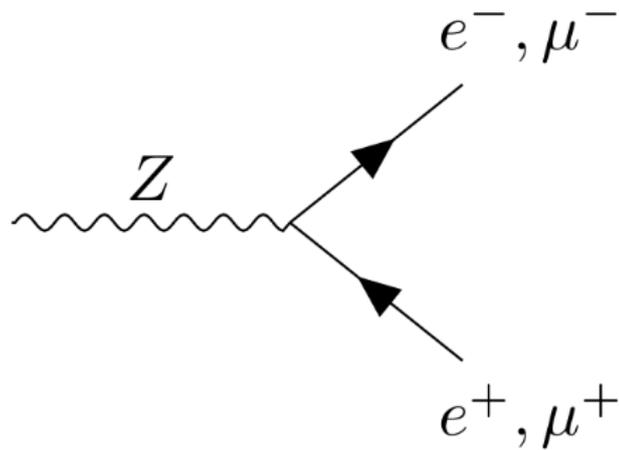
Figure 5.2.: Feynman diagram of the $Z \rightarrow ee$ and $Z \rightarrow \mu\mu$ decays [18]

$Z \rightarrow \tau\tau$

The Z decay into two τ-leptons is different from the other leptonic Z decays, because it has the exact same particles in its final state as the signal process. Thats why this is the main background of the analaysis. A feynman diagram of this process is shown in Fig. 5.3
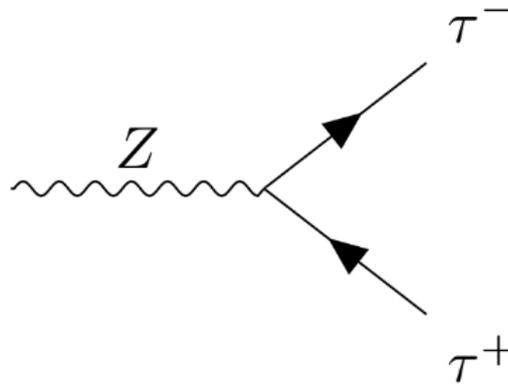

Figure 5.3.: Feynman diagram of the $Z \rightarrow \tau\tau$ decay [18]

There are only small differences between this background and the signal. The A boson is a spin 0 particle with a negative CP eigenvalue and the Z boson has spin 1 and does not have a parity eigenvalue [76]. For a scalar (CP even) Higgs boson, the flight direction of the decay products are preferably anti-parallel, while a pseudoscale (CP odd) Higgs boson produces decay product, which have preferably

a parallel direction of flight (see Fig. 5.5). This preference is enhanced, because the total spin of the ditau system originating from the A boson is zero and because it needs to obtain a CP eigenvalue of -1. As a result the spin alignment of the τ-leptons originating from the decay of a CP-odd Higgs boson has to be antiparallel. τ-leptons originating from a CP-even Higgs boson have a parallel spin alignment. Fig. 5.4 shows the different angles between the decay planes of the two τ leptons originating from a CP-odd Higgs, CP-even Higgs and a Z boson. The distributions are obtained by truth MC particle information. This will lead to a difference in the angular difference ΔR of the τ decay products.
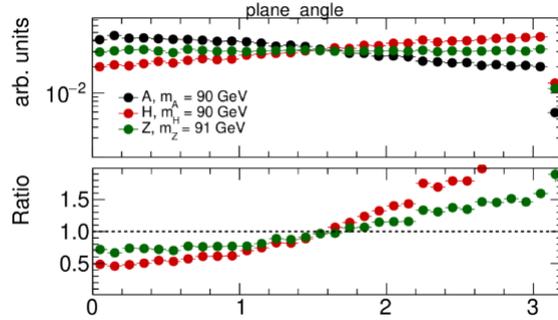

Figure 5.4.: Angle Φ between the τ-lepton decay planes resulting from an A boson (black), CP-even Higgs boson H (red) and a Z boson (green). [18]
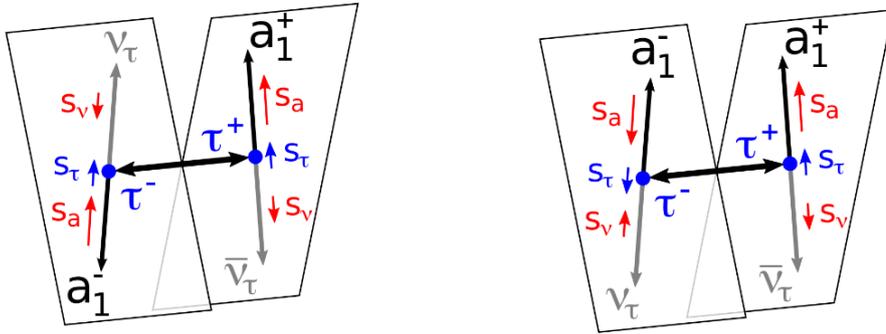

Figure 5.5.: Angle betwee the τ-lepton decay planes for a scalar (left) and pseudoscalar (right) Higgs boson [77]

5.2.2. Top quark processes

Background resulting from processes involving a top quark can either originate from a single top quark (t) or top-antitop pairs ($t\bar{t}$). With a probability of 95.7% a top quark decays into a bottom quark and a W boson [32].
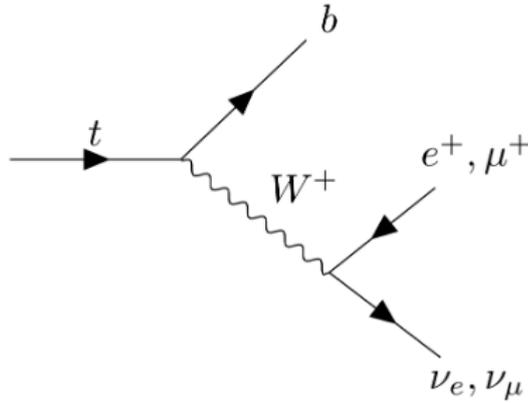
Figure 5.6.: Feynman diagram of the leptonic decay of a single top quark [18]

This W boson can decay leptonically (as shown in Fig. 5.6) or hadronically. This means, the $t\bar{t}$ final state can have the same signature as the signal process. Differences come from the number of involved neutrinos and the contribution of b-quarks in the t decay.

To reduce this background, b-tagging was introduced to the analysis. This mechanism detects events that contains b-jets, which can then be disregarded. This algorithm is not perfect, which means this background stays relevant. Background from single top decays can be detected, even though only one lepton is in the final state. The second lepton can come from a jet falsely identified as a lepton.

Furthermore leptons from the signal process can be falsely identified as b-jets or other b-jets might contribute. This effect is negligibly small, hence does not need further studies.

5.2.3. SM Higgs processes

The SM Higgs boson can leave a similar signature in the detector as the signal process, since it can also decay into two τ-leptons or into two W bosons, which can also decay into two leptons. This makes a full supression of these decays impossible. Because of the low signal mass hypotheses and the higher SM Higgs boson mass of 125 GeV, a suppression of this background can be achieved by differentiation via mass variables.

Also the cross-section of the Higgs boson is much lower than for the signal process regarding the assumed coupling strengths. This makes the contribution of the SM Higgs decays relatively small.

5.2.4. $W \to l\nu_l$

W bosons can decay into one lepton accompanied by the corresponding neutrino as shown in Fig. 5.7. This decay does not match the signal signature, since only one

lepton is produced. But again a lepton can be wrongly detected due to misidenti-
fication of an accompanied jet or pile-up collisions. These contributions should be
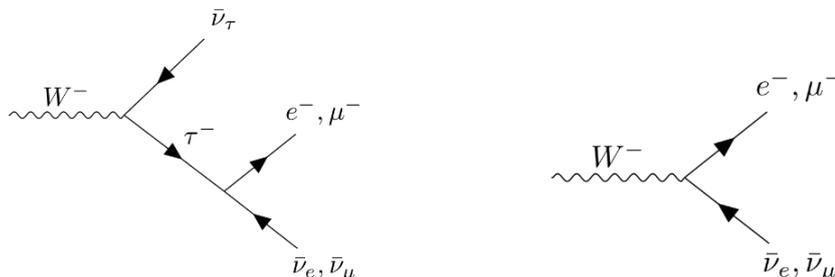small because of the high rejection power of the lepton identification and isolation.

Figure 5.7.: Feynman diagrams of the W decays $W \to \tau \nu_\tau$ (left) and $W \to e\nu_e / W \to \mu\nu_\mu$ [18]

5.2.5. Diboson processes

Diboson processes inlcude all processes that contain the decay of two weak vector
bosons W and Z. These cover a wide range of final states. Some of them leave a
similar detector signature, like two W bosons decaying into two leprons and their
corresponding neutrinos. Other decays can also leave similar detector signatures,
again due to misidentification.

5.2.6. QCD processes

As a result of the proton-proton collisions many QCD processes are involved. These
processes lead to cone-shaped structures called jets, due to hadronization. These
jets can be misidentified as leptons. Again identification and isolation algorithms
are able to supress this kind of misidentification. But especially for low p_T a lot of
these events occur. These events can still be misidentified. Because MC simulation of
these kind of events can not produce a statistically reliable background a data-driven
technique is required to estimate this background. The method used is described in
Sec. 5.4.

5.3. Event selection

5.3.1. Particle identification and reconstruction

The identification of particles and their reconstruction is necessary for every anal-
ysis. This section explains the experimental foundation of the identification and
reconstruction of electrons muons and b-jets.

Electrons

Electrons are an integral part of the analysis, since they appear in the final state of the signal. To reconstuct electrons, the trajectory within the detector layes with three characteristic components are used. These three components are the localized clusters of deposited energy within the EM calorimeter, charged particle tracks in the inner detector and the geometrical matching of those in the $\eta \times \phi$ space. The deposited energy clusters are determined by portionizing the $\eta \times \phi$ space of the EM cuboid into a cuboid grid of fixed size. The cluster candidates are recognized by localizing energy depositions above 30 GeV with a sliding window algorithm [78]. These act as seeds for EM cluster candidates.

The tracks in the inner detector come from hits in the tracking layers of the inner detector. Hits in a three-dimensional measurement represent a space point. The obtained patterns are then fitted by different methods to models of energy loss of charged particles propagating through matter. The information from the EM seeds is then matched to the particle tracks. These tracks are extrapolated to their entry points in the calorimeter.

The identification of electrons uses a likelihood technique [79]. It provides three working points: *loose*, *medium* and *tight*.

Muons

To reconstruct muons, information from the individual reconstructions in the inner detector and the muon spectrometer is taken and combined. The reconstruction in the inner detector happens similarly to the electron reconstruction. In the muon spectrometer hit patterns from different layers that are not rejected by selection criteria are combined. Then fit algorithms are used on these patterns. In the end the reconstruction information from the inner detector and the muon spectrometer are combined and processed by different algorithms.

The muon identification working points *loose*, *medium*, *tight* and $high-p_\text{T}$ are used in combination with different analysis requirements [80].

Jets and b-tagging

Jet identification is necessary, due to the b-tagging for reducing top background processes.

For this thesis two reconstruction algorithms are in use. The anti-k_t algorithm uses the output of the second algorithm, the particle flow algorithm, as input. This algorithm takes the information from the inner detector and the calorimeters as input, using cell-based subtraction for overlap removal between tracks and topo-clusters.

The anti-k_t algorithm then calculates the weighted distance between deposits in the calorimeter d_{ij} and the beam axis B.

$$d_{ij} = \min k_{T,i}^{2p}, k_{T,j}^{2p} \frac{\Delta_{ij}^2}{R^2}$$
$$d_{iB} = k_{T,i}^{2p} \tag{5.1}$$
$$\text{with} \Delta_{ij}^2 = (y_i - y_j)(\Phi_i - \Phi_j).$$

In this equation $k_{T,i}^{2p}$ is the transverse momentum, y_i the rapidity and Φ_i the azimuthal angle of the ith record. $R = 0.4$ and $p = -1$ are set for this analysis. Each iteration merges the two closest entries, which form a cluster. This iteration stops when $d_{i,B}$ reaches the shortest distance and the cluster is classified as a jet. These jets are called AntiKt4EMPFlow jets. [81, 82]

The b-tagging determines whether jets originate from hadrons containing a botton quark. Because of their relatively long lifetime, these jets leave a specific detector signature with two distinct vertices. The used b-tagger is called DL1r [83], which is based on a deep learning neural netwwork algorithm. The input variables of this algorithm are the displaced vertices reconstructed in the inner detector, impact paramters of the tracks and discriminating variables constructed by a recurrent neural network. The recurrent neural network analyses the correlations (spatial and kinematic) between tracks originating from the same b-hadron. The working point is chosen by a fixed cut on the output of the neural network. This leads to a b-tagging efficiency of 85%.

Overlap removal

Because objects are reconstructed independently, more than one object may be reconstructed from the same detector signal. But each signal has to be assigned to exactly one object. To do this reconstruction correctly overlap removal is applied, favouring objects with higher signal purity. Tab. 5.2 shows the criteria for the overlap removal [84].

kept object	removed object	ΔR
muon	electron	0.2
electron	jet	0.4
muon	jet	0.4

Table 5.2.: Overlapping criteria used. If the distance between the two objects in the first two collumns is less than ΔR, only the object from the first collumn will be kept and the other will be removed.

5.3.2. Triggers and cut-flow

Combination of electron-muon-triggers

Since only one electron and one muon are allowed in the final state, different HLT signatures for the data-taking period between 2015 and 2018 are applied. These are

shown in Tab. 5.3.

The trigger e7mu24 fires for one likelihood based *medium* (Identification) electron with $p_T^e > 7$ GeV and one muon with $p_T^\mu > 24$ GeV, the trigger e17mu14 fires if the event contains at least one likelihood based *loose* electron with $p_T^e > 17$ GeV and one muon with $p_T^\mu > 14$ GeV and the trigger e26mu8 fires if the event contains at least one likelihood based *medium* electron with $p_T^e > 26$ GeV (for the 2016 data-taking period A-D3 $p_T^e > 26$ GeV) and one muon with $p_T^\mu > 8$ GeV.

Because the trigger efficiencies are not provided exactly down to the trigger threshold, the electron and muon-p_T selection cuts are set to 1 GeV above the trigger threshold. Also the scaling factors are binned into bin of p_T. Since the first bin of the scaling factors start at 7 GeV, this bin has to be disregarded. Otherwise, some muons may not obtain scaling factors. Thats why the selection cuts for these triggers have to be set to $p_T > 10$ GeV for electrons and muons respectively. This whole setup is shown in Fig. 5.8.
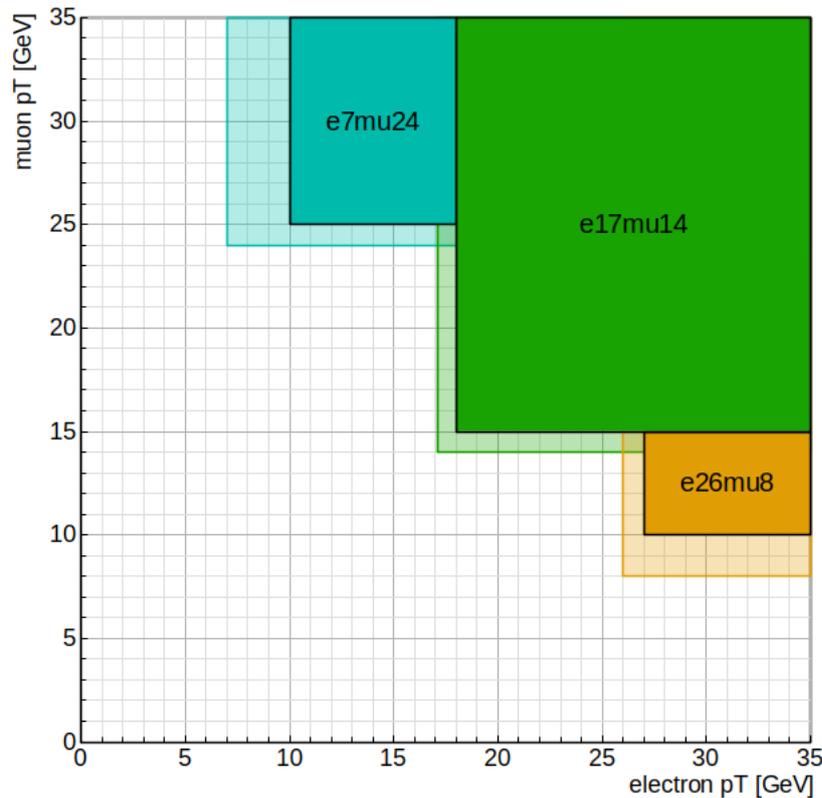

Figure 5.8.: Schematic view of the lepton trigger p_T ranges [20].

year	short name	ATLAS trigger name
2015	e7mu24	HLT_e7_lhmedium_mu24
	e17mu14	HLT_e17_lhloose_mu14
2016 period A-D3	e7mu24	HLT_e7_lhmedium_nod0_mu24
	e17mu14	HLT_e17_lhloose_nod0_mu14
	e26mu14	HLT_e24_lhmedium_nod0_L1EM20VHI_mu8noL1
2016 period D4-	e7mu24	HLT_e7_lhmedium_nod0_mu24
	e17mu14	HLT_e17_lhloose_nod0_mu14
	e26mu8	HLT_e26_lhmedium_nod0_L1EM22VHI_mu8noL1
2017	e7mu24	HLT_e7_lhmedium_nod0_mu24
	e17mu14	HLT_e17_lhloose_nod0_mu14
	e26mu8	HLT_e26_lhmedium_nod0_mu8noL1
2018	e7mu24	HLT_e7_lhmedium_nod0_mu24
	e17mu14	HLT_e17_lhloose_nod0_mu14
	e26mu8	HLT_e26_lhmedium_nod0_mu8noL1

Table 5.3.: Overview of the used HLT. The term nod0 means that no d_0 information (information about the distance between particle track and hard scattering vertex in the $x - y$ plane) is used. The term noL1 means that no L1 seed is used. The terms L1EM20VHI and L1EM22VHI show, if hadronic core isolation (H) and electromagnetic isolation (I) are applied [85, 86].

Cut-flow

For refining the event selection several cuts are applied. The optimization of these cuts was done by previous theses [18–20]. To test if the backgrounds are correctly modeled two control regions (CR) are defined. This is done by inverting a cut, which enhances a background and supresses the signal. These two regions are orthogonal to the signal region, by construction. One is called Top-CR and the other $Z \to \tau\tau$ CR

In this section an overview of all cuts is given with brief explanations. It has to be kept in mind that the cuts from the trigger thresholds are still applied. An overview of all cuts is shown in Tab. 5.4.

The lepton identificantion for both muons and electrons are set to the working point *medium* [79].

The lepton isolation variables quantify the energy deposition in the cone ΔR around the lepton candidate. There are two different isolations used. The calorimeter isolation detects clusters of transverse energy depositions. The track isolation is obtained by summing the transverse momenta in a cone around the observed lepton track. Here the working *tight* is chosen for both lepton candidates. This working point has an efficiency of 90% for prompt leptons with $E_T = 40$ GeV [79]. With the help of this criteria backgrounds from heavyquark induced leptons and fake leptons from QCD processes are reduced [79, 80, 87].

The *b*-tagging is used as described in Sec. 5.3.1. For the Top-CR the *b*-tagging is inverted. This enhances the backround coming from *t* processes and supresses the signal.

The cut on E_T^{miss} also reduces the background coming from QCD processes. Here different mass hypotheses are treated differently. For the mass points from 20 GeV to 70 GeV the cut $E_T^{miss} < 50$ GeV is used. For the mass hypotheses 80 GeV and 90 GeV the cut $E_T^{miss} < 50$ GeV is applied [20].

The next cut is the cut on the total transverse mass:

$$m_T^{tot} = \sqrt{(p_T^e + p_T^\mu + E_T^{miss})^2 - (\vec{p}_T^e + \vec{p}_T^\mu + \vec{E}_T^{miss})^2}. \tag{5.2}$$

As this mass uses E_T^{miss} it determines the mass of the mother particle with a higher precision, than the simple di-lepton mass. With a cut of $m_T^{tot} < 45$ GeV for the lower mass hypotheses and CRs and $m_T^{tot} < 65$ GeV for the higher mass hypotheses background from top, diboson and Z processes are supressed.

As explained in Sec. 5.2.1, the signal process only differs with respect to angular distribution from the $Z \to \tau\tau$ backfround. From this fact the cuts onto ΔR are derived. In the signal region the cuts are set to be $\Delta R < 0.7$ for the low mass hypotheses and $\Delta R < 1.0$ for the higher mass hypotheses. In the $Z \to \tau\tau$-CR this cut is set to $\Delta R > 1.4$. This supresses the signal in the CR leading to $Z \to \tau\tau$ decays as the main background.

Variable	Signal region (20 - 70 Gev/80 - 90 GeV)	$Z \to \tau\tau$-CR	Top-CR
ID$_e$	*medium*		
ID$_\mu$	*medium*		
Isolation$_e$	*tight*		
Isolation$_\mu$	*tight*		
b-tagging	no *b*-jets		at least one *b*-jet
E_T^{miss}	> 50 GeV/> 30 GeV	> 30 GeV	
m_T^{tot}	< 45 GeV/< 65 GeV	< 65 GeV	
ΔR	< 0.7 / < 1.0	> 1.4	< 1.0

Table 5.4.: Overview of all applied cuts for the signal region and the two CRs

5.4. Fake Factor estimation

In the Top and $Z \to \tau\tau$ control regions a background seems to be missing, especially in the low missing transverse energy region. This indicates another source of background not estimated by the Monte-Carlo predictions. The additional backgound arises from lepton candidates originating from quark- or gluon-initiated jets. The probability of a jet being misidentified as a lepton is not modeled well enough and simulation of the multijet events is not statistical significant, due to high cross-

sections and small acceptances. Thus a data driven method needs to be applied. This analysis uses a method, which is similar to the method explained in [88].

5.4.1. Nominal fake factor method

To estimate this Multijet background a fake factor method is employed. This method uses events from additional control regions, where muon isolation are required to be *loos* but not *tight*. These are called fake regions (FR).

This region gets split up into two regions, where fake factors (FF) get measured. The first region is the enumerator region (A). The second one is the denominator region (B). In A just the muon isolation fails and electron isolation and ID passes the requirements, whereas in B either the electron isolation or ID fails additionally to the muon isolation. These regions are chosen to maximize the fraction of QCD-events. After substracting the true lepton contamination from data in these regions, the FF is calculated:

$$FF = \frac{N(\text{pass electron isolation and ID})}{N(\text{fail electron isolation and ID})}\bigg|_{\mu-\text{fail}} \tag{5.3}$$

These FF are binned in an arbitrary variable. In this case p_{T}^e is used. Afterwards the FF are applied onto the denominator region of the actual control- and signal-regions. Again only the Monte Carlo substracted data is used for these calculations:

$$\begin{aligned} N_{Multijet} &= N(\text{pass electron isolation and ID})|_{\mu-\text{pass}} \\ &= FF \cdot N(\text{fail electron isolation and ID})|_{\mu-\text{pass}} \end{aligned} \tag{5.4}$$

Because the missing background is only visible for low-p_{T}^e, the FFs only get calculated for $p_{\text{T}}^e < 40$GeV. A schematic illustration of the method is shown in Fig. 5.9.

5.4.2. Systematics on fake background

The FFs are calculated in discrete bins of p_{T}^e. These FFs are smoothed by a smoothing algorithm described in [89]. Centers of bins are then linearly connected allowing a smoother interpolation in between bins. Also the bin edges are chosen in a way that the statistical uncertainties are small after the interpolation. The bin-edges are shown in Tab. 5.5

To calculate uncertainties on the FFs three sources of uncertainties are considered, the statistical uncertainties on data and Monte Carlo and the systematic uncertainties on Monte Carlo. To apply the correct statistical uncertainty, the statistical uncertainties are decorrelated for each bin. This is simply done by taking each bin uncertainty individually for further calculations. The systematic uncertainties on the substracted Monte Carlo backgrounds are added in quadrature and combined into a single uncertainty.

As a result seen in Fig. 5.10 the FFs for the $Z \to \tau\tau$-, Top- and signal-region are statistically compatible and ready for application.
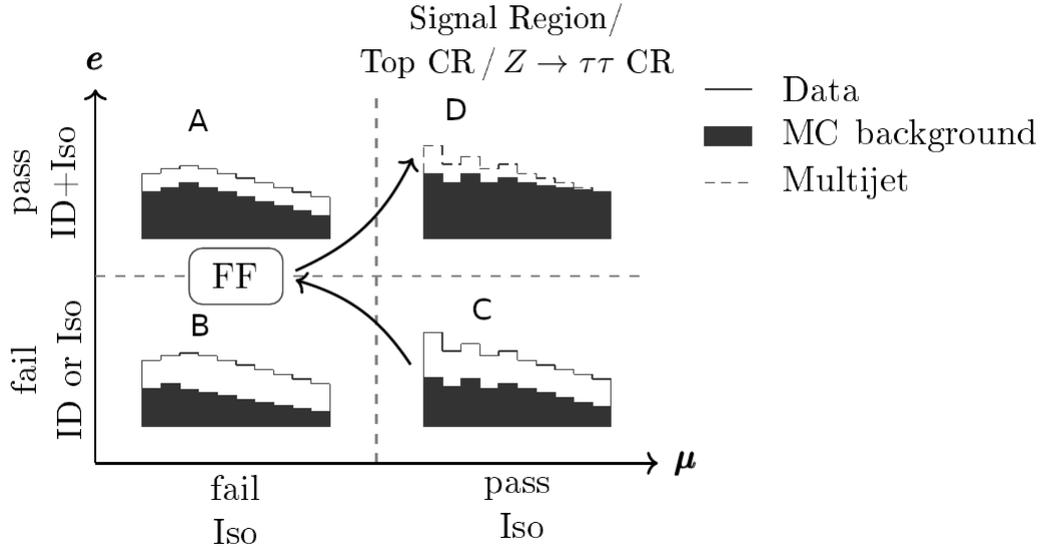
Figure 5.9.: schematic view of the workflow for the calculation of fake factors

After the application the new background (called Multijet) is estimated. Plots of both signal regions with this background are shown in Fig. 5.11 and Fig. 5.12. Additionally Fig. 5.13 and **??** show the two CRs with the Multijet background.. In Tab. 5.6 the event numbers of the signal and control regions together with the resulting Multijet background can be found. Plots from the A, B and C region can be found in Appendix B together with the respective event numbers.

	Bin-edges/GeV
Signal-region	$\{10.0, 10.5, 11.0, 12.0, 13.0, 14.0, 15.0,$ $16.0, 17.0, 18.0, 19.0, 20.0, 25.0, 30.0, 35.0, 40.0\}$
$Z \to \tau\tau$ CR	$\{10.0, 10.5, 11.0, 12.0, 13.0, 14.0, 15.0, 16.0,$ $17.0, 18.0, 19.0, 20.0, 25.0, 30.0, 40.0\}$
TOP-CR	$\{10.0, 10.5, 11.0, 12.0, 14.0, 18.0, 20.0, 30.0, 40.0\}$

Table 5.5.: Bin-edges for fake factor calculation

Region	SR m_A=(20-70) GeV	SR m_A=(80-90) GeV	$Z \to \tau\tau$-CR	Top-CR
$Z \to \tau\tau$	1330	5281	64899	1090
Top	158	882	5065	15749
$W \to l\nu$	55	435	25331	171
Diboson	134	630	4191	157
SM Higgs	89	462	4077	106
$Z \to ee/\mu\mu$	18	163	2063	67
Multijet	195	1315	5168	203
Sum	1784	7854	105625	17340
Data	–	–	100095	18522

Table 5.6.: Event-numbers in the resulting regions
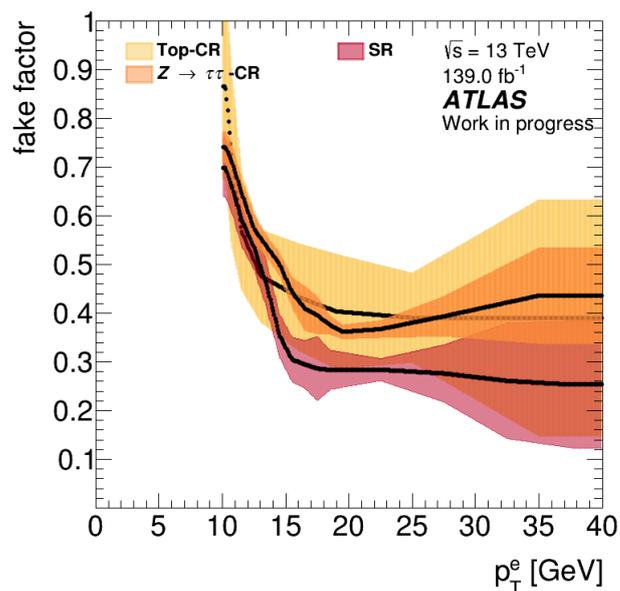
Figure 5.10.: Calculated FFs for $10\,\mathrm{GeV} < p_\mathrm{T}^e < 40\,\mathrm{GeV}$
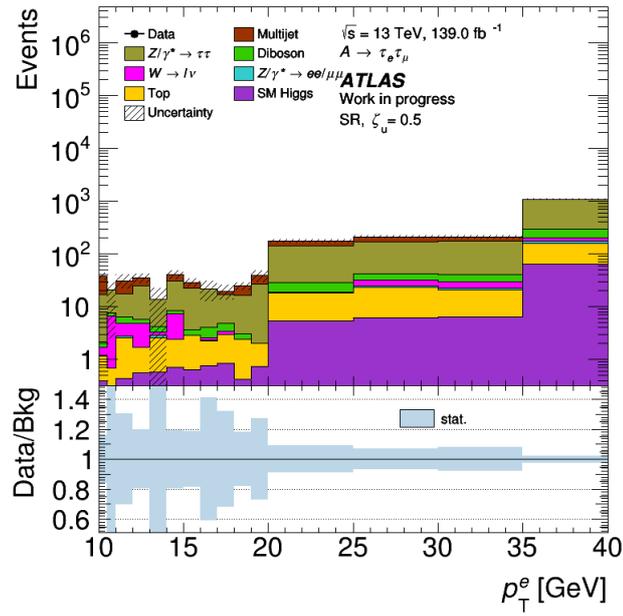
Figure 5.11.: Signal region for A masses of 40, 50, 60 and 70 GeV with Multijet Background
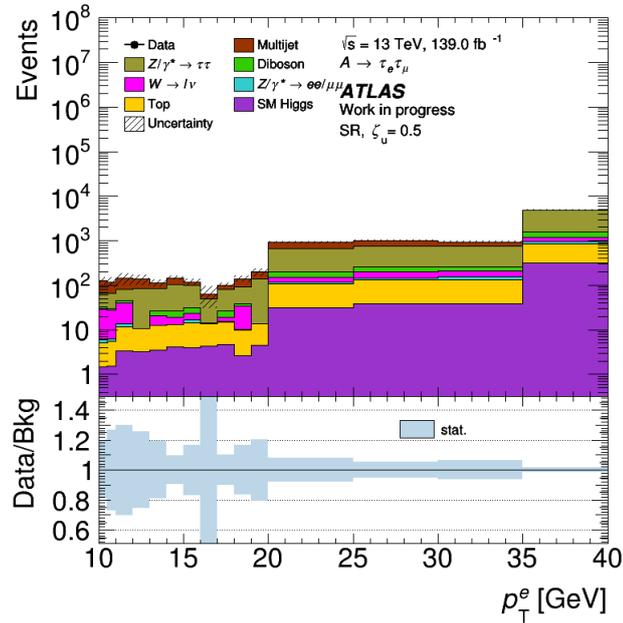
Figure 5.12.: Signal region for A masses of 80 and 90 GeV with Multijet Background
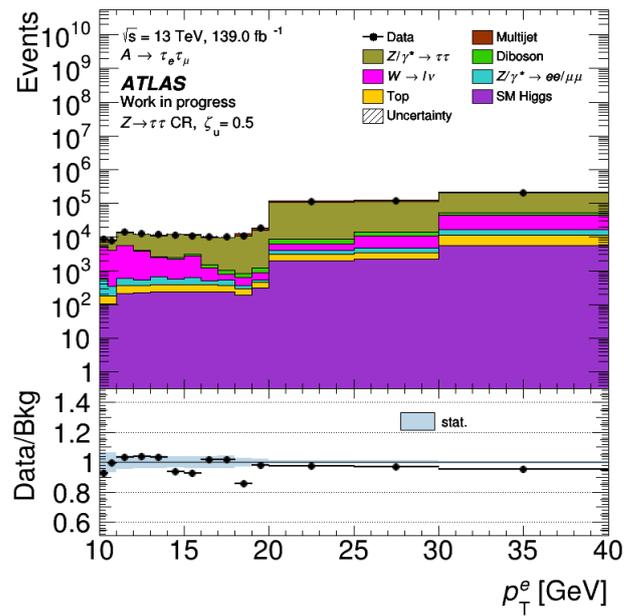
Figure 5.13.: $Z \to \tau\tau$-CR with Multijet Background
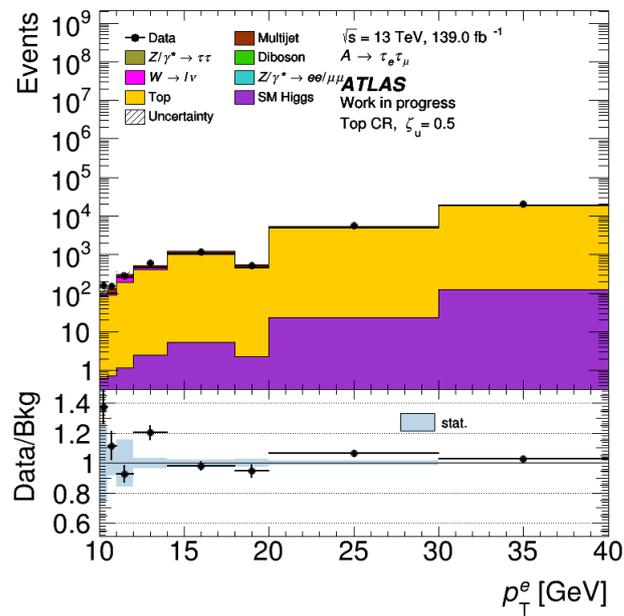
Figure 5.14.: TOP-CR with Multijet Background

6. Introduction to neural networks for the analysis

This chapter aims to give an introduction into how neural networks are used as a classifier in particle physics. The goal of this type of multivariate analysis is to classify events into signal and background categories. This is done to either introduce a cut on the obtained score the neural net calculates from kinematic properties of the viewed events.

At first a brief introduction in deep neural nets and their training is given. Afterwards the results of applying this network onto the events from the signal region and $Z \to \tau\tau$ region are shown.

6.1. Basics of neural networks

Artificial neural networks [90, 91] were designed to imitate biological neural networks like the human brain. Since computing power vastly increased in the last years, this machine learning technique proved to be a powerful tool not only in particle physics. A deep feed-forward neural network is organized into layers of neurons. For each Layer of neurons a simple calculation is executed:

$$a_j^l = A \left(\sum_k w_{jk}^l a_k^{l-1} + b_j^l \right) = A(z_j^l), \qquad (6.1)$$

where l is the layer, the neuron is located in, a is the output of the neuron, A is a non-linear activation function, w are weights, j is the number of the neuron in the layer l and k is the number of the neuron in layer $l-1$. In this case A is the sigmoid function:

$$A(x) = \frac{1}{1 + e^{-x}} \qquad (6.2)$$

The first layer of neurons uses a vector of variables as input. These variables are chosen in a way that important properties of the event are described properly by this set of variables.

A schematic illustration of this layout is depicted in Fig. 6.1.

6.1.1. Training of deep neural networks

The neural network "learns" its features while it is trained. The training strategies may vary depending on the task and available datasets for this task. If datasets,
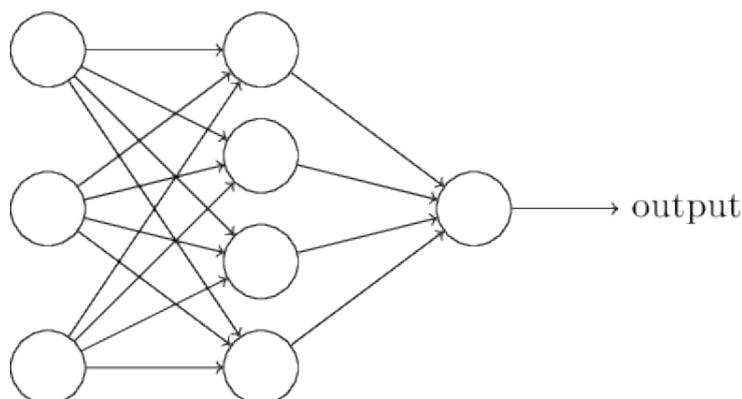
Figure 6.1.: Schematic illustration of neurons organized in three two layers and an additional output layer with one neuron [91].

where the desired outputs are known, do exist, a supervised training method can be used.

The datasets need to be organized and prepared in a certain way, before training is started. The datasets get split up into training, validation and test datatsets. The training datasets are used in the actual training, which is described later. The validation datasets are used to check if the network still performs well for data it has not seen during training. The application of the networks is then performed onto the test dataset to ensure the training was not biased by the training and validation datasets. The network will perform best if the training dataset has the same contribution ratios as the datasets it will be applied on later. To ensure this, each entry will be weighted corresponding to their later contribution.

The loss function

To obtain a quantity of how well a network performs, a so called loss function has to be defined. This function has to have cerain properties. It should have a minimum, which is achieved if a perfect prediction was obtained by the network. It also needs to be differentiable, as the derivatives are needed for the training. The perfomance of the network can then be quantified by the mean value of the single losses of each entry:

$$C = \frac{1}{n} \sum_x C_x, \tag{6.3}$$

with C being the loss over all entries, n the number of entries and C_x the loss of the entry x. In this thesis the binary cross-entropy is used as loss function:

$$C_x = y \ln a + (1 - y) \ln 1 - a, \tag{6.4}$$

with a being the output of the network and y being the desired output. The binary cross entropy or log loss function is desireable to use, because here the values a can be interpreted as probabilities. Since this thesis aims to create a classification of events into two categories (signal and background), the output of the network is a single number between 0 and 1. This output can be interpreted as the probability of the event being a signal event. 1 being 100 % sure it is a signal event and 0 being sure it is a background event.

The goal of training is now to find a certain set of weights and biases, which minimize the loss function.

The Adam optimizer

For deep neural networks with multiple layers and a great number of neurons it is practically impossible to minimize the loss function analytically. To find the minimum nevertheless optimizers are used. The most prominent optimizer is the stochastical gradient descent, because it was developed first.

In principle most optimizers work in the same way. A nice visualization of this problem is to think of the loss function as a complex landscape in a multidimensional space (see Fig. 6.2). When placing an object into the landscape it should gravitate towards the minimum. The "placing" is done by initializing the weights and biases. This is mostly done by randomizing them around zero with a gaussian distribution. Afterwards the partial derivatives for a training entry, the obtained value from the net a and the desired value y are calculated with respect to the weights and biases. This vector can then be interpreted as the direction the ball would roll upwards. After normalization this vector gets multiplied by a negative factor $-\eta$. This flips the direction (hopefully) towards the valley of the loss landscape. η is here called learning rate and is the distance the ball rolls. This is then repeated until a minimum is found.

While this would work, it will be necessary to calculate the gradient of the loss function for every training input. To avoid this the training data is comibined into mini-batches. This alters the loss function with m being the size of a mini-batch:

$$C = \frac{1}{n} \sum_x C_x \approx \frac{1}{n} \sum_j = 1^m C_j \tag{6.5}$$

After every input from the training dataset is used in a mini-batch, one so called training epoch is over and it starts all over.

This method seems to work quite well for different problems, but it may happen, that the network will get stuck in a local minimum. There are several techniques to avoid this problem. One of these is using a momentum based optimizer. The Adam optimizer is one of these and is provided by the keras package [92].

This optimizer differs from the stochastical gradient descent because of a changed update rule after a training epoch. For this two additional values are defined. The first and second moment vectors m_t and v_t:
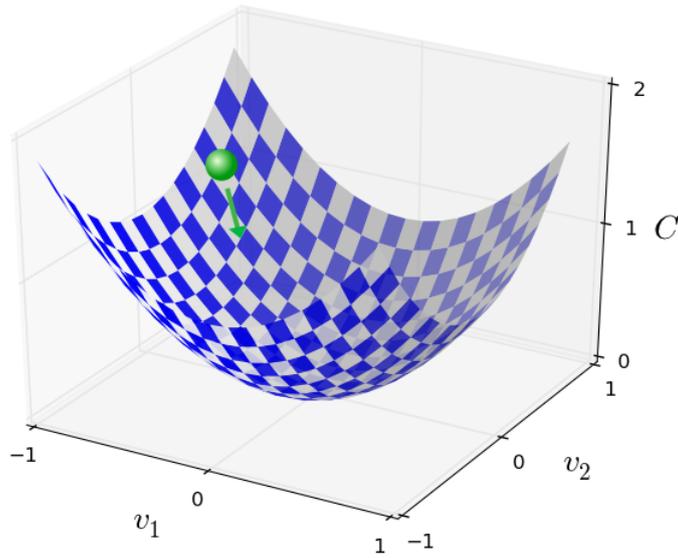
Figure 6.2.: Schematic illustration of the loss landscape with a ball rolling down into a valley as visualization of the training process [91].

$$
\begin{aligned}
m_t &= \beta_1 m_{t-1} + (1 - \beta_1) g_t \\
v_t &= \beta_2 v_{t-1} + (1 - \beta_1) g_t^2
\end{aligned}
\tag{6.6}
$$

Here t is the current epoch, $0 \leq \beta_1 < 1$ and $0 \leq \beta_2 < 1$ are exponential decay rates for the momenta estimates and $g_t = \nabla_{theta} C_t(\theta_{t-1})$ is the gradient of the loss funtion with respect to the parameter set θ (weights and biasses). Note that the squared gradient g_t^2 indicates the elementwise square $g_t \odot g_t$.

Afterwards the momenta are bias-corrected. This has to be done, because the momenta are initialized at zero, which leads to a bias. This correction looks like this:

$$
\begin{aligned}
\hat{m}_t &= \frac{m_t}{1 - \beta_1^t} \\
\hat{v}_t &= \frac{v_t}{1 - \beta_2^t}
\end{aligned}
\tag{6.7}
$$

In the end an update rule for the parameter vector θ is defined:

$$
\theta_t = \theta_{t-1} - \eta \frac{\hat{m}_t}{\sqrt{\hat{v}_t} + \epsilon}
\tag{6.8}
$$

With the help of the newly defined momenta terms, the network is able to conserve some momentum while fitting one epoch and use it later on to "jump" out of a local minimum.

6.2. Application of neural networks to the analysis

The goal is to classify measured events as signal or background. For this purpose a parameterized neural network (PNN) is used. The input parameters are 14 kinematic variables characterizing the event:
$E_T^{miss}, p_T^e, p_T^\mu, \eta_e, \eta_m u, \Phi_e, \Phi_\mu, m_T^{tot}, m_{MMC}, p_T^{higgs}, m_{leplep}, \Delta R, \Delta\Phi_{met}^{leadlep}$
and $\Delta\Phi_{met}^{subleadlep}$.

To account for the different mass hypotheses a 15th parameter is defined. This parameter is the underlying mass hypotheses $m_A/100\,\text{GeV}$.

To train the PNN different datasets are used. The signal dataset uses the generated Monte Carlo data of the $A \to \tau\tau$ decays. Here the mass parameter is set to the mass hypothesis, which was used to generate the Monte Carlo samples.

The background dataset consists of five different datasets. Four of these are also Monte Carlo generated: the $Z \to \tau\tau$, the top dataset, the diboson dataset and the "others" dataset. The last one contains all other decays not included in the first three datasets. All events are selected with the cuts for the high mass signal hypothesis from Sec. 5.3.2, to ensure a distribution similar to the one, the PNN is applied on in the end. The fifth background dataset is the QCD dataset. Because for this background no Monte Carlo samples can be generated, data has to be used for training. A simple solution is to use events from the B region introduced in Sec. 5.4. This region is filled nearly exclusively with QCD events, since the prompt-lepton contamination is only around 4.2 %. To model the distribution correctly the loss function has to be reweighted according to the contribution of the underlying event. The Monte Carlo events are reweighted by their Monte Carlo weights and the QCD events by a the ratio $\frac{D}{B}$. This makes sure the contribution of the QCD events is the same as in the signal region D.

For the background events a random mass hypothesis is chosen from the eight mass points (20 GeV, 30 GeV, 40 GeV, 50 GeV, 60 GeV, 70 GeV, 80 GeV, 90 GeV).

Basic layout of the PNN

As mentioned previously the PNN uses 15 parameters, which leads to 15 input nodes. These are the forwarded through four fully connected layers with ten neurons each. Each neuron applies the sigmoid function from Eq. 6.2. The last layer connects the ten neurons from the second to last layer to one neuron. Again the sigmoid function is applied, to obtain values in between one and zero. An illustration of this model is shown in Fig. 6.3. This model is then trained for 200 epochs.
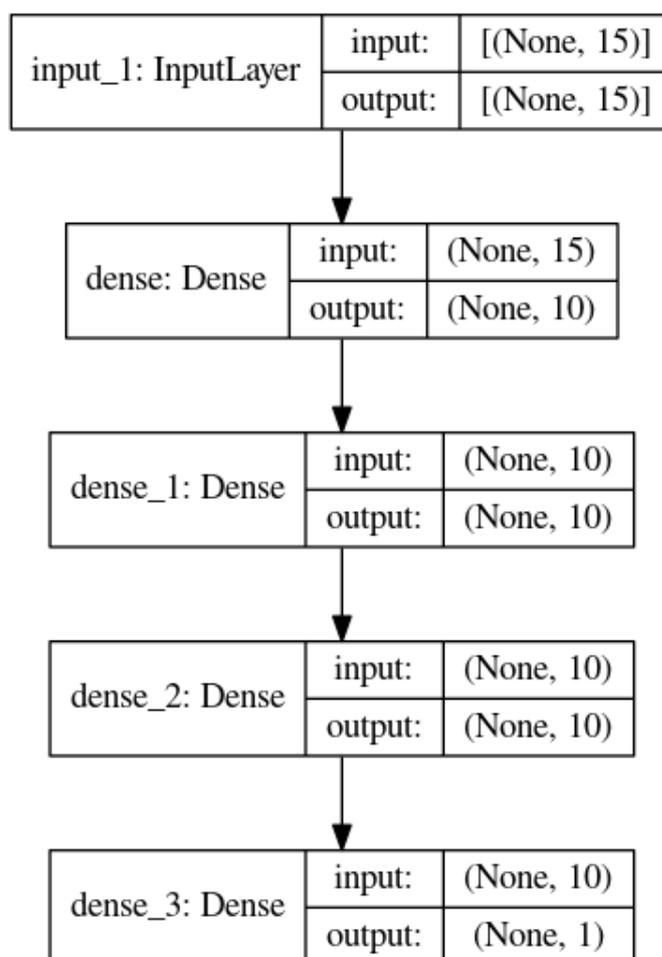
Figure 6.3.: PNN model with four hidden layers of ten neurons each.

k-folding cross validation

A problem for using a neural network for a statistical anlysis arises, because the data used for training is also used for the statistical tests and limit setting. As this data is shown directly to the neural network a bias on this data is created. As mentioned before the datasets have to be divided into training, validation and test datasets. Since the training and validation data are used to develop the neural network, these can not be used for application. Only the test dataset can be used. But this would reduce the statistics of the analysis drastically. The solution to this problem is the k-folding cross validation. Here the complete dataset is split up into k different datasets, called k-folds. In this case five different PNNs are trained. Each network uses different k-folds as training, validation and test datasets. In this analysis the data is split into five k-folds resulting in five independent neural networks. This is shown in Fig. 6.4.
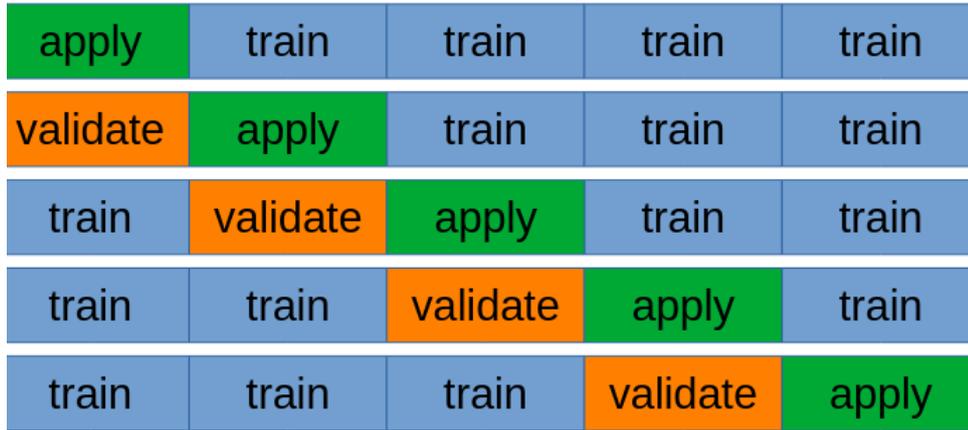
Figure 6.4.: *k*-folding model with five different *k*-folds. Each has its own application (test) dataset, a different validation dataset and different training datasets [93].

The downside of this method is the computing time which increases proportional to *k*. Thus the number of *k*-folds should be kept low as long as the training data is still statisically feasible.

Learning rate scheduler and ROC-curves

Since the PNN acts as a classifier, one way to evaluate the performance of the network are the ROC-curves. Roc-curves implement a cut in the resulting score and classify every event above the cut threshold as signal. This cut is then varied from zero to one. For every variation the portion of correctly identified events above the threshold (true positive rate) is plotted against the portion of falsely identified events (false positive rate). Because a perfect classification would result in a square-shaped ROC-curve with an area of 1, the area under the ROC-curve (AUC) is a good quantity for determining the perfomance of the PNN. The ROC curve is also directly tied to the significance as the significance is approximately calculated by:

$$\sigma = \frac{N_{\text{signal}}}{\sqrt{N_{\text{background}}}} \tag{6.9}$$

After the score cut is applied the ratio of the new obtained significance to the initial significance can be expressed in terms of true positive rate and false positive rate.

$$\frac{\sigma_{\text{NN}}}{\sigma_{\text{initial}}} = \frac{\text{True positve rate}}{\sqrt{\text{False positive rate}}} \tag{6.10}$$

Eventhough a momentum-based optimizer was used, the single *k*-folds can still converge to a local minimum. To prevent this a learning rate scheduler is applied.

This mechanism sets the learning rate depending on the epoch. Best results were obtained by resetting the learning rate after 20 epochs (See Fig. 6.5). The AUC depicted in Fig. 6.6 shows that the different k-folds arrive in a similar performing minimum in the end. The differences which occur in the first 150 epochs are fixed by the learning rate scheduler in the epochs at the end and an AUC of roughly 0.93 is achieved.
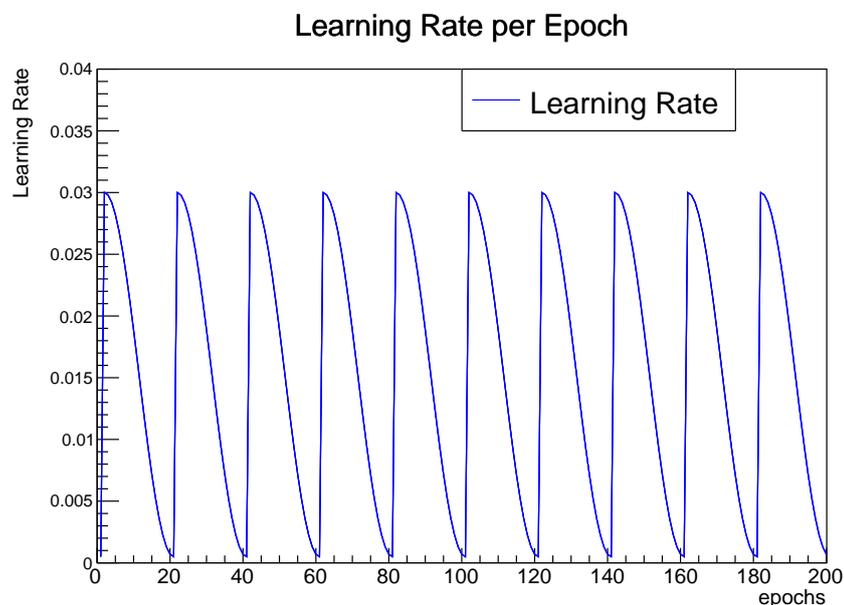

Figure 6.5.: Learning rate schedule over 200 epochs. The learning rate is reset to 0.03 after 20 epochs and it decreases afterwards with a cosine function

Results after applying the PNN

After the PNN is applied onto Monte Carlo in the signal region. The score can be plotted and analyzed. The plot for a mass hypotheses of 60 GeV is shown in Fig. 6.7. The PNN seems to perform well based on this plot, since th signal accumulates at high scores just below one and the backgrounds peak at zero. Additional PNN score plots are shown in Appendix C.

With those plots and with Eq. 6.10 significance factors can be calculated for every mass hypotheses. These are shown in Fig. 6.8. The resulting significance peaks for every mass at a low false positve rate. The peaks range from 2.7 for $m_A = 20$ GeV to 1.3 for $m_A = 90$ GeV. Generally the classification works best for the low-mass hypotheses, since the high-mass hypotheses approach the Z-peak, which makes the signal events nearly indistuingishable from $Z \to \tau\tau$ background.
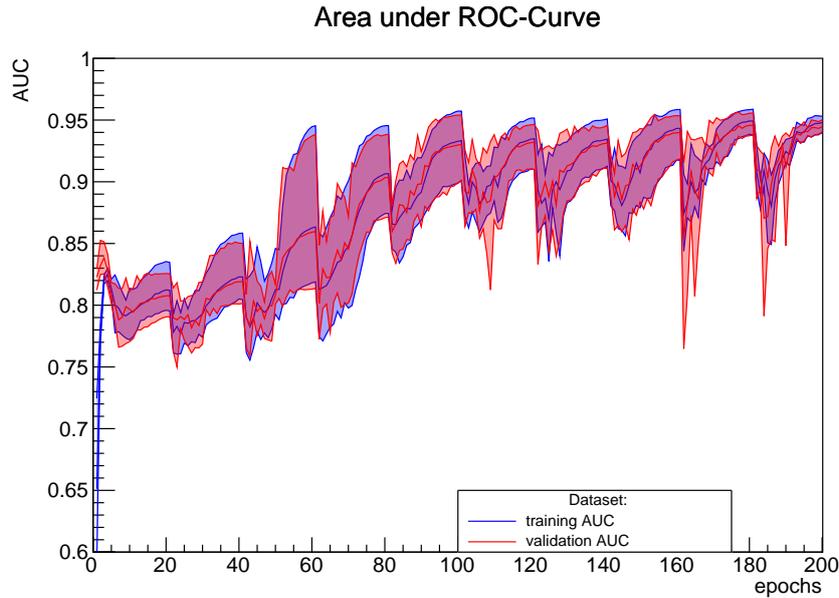
Figure 6.6.: AUC of training data (blue) and validation data (red) over 200 epochs. The lower border of the error bands shows the worst performing *k*-fold and the upper border the best performing *k*-fold

After the score in the signal region was inspected, the score in the $Z \to \tau\tau$ CR has to be analyzed. In Fig. 6.9 the score obtained by the PNN with the mass parameter set to $60\,\mathrm{GeV}$ in this CR is shown. Here a mismodelling of the Monte Carlo background can be seen. The data undershoots the Monte Carlo backgrounds substancially for high scores. Due to this mismodelling the fake factor method can not be applied, since it is dependent on well modelled Monte Carlo backgrounds.

The most probable reason for this is the existence of negative Monte Carlo weights. Thes can arise because of negative interferences from higher orde loop contributions. The negative Monte Carlo weights flip the sign of the loss function. Since the optimizer minimizes the loss function, the absolute value of the loss will rise. This would mean a Monte Carlo event with a negative weight will get classified completely wrong, since the absolute value of the loss function can get extremely high. The data events are unweighted, meaning the effect can not be reproduced with measured data. This would give a coherent explanation of the undershoot of data for the high score regions.
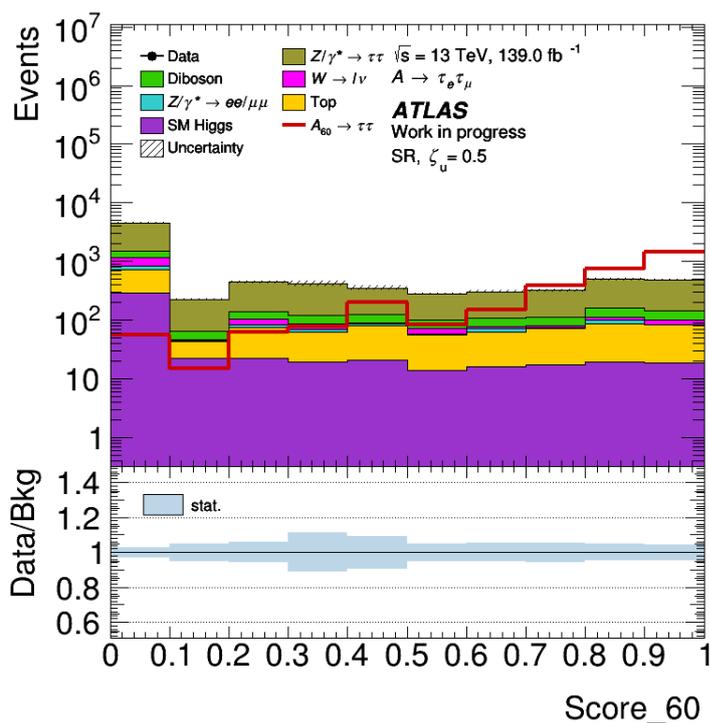
Figure 6.7.: Plot of the score obtained by the PNN with the mass parameter set to 60 GeV, applied on Monte Carlo backgrounds and the 60 GeV signal Monte Carlo in the signal region
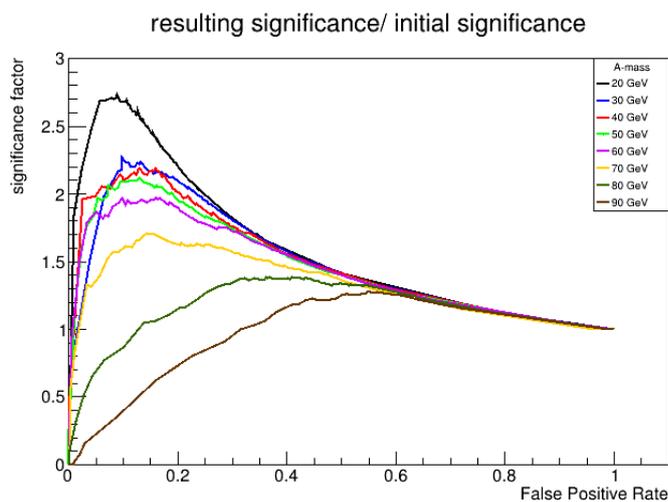

Figure 6.8.: Significance enhancement factors for every mass hypotheses plotted against the false negative rate
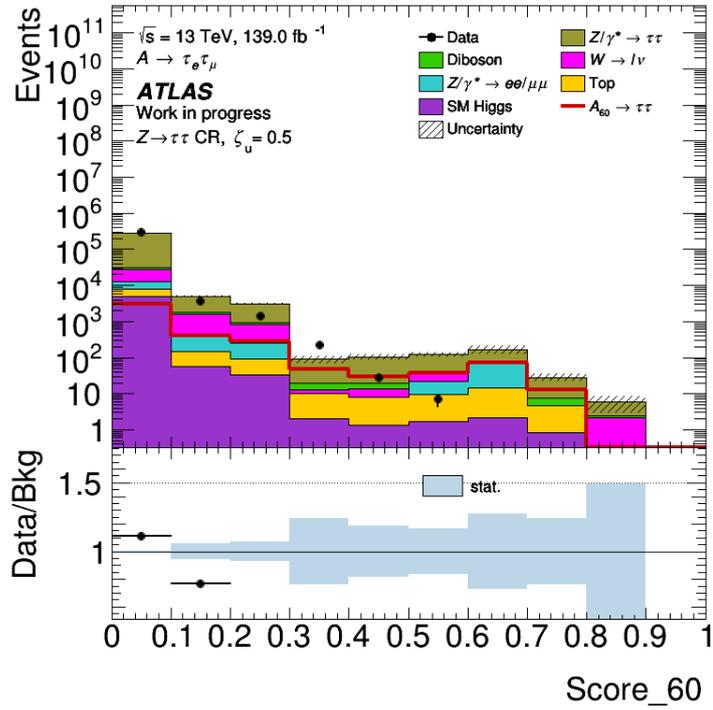
Figure 6.9.: Plot of the score obtained by the PNN with the mass parameter set to 60 GeV, applied on Monte Carlo backgrounds and the 60 GeV signal Monte Carlo in the $Z \to \tau\tau$ CR

7. Conclusion and outlook

To conclude this thesis limits are shown in Fig. 7.1. These are limits on the production cross-section of the A boson. Here fake factors have been taken into account. The black dotted line indicating the expected limit with its uncertainty bands. The green band indicates the area of $1\,\sigma$ and the yellow band $1\,\sigma$. The red line shows the expected limits without accounting the Multijet background. As expected the limits get worse with the new background, since another background source with additional uncertainties was added. Additionally the plot has its switch in between the to signal regions still at A boson masses of $m_A = 70\,\mathrm{GeV}$. This needs to be set to $m_A = 80\,\mathrm{GeV}$ for future studies, to show that at $80\,\mathrm{GeV}$ the higher mass-dependent cuts are needed. New mass points at $100\,\mathrm{GeV}$ and $110\,\mathrm{GeV}$ will be added too.

The fake factor method seems to be working well and reduces the overshoot of data at low p_T. The whole process of generating the Multijet background has to be repeated, if changes on the Monte Carlo samples or isolation and ID criteria were made, because the whole calculation depends greatly on these three criteria.

Also an implementation of a working neural network framework was done. The application of the neural networks does not produce a good agreement between Monte Carlo simulation and data. A possible problem could be negative Monte Carlo weights, which invert the loss function. Also a simple mismoddeling of Monte Carlo data, which gets amplified by the PNN could be the source of this problem. In the future further studies need to be conducted to indentify the problem correctly. Possible solutions could be e.g. ignoring the events with negative weight or taking the absolute value of the weight. Also different regularization patterns can be tested. These can account for statistical deviations in training and test data, which could smear the mismoddeling enough to make it disappear.

Nevertheless the analysis is in a highly advanced state. After approval the data in the signal region can be unblinded soon. After the unblinding not only expected results can be shown, but also real results.
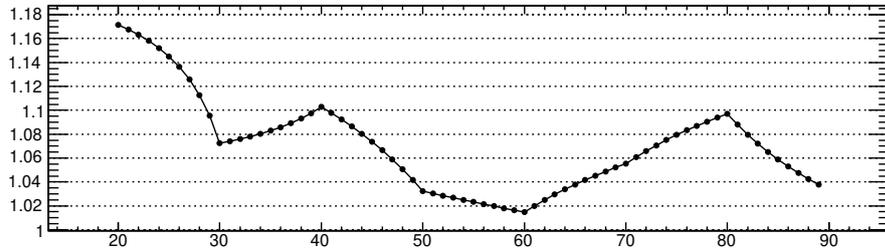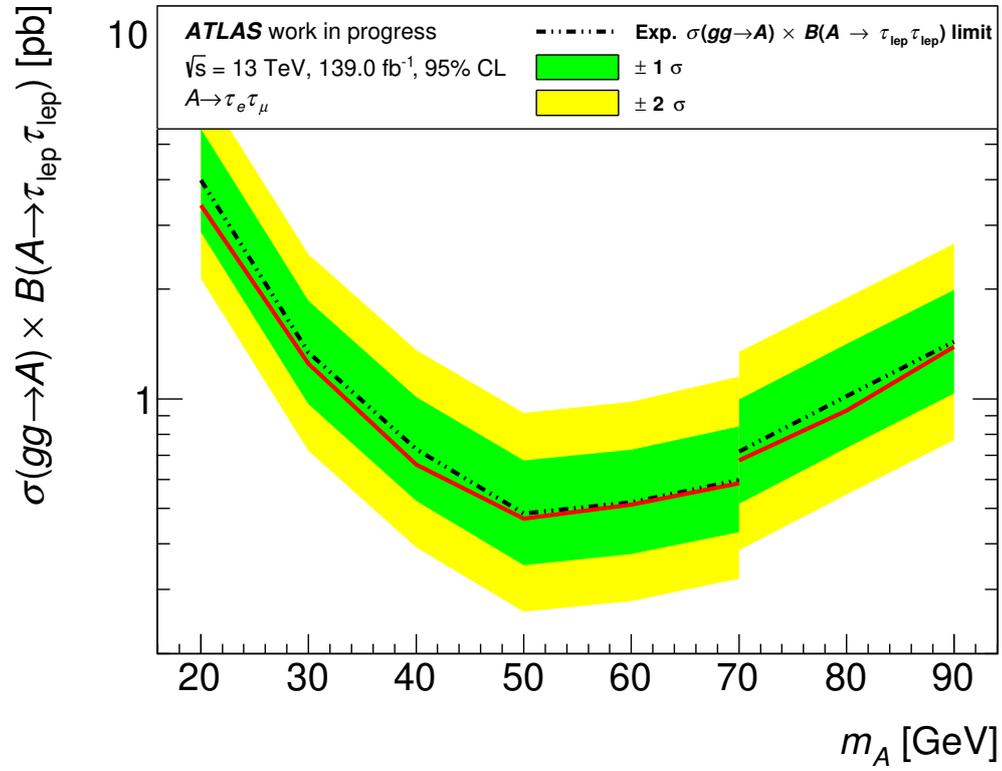
Figure 7.1.: Upper limits on the production cross section of the A boson, with the 1σ (green) and 2σ (yellow) error bands. This was done with the newly added Multijet background. As comparison the limits without this background are depicted as red line.

A. Monte Carlo Samples

This section contains a list of all the MC samples used in the analysis

A.1. mc16a

gluon-fusion A production

```
mc16_13TeV.346025.Pythia8EvtGen_A14NNPDF23LO_ggA60_tautau_leplep.deriv.DAOD_HIGG3D1.e7122_a875_r9364_p4164

mc16_13TeV.346026.Pythia8EvtGen_A14NNPDF23LO_ggA70_tautau_leplep.deriv.DAOD_HIGG3D1.e7122_a875_r9364_p4164
mc16_13TeV.346027.Pythia8EvtGen_A14NNPDF23LO_ggA80_tautau_leplep.deriv.DAOD_HIGG3D1.e7122_a875_r9364_p4164
mc16_13TeV.346028.Pythia8EvtGen_A14NNPDF23LO_ggA90_tautau_leplep.deriv.DAOD_HIGG3D1.e7122_a875_r9364_p4164
mc16_13TeV.346375.Pythia8EvtGen_A14NNPDF23LO_ggA50_tautau_leplep.deriv.DAOD_HIGG3D1.e7122_a875_r9364_p4164
mc16_13TeV.451705.Pythia8EvtGen_A14NNPDF23LO_ggA40_tautau_leplep.deriv.DAOD_HIGG3D1.e8139_a875_r9364_p4164
mc16_13TeV.801162.Py8EG_A14NNPDF23LO_ggA20_tautau_11314.deriv.DAOD_HIGG3D1.e8307_a875_r9364_p4164
mc16_13TeV.801163.Py8EG_A14NNPDF23LO_ggA30_tautau_11314.deriv.DAOD_HIGG3D1.e8307_a875_r9364_p4164
mc16_13TeV.801827.Py8EG_A14NNPDF23LO_ggA100_tautau_11314.deriv.DAOD_HIGG3D1.e8307_a875_r9364_p4164
mc16_13TeV.801828.Py8EG_A14NNPDF23LO_ggA110_tautau_11314.deriv.DAOD_HIGG3D1.e8307_a875_r9364_p4164
```

$Z/\gamma* \to \tau\tau$+jets

```
mc16_13TeV.364128.Sherpa_221_NNPDF30NNLO_Ztautau_MAXHTPTV0_70_CVetoBVeto.deriv.DAOD_HIGG3D1.e5307_s3126_r9364_p4164

mc16_13TeV.364129.Sherpa_221_NNPDF30NNLO_Ztautau_MAXHTPTV0_70_CFilterBVeto.deriv.DAOD_HIGG3D1.e5307_s3126_r9364_p4164
mc16_13TeV.364130.Sherpa_221_NNPDF30NNLO_Ztautau_MAXHTPTV0_70_BFilter.deriv.DAOD_HIGG3D1.e5307_s3126_r9364_p4164
mc16_13TeV.364131.Sherpa_221_NNPDF30NNLO_Ztautau_MAXHTPTV70_140_CVetoBVeto.deriv.DAOD_HIGG3D1.e5307_s3126_r9364_p4164
mc16_13TeV.364132.Sherpa_221_NNPDF30NNLO_Ztautau_MAXHTPTV70_140_CFilterBVeto.deriv.DAOD_HIGG3D1.e5307_s3126_r9364_p4164
mc16_13TeV.364133.Sherpa_221_NNPDF30NNLO_Ztautau_MAXHTPTV70_140_BFilter.deriv.DAOD_HIGG3D1.e5307_s3126_r9364_p4164
mc16_13TeV.364134.Sherpa_221_NNPDF30NNLO_Ztautau_MAXHTPTV140_280_CVetoBVeto.deriv.DAOD_HIGG3D1.e5307_s3126_r9364_p4164
mc16_13TeV.364135.Sherpa_221_NNPDF30NNLO_Ztautau_MAXHTPTV140_280_CFilterBVeto.deriv.DAOD_HIGG3D1.e5307_s3126_r9364_p4164
mc16_13TeV.364136.Sherpa_221_NNPDF30NNLO_Ztautau_MAXHTPTV140_280_BFilter.deriv.DAOD_HIGG3D1.e5307_s3126_r9364_p4164
mc16_13TeV.364137.Sherpa_221_NNPDF30NNLO_Ztautau_MAXHTPTV280_500_CVetoBVeto.deriv.DAOD_HIGG3D1.e5307_s3126_r9364_p4164
mc16_13TeV.364138.Sherpa_221_NNPDF30NNLO_Ztautau_MAXHTPTV280_500_CFilterBVeto.deriv.DAOD_HIGG3D1.e5313_s3126_r9364_p4164
mc16_13TeV.364139.Sherpa_221_NNPDF30NNLO_Ztautau_MAXHTPTV280_500_BFilter.deriv.DAOD_HIGG3D1.e5307_s3126_r9364_p4164
mc16_13TeV.364140.Sherpa_221_NNPDF30NNLO_Ztautau_MAXHTPTV500_1000.deriv.DAOD_HIGG3D1.e5307_s3126_r9364_p4164
mc16_13TeV.364141.Sherpa_221_NNPDF30NNLO_Ztautau_MAXHTPTV1000_E_CMS.deriv.DAOD_HIGG3D1.e5307_s3126_r9364_p4164
mc16_13TeV.364210.Sherpa_221_NN30NNLO_Ztt_M110_40_MAXHTPTV0_70_BVeto.deriv.DAOD_HIGG3D1.e5421_s3126_r9364_p4164
mc16_13TeV.364211.Sherpa_221_NN30NNLO_Ztt_M110_40_MAXHTPTV0_70_BFilter.deriv.DAOD_HIGG3D1.e5421_s3126_r9364_p4164
mc16_13TeV.364212.Sherpa_221_NN30NNLO_Ztt_M110_40_MAXHTPTV70_280_BVeto.deriv.DAOD_HIGG3D1.e5421_s3126_r9364_p4164
```

```
mc16_13TeV.364213.Sherpa_221_NN3ONNLO_Ztt_Ml110_40_MAXHTPTV70_280_BFilter.deriv.DAOD_HIGG3D1.e5421_s3126_r9364_p4164
mc16_13TeV.364214.Sherpa_221_NN3ONNLO_Ztt_Ml110_40_MAXHTPTV280_E_CMS_BVeto.deriv.DAOD_HIGG3D1.e5421_s3126_r9364_p4164
mc16_13TeV.364215.Sherpa_221_NN3ONNLO_Ztt_Ml110_40_MAXHTPTV280_E_CMS_BFilter.deriv.DAOD_HIGG3D1.e5421_s3126_r9364_p4164
mc16_13TeV.364282.Sherpa_221_NNPDF30NNLO_Ztautau_Ml12M1_MAXHTPTV280_E_CMS.deriv.DAOD_HIGG3D1.e6037_s3126_r9364_p4164
mc16_13TeV.364360.Sherpa_221_NNPDF30NNLO_Ztautau_Ml12M1_MAXHTPTV70_140.deriv.DAOD_HIGG3D1.e6544_a875_r9364_p4164
mc16_13TeV.364363.Sherpa_221_NNPDF30NNLO_Ztautau_Ml12M1_MAXHTPTV140_280.deriv.DAOD_HIGG3D1.e6544_a875_r9364_p4164
```

Diboson

```
mc16_13TeV.363355.Sherpa_221_NNPDF30NNLO_ZqqZvv.deriv.DAOD_HIGG3D1.e5525_s3126_r9364_p4164
mc16_13TeV.363356.Sherpa_221_NNPDF30NNLO_ZqqZll.deriv.DAOD_HIGG3D1.e5525_s3126_r9364_p4164
mc16_13TeV.363357.Sherpa_221_NNPDF30NNLO_WqqZvv.deriv.DAOD_HIGG3D1.e5525_s3126_r9364_p4164
mc16_13TeV.363358.Sherpa_221_NNPDF30NNLO_WqqZll.deriv.DAOD_HIGG3D1.e5525_s3126_r9364_p4164
mc16_13TeV.363359.Sherpa_221_NNPDF30NNLO_WpqqWmlv.deriv.DAOD_HIGG3D1.e5583_s3126_r9364_p4164
mc16_13TeV.363360.Sherpa_221_NNPDF30NNLO_WplvWmqq.deriv.DAOD_HIGG3D1.e5983_s3126_r9364_p4164
mc16_13TeV.363489.Sherpa_221_NNPDF30NNLO_WlvZqq.deriv.DAOD_HIGG3D1.e5525_s3126_r9364_p4164
mc16_13TeV.364250.Sherpa_222_NNPDF30NNLO_llll.deriv.DAOD_HIGG3D1.e5894_s3126_r9364_p4164
mc16_13TeV.364253.Sherpa_222_NNPDF30NNLO_lllv.deriv.DAOD_HIGG3D1.e5916_s3126_r9364_p4164
mc16_13TeV.364254.Sherpa_222_NNPDF30NNLO_llvv.deriv.DAOD_HIGG3D1.e5916_s3126_r9364_p4166
mc16_13TeV.364255.Sherpa_222_NNPDF30NNLO_lvvv.deriv.DAOD_HIGG3D1.e5916_s3126_r9364_p4164
mc16_13TeV.364286.Sherpa_222_NNPDF30NNLO_llvvjj_ss_EW4.deriv.DAOD_HIGG3D1.e6055_s3126_r9364_p4164
mc16_13TeV.364288.Sherpa_222_NNPDF30NNLO_llll_lowMllPtComplement.deriv.DAOD_HIGG3D1.e6096_s3126_r9364_p4164
mc16_13TeV.364289.Sherpa_222_NNPDF30NNLO_lllv_lowMllPtComplement.deriv.DAOD_HIGG3D1.e6133_s3126_r9364_p4164
mc16_13TeV.364290.Sherpa_222_NNPDF30NNLO_llvv_lowMllPtComplement.deriv.DAOD_HIGG3D1.e6096_s3126_r9364_p4164
```

$W \to l\nu$+jets

```
mc16_13TeV.364156.Sherpa_221_NNPDF30NNLO_Wmunu_MAXHTPTV0_70_CVetoBVeto.deriv.DAOD_HIGG3D1.e5340_s3126_r9364_p4164
mc16_13TeV.364157.Sherpa_221_NNPDF30NNLO_Wmunu_MAXHTPTV0_70_CFilterBVeto.deriv.DAOD_HIGG3D1.e5340_s3126_r9364_p4164
mc16_13TeV.364158.Sherpa_221_NNPDF30NNLO_Wmunu_MAXHTPTV0_70_BFilter.deriv.DAOD_HIGG3D1.e5340_s3126_r9364_p4164
mc16_13TeV.364159.Sherpa_221_NNPDF30NNLO_Wmunu_MAXHTPTV70_140_CVetoBVeto.deriv.DAOD_HIGG3D1.e5340_s3126_r9364_p4164
```

mc16_13TeV.364160.Sherpa_221_NNPDF30NNLO_Wmunu_MAXHTPTV70_140_CFilterBVeto.deriv.DAOD_HIGG3D1.e5340_s3126_r9364_p4164
mc16_13TeV.364161.Sherpa_221_NNPDF30NNLO_Wmunu_MAXHTPTV70_140_BFilter.deriv.DAOD_HIGG3D1.e5340_s3126_r9364_p4164
mc16_13TeV.364162.Sherpa_221_NNPDF30NNLO_Wmunu_MAXHTPTV140_280_CVetoBVeto.deriv.DAOD_HIGG3D1.e5340_s3126_r9364_p4164
mc16_13TeV.364163.Sherpa_221_NNPDF30NNLO_Wmunu_MAXHTPTV140_280_CFilterBVeto.deriv.DAOD_HIGG3D1.e5340_s3126_r9364_p4164
mc16_13TeV.364164.Sherpa_221_NNPDF30NNLO_Wmunu_MAXHTPTV140_280_BFilter.deriv.DAOD_HIGG3D1.e5340_s3126_r9364_p4164
mc16_13TeV.364165.Sherpa_221_NNPDF30NNLO_Wmunu_MAXHTPTV280_500_CVetoBVeto.deriv.DAOD_HIGG3D1.e5340_s3126_r9364_p4164
mc16_13TeV.364166.Sherpa_221_NNPDF30NNLO_Wmunu_MAXHTPTV280_500_CFilterBVeto.deriv.DAOD_HIGG3D1.e5340_s3126_r9364_p4164
mc16_13TeV.364167.Sherpa_221_NNPDF30NNLO_Wmunu_MAXHTPTV280_500_BFilter.deriv.DAOD_HIGG3D1.e5340_s3126_r9364_p4164
mc16_13TeV.364168.Sherpa_221_NNPDF30NNLO_Wmunu_MAXHTPTV500_1000.deriv.DAOD_HIGG3D1.e5340_s3126_r9364_p4164
mc16_13TeV.364169.Sherpa_221_NNPDF30NNLO_Wmunu_MAXHTPTV1000_E_CMS.deriv.DAOD_HIGG3D1.e5340_s3126_r9364_p4164
mc16_13TeV.364170.Sherpa_221_NNPDF30NNLO_Wenu_MAXHTPTV0_70_CVetoBVeto.deriv.DAOD_HIGG3D1.e5340_s3126_r9364_p4164
mc16_13TeV.364171.Sherpa_221_NNPDF30NNLO_Wenu_MAXHTPTV0_70_CFilterBVeto.deriv.DAOD_HIGG3D1.e5340_s3126_r9364_p4164
mc16_13TeV.364172.Sherpa_221_NNPDF30NNLO_Wenu_MAXHTPTV0_70_BFilter.deriv.DAOD_HIGG3D1.e5340_s3126_r9364_p4164
mc16_13TeV.364173.Sherpa_221_NNPDF30NNLO_Wenu_MAXHTPTV70_140_CVetoBVeto.deriv.DAOD_HIGG3D1.e5340_s3126_r9364_p4164
mc16_13TeV.364174.Sherpa_221_NNPDF30NNLO_Wenu_MAXHTPTV70_140_CFilterBVeto.deriv.DAOD_HIGG3D1.e5340_s3126_r9364_p4164
mc16_13TeV.364175.Sherpa_221_NNPDF30NNLO_Wenu_MAXHTPTV70_140_BFilter.deriv.DAOD_HIGG3D1.e5340_s3126_r9364_p4164
mc16_13TeV.364176.Sherpa_221_NNPDF30NNLO_Wenu_MAXHTPTV140_280_CVetoBVeto.deriv.DAOD_HIGG3D1.e5340_s3126_r9364_p4164
mc16_13TeV.364177.Sherpa_221_NNPDF30NNLO_Wenu_MAXHTPTV140_280_CFilterBVeto.deriv.DAOD_HIGG3D1.e5340_s3126_r9364_p4164
mc16_13TeV.364178.Sherpa_221_NNPDF30NNLO_Wenu_MAXHTPTV140_280_BFilter.deriv.DAOD_HIGG3D1.e5340_s3126_r9364_p4164
mc16_13TeV.364179.Sherpa_221_NNPDF30NNLO_Wenu_MAXHTPTV280_500_CVetoBVeto.deriv.DAOD_HIGG3D1.e5340_s3126_r9364_p4164
mc16_13TeV.364180.Sherpa_221_NNPDF30NNLO_Wenu_MAXHTPTV280_500_CFilterBVeto.deriv.DAOD_HIGG3D1.e5340_s3126_r9364_p4164
mc16_13TeV.364181.Sherpa_221_NNPDF30NNLO_Wenu_MAXHTPTV280_500_BFilter.deriv.DAOD_HIGG3D1.e5340_s3126_r9364_p4164
mc16_13TeV.364182.Sherpa_221_NNPDF30NNLO_Wenu_MAXHTPTV500_1000.deriv.DAOD_HIGG3D1.e5340_s3126_r9364_p4164
mc16_13TeV.364183.Sherpa_221_NNPDF30NNLO_Wenu_MAXHTPTV1000_E_CMS.deriv.DAOD_HIGG3D1.e5340_s3126_r9364_p4164
mc16_13TeV.364184.Sherpa_221_NNPDF30NNLO_Wtaunu_MAXHTPTV0_70_CVetoBVeto.deriv.DAOD_HIGG3D1.e5340_s3126_r9364_p4164
mc16_13TeV.364185.Sherpa_221_NNPDF30NNLO_Wtaunu_MAXHTPTV0_70_CFilterBVeto.deriv.DAOD_HIGG3D1.e5340_s3126_r9364_p4164
mc16_13TeV.364186.Sherpa_221_NNPDF30NNLO_Wtaunu_MAXHTPTV0_70_BFilter.deriv.DAOD_HIGG3D1.e5340_s3126_r9364_p4164
mc16_13TeV.364187.Sherpa_221_NNPDF30NNLO_Wtaunu_MAXHTPTV70_140_CVetoBVeto.deriv.DAOD_HIGG3D1.e5340_s3126_r9364_p4164
mc16_13TeV.364188.Sherpa_221_NNPDF30NNLO_Wtaunu_MAXHTPTV70_140_CFilterBVeto.deriv.DAOD_HIGG3D1.e5340_s3126_r9364_p4164

mc16_13TeV.364189.Sherpa_221_NNPDF30NNLO_Wtaunu_MAXHTPTV70_140_BFilter.deriv.DAOD_HIGG3D1.e5340_s3126_r9364_p4164

mc16_13TeV.364190.Sherpa_221_NNPDF30NNLO_Wtaunu_MAXHTPTV140_280_CVetoBVeto.deriv.DAOD_HIGG3D1.e5340_s3126_r9364_p4164

mc16_13TeV.364191.Sherpa_221_NNPDF30NNLO_Wtaunu_MAXHTPTV140_280_CFilterBVeto.deriv.DAOD_HIGG3D1.e5340_s3126_r9364_p4164

mc16_13TeV.364192.Sherpa_221_NNPDF30NNLO_Wtaunu_MAXHTPTV140_280_BFilter.deriv.DAOD_HIGG3D1.e5340_s3126_r9364_p4164

mc16_13TeV.364193.Sherpa_221_NNPDF30NNLO_Wtaunu_MAXHTPTV280_500_CVetoBVeto.deriv.DAOD_HIGG3D1.e5340_s3126_r9364_p4164

mc16_13TeV.364194.Sherpa_221_NNPDF30NNLO_Wtaunu_MAXHTPTV280_500_CFilterBVeto.deriv.DAOD_HIGG3D1.e5340_s3126_r9364_p4164

mc16_13TeV.364195.Sherpa_221_NNPDF30NNLO_Wtaunu_MAXHTPTV280_500_BFilter.deriv.DAOD_HIGG3D1.e5340_s3126_r9364_p4164

mc16_13TeV.364196.Sherpa_221_NNPDF30NNLO_Wtaunu_MAXHTPTV500_1000.deriv.DAOD_HIGG3D1.e5340_s3126_r9364_p4164

mc16_13TeV.364197.Sherpa_221_NNPDF30NNLO_Wtaunu_MAXHTPTV1000_E_CMS.deriv.DAOD_HIGG3D1.e5340_s3126_r9364_p4164

$Z/\gamma* \rightarrow \mu\mu$+jets

mc16_13TeV.364100.Sherpa_221_NNPDF30NNLO_Zmumu_MAXHTPTV0_70_CVetoBVeto.deriv.DAOD_HIGG3D1.e5271_s3126_r9364_p4164

mc16_13TeV.364101.Sherpa_221_NNPDF30NNLO_Zmumu_MAXHTPTV0_70_CFilterBVeto.deriv.DAOD_HIGG3D1.e5271_s3126_r9364_p4164

mc16_13TeV.364102.Sherpa_221_NNPDF30NNLO_Zmumu_MAXHTPTV0_70_BFilter.deriv.DAOD_HIGG3D1.e5271_s3126_r9364_p4164

mc16_13TeV.364103.Sherpa_221_NNPDF30NNLO_Zmumu_MAXHTPTV70_140_CVetoBVeto.deriv.DAOD_HIGG3D1.e5271_s3126_r9364_p4164

mc16_13TeV.364104.Sherpa_221_NNPDF30NNLO_Zmumu_MAXHTPTV70_140_CFilterBVeto.deriv.DAOD_HIGG3D1.e5271_s3126_r9364_p4164

mc16_13TeV.364105.Sherpa_221_NNPDF30NNLO_Zmumu_MAXHTPTV70_140_BFilter.deriv.DAOD_HIGG3D1.e5271_s3126_r9364_p4164

mc16_13TeV.364106.Sherpa_221_NNPDF30NNLO_Zmumu_MAXHTPTV140_280_CVetoBVeto.deriv.DAOD_HIGG3D1.e5271_s3126_r9364_p4164

mc16_13TeV.364107.Sherpa_221_NNPDF30NNLO_Zmumu_MAXHTPTV140_280_CFilterBVeto.deriv.DAOD_HIGG3D1.e5271_s3126_r9364_p4164

mc16_13TeV.364108.Sherpa_221_NNPDF30NNLO_Zmumu_MAXHTPTV140_280_BFilter.deriv.DAOD_HIGG3D1.e5271_s3126_r9364_p4164

mc16_13TeV.364109.Sherpa_221_NNPDF30NNLO_Zmumu_MAXHTPTV280_500_CVetoBVeto.deriv.DAOD_HIGG3D1.e5271_s3126_r9364_p4164

mc16_13TeV.364110.Sherpa_221_NNPDF30NNLO_Zmumu_MAXHTPTV280_500_CFilterBVeto.deriv.DAOD_HIGG3D1.e5271_s3126_r9364_p4164

mc16_13TeV.364111.Sherpa_221_NNPDF30NNLO_Zmumu_MAXHTPTV280_500_BFilter.deriv.DAOD_HIGG3D1.e5271_s3126_r9364_p4164

mc16_13TeV.364112.Sherpa_221_NNPDF30NNLO_Zmumu_MAXHTPTV500_1000.deriv.DAOD_HIGG3D1.e5271_s3126_r9364_p4164

mc16_13TeV.364113.Sherpa_221_NNPDF30NNLO_Zmumu_MAXHTPTV1000_E_CMS.deriv.DAOD_HIGG3D1.e5271_s3126_r9364_p4164

mc16_13TeV.364198.Sherpa_221_NN30NNLO_Zmm_M110_40_MAXHTPTV0_70_BVeto.deriv.DAOD_HIGG3D1.e5421_s3126_r9364_p4164

mc16_13TeV.364199.Sherpa_221_NN30NNLO_Zmm_M110_40_MAXHTPTV0_70_BFilter.deriv.DAOD_HIGG3D1.e5421_s3126_r9364_p4164

mc16_13TeV.364200.Sherpa_221_NN30NNLO_Zmm_M110_40_MAXHTPTV70_280_BVeto.deriv.DAOD_HIGG3D1.e5421_s3126_r9364_p4164

mc16_13TeV.364201.Sherpa_221_NN30NNLO_Zmm_M110_40_MAXHTPTV70_280_BFilter.deriv.DAOD_HIGG3D1.e5421_s3126_r9364_p4164

mc16_13TeV.364202.Sherpa_221_NN30NNL0_Zmm_M110_40_MAXHTPTV280_E_CMS_BVeto.deriv.DAOD_HIGG3D1.e5421_s3126_r9364_p4164
mc16_13TeV.364203.Sherpa_221_NN30NNL0_Zmm_M110_40_MAXHTPTV280_E_CMS_BFilter.deriv.DAOD_HIGG3D1.e5421_s3126_r9364_p4164
mc16_13TeV.364204.Sherpa_221_NN30NNL0_Zmm_M110_40_MAXHTPTV0_70_BVeto.deriv.DAOD_HIGG3D1.e5421_s3126_r9364_p4164
mc16_13TeV.364205.Sherpa_221_NN30NNL0_Zee_M110_40_MAXHTPTV0_70_BFilter.deriv.DAOD_HIGG3D1.e5421_s3126_r9364_p4164
mc16_13TeV.364206.Sherpa_221_NN30NNL0_Zee_M110_40_MAXHTPTV70_280_BVeto.deriv.DAOD_HIGG3D1.e5421_s3126_r9364_p4164
mc16_13TeV.364207.Sherpa_221_NN30NNL0_Zee_M110_40_MAXHTPTV70_280_BFilter.deriv.DAOD_HIGG3D1.e5421_s3126_r9364_p4164
mc16_13TeV.364208.Sherpa_221_NN30NNL0_Zee_M110_40_MAXHTPTV280_E_CMS_BVeto.deriv.DAOD_HIGG3D1.e5421_s3126_r9364_p4164
mc16_13TeV.364209.Sherpa_221_NN30NNL0_Zee_M110_40_MAXHTPTV280_E_CMS_BFilter.deriv.DAOD_HIGG3D1.e5421_s3126_r9364_p4164
mc16_13TeV.364281.Sherpa_221_NNPDF30NNL0_Zmumu_M112M1_MAXHTPTV280_E_CMS.deriv.DAOD_HIGG3D1.e6037_s3126_r9364_p4164
mc16_13TeV.364359.Sherpa_221_NNPDF30NNL0_Zmumu_M112M1_MAXHTPTV70_140.deriv.DAOD_HIGG3D1.e6544_a875_r9364_p4164
mc16_13TeV.364362.Sherpa_221_NNPDF30NNL0_Zmumu_M112M1_MAXHTPTV140_280.deriv.DAOD_HIGG3D1.e6544_a875_r9364_p4164

$Z/\gamma* \to ee$+jets

mc16_13TeV.364114.Sherpa_221_NNPDF30NNL0_Zee_MAXHTPTV0_70_CVetoBVeto.deriv.DAOD_HIGG3D1.e5299_s3126_r9364_p4164
mc16_13TeV.364115.Sherpa_221_NNPDF30NNL0_Zee_MAXHTPTV0_70_CFilterBVeto.deriv.DAOD_HIGG3D1.e5299_s3126_r9364_p4164
mc16_13TeV.364116.Sherpa_221_NNPDF30NNL0_Zee_MAXHTPTV0_70_BFilter.deriv.DAOD_HIGG3D1.e5299_s3126_r9364_p4164
mc16_13TeV.364117.Sherpa_221_NNPDF30NNL0_Zee_MAXHTPTV70_140_CVetoBVeto.deriv.DAOD_HIGG3D1.e5299_s3126_r9364_p4164
mc16_13TeV.364118.Sherpa_221_NNPDF30NNL0_Zee_MAXHTPTV70_140_CFilterBVeto.deriv.DAOD_HIGG3D1.e5299_s3126_r9364_p4164
mc16_13TeV.364119.Sherpa_221_NNPDF30NNL0_Zee_MAXHTPTV70_140_BFilter.deriv.DAOD_HIGG3D1.e5299_s3126_r9364_p4164
mc16_13TeV.364120.Sherpa_221_NNPDF30NNL0_Zee_MAXHTPTV140_280_CVetoBVeto.deriv.DAOD_HIGG3D1.e5299_s3126_r9364_p4164
mc16_13TeV.364121.Sherpa_221_NNPDF30NNL0_Zee_MAXHTPTV140_280_CFilterBVeto.deriv.DAOD_HIGG3D1.e5299_s3126_r9364_p4164
mc16_13TeV.364122.Sherpa_221_NNPDF30NNL0_Zee_MAXHTPTV140_280_BFilter.deriv.DAOD_HIGG3D1.e5299_s3126_r9364_p4164
mc16_13TeV.364123.Sherpa_221_NNPDF30NNL0_Zee_MAXHTPTV280_500_CVetoBVeto.deriv.DAOD_HIGG3D1.e5299_s3126_r9364_p4164
mc16_13TeV.364124.Sherpa_221_NNPDF30NNL0_Zee_MAXHTPTV280_500_CFilterBVeto.deriv.DAOD_HIGG3D1.e5299_s3126_r9364_p4164
mc16_13TeV.364125.Sherpa_221_NNPDF30NNL0_Zee_MAXHTPTV280_500_BFilter.deriv.DAOD_HIGG3D1.e5299_s3126_r9364_p4164
mc16_13TeV.364126.Sherpa_221_NNPDF30NNL0_Zee_MAXHTPTV500_1000.deriv.DAOD_HIGG3D1.e5299_s3126_r9364_p4164
mc16_13TeV.364127.Sherpa_221_NNPDF30NNL0_Zee_MAXHTPTV1000_E_CMS.deriv.DAOD_HIGG3D1.e5299_s3126_r9364_p4164
mc16_13TeV.364280.Sherpa_221_NNPDF30NNL0_Zee_M112M1_MAXHTPTV280_E_CMS.deriv.DAOD_HIGG3D1.e6037_s3126_r9364_p4164
mc16_13TeV.364358.Sherpa_221_NNPDF30NNL0_Zee_M112M1_MAXHTPTV70_140.deriv.DAOD_HIGG3D1.e6544_a875_r9364_p4164

mc16_13TeV.364361.Sherpa_221_NNPDF30NNLO_Zee_M112M1_MAXHTPTV140_280.deriv.DAOD_HIGG3D1.e6544_a875_r9364_p4164

$t\bar{t}$, single top

mc16_13TeV.410470.PhPy8EG_A14_ttbar_hdamp258p75_nonallhad.deriv.DAOD_HIGG3D1.e6337_s3126_r9364_p4164
mc16_13TeV.410644.PowhegPythia8EvtGen_A14_singletop_schan_lept_top.deriv.DAOD_HIGG3D1.e6527_s3126_r9364_p4164
mc16_13TeV.410645.PowhegPythia8EvtGen_A14_singletop_schan_lept_antitop.deriv.DAOD_HIGG3D1.e6527_s3126_r9364_p4164
mc16_13TeV.410648.PowhegPythia8EvtGen_A14_Wt_DR_dilepton_top.deriv.DAOD_HIGG3D1.e6615_s3126_r9364_p4164
mc16_13TeV.410649.PowhegPythia8EvtGen_A14_Wt_DR_dilepton_antitop.deriv.DAOD_HIGG3D1.e6615_s3126_r9364_p4164
mc16_13TeV.410658.PhPy8EG_A14_tchan_BW50_lept_top.deriv.DAOD_HIGG3D1.e6671_s3126_r9364_p4164
mc16_13TeV.410659.PhPy8EG_A14_tchan_BW50_lept_antitop.deriv.DAOD_HIGG3D1.e6671_s3126_r9364_p4164

SM Higgs

mc16_13TeV.345120.PowhegPy8EG_NNLOPS_nnlo_30_ggH125_tautaul1317.deriv.DAOD_HIGG3D1.e5814_s3126_r9364_p4164
mc16_13TeV.345121.PowhegPy8EG_NNLOPS_nnlo_30_ggH125_tautaulm15hp20.deriv.DAOD_HIGG3D1.e5814_s3126_r9364_p4164
mc16_13TeV.345122.PowhegPy8EG_NNLOPS_nnlo_30_ggH125_tautaulp15hm20.deriv.DAOD_HIGG3D1.e5814_s3126_r9364_p4164
mc16_13TeV.345123.PowhegPy8EG_NNLOPS_nnlo_30_ggH125_tautauh30h20.deriv.DAOD_HIGG3D1.e5814_s3126_r9364_p4164
mc16_13TeV.345211.PowhegPy8EG_NNPDF30_AZNLO_WmH125J_Winc_MINLO_tautau.deriv.DAOD_HIGG3D1.e5808_s3126_r9364_p4164
mc16_13TeV.345212.PowhegPy8EG_NNPDF30_AZNLO_WpH125J_Winc_MINLO_tautau.deriv.DAOD_HIGG3D1.e5808_s3126_r9364_p4164
mc16_13TeV.345217.PowhegPy8EG_NNPDF30_AZNLO_ZH125J_Zinc_MINLO_tautau.deriv.DAOD_HIGG3D1.e5808_s3126_r9364_p4164
mc16_13TeV.345324.PowhegPythia8EvtGen_NNLOPS_NN30_ggH125_WW1v1v_EF_15_5.deriv.DAOD_HIGG3D1.e5769_s3126_r9364_p4166
mc16_13TeV.345948.PowhegPy8EG_NNPDF30_AZNLOCTEQ6L1_VBFH125_WW1v1v.deriv.DAOD_HIGG3D1.e7172_s3126_r9364_p4166
mc16_13TeV.346190.PowhegPy8EG_NNPDF30_AZNLOCTEQ6L1_VBFH125_tautaul1317.deriv.DAOD_HIGG3D1.e7259_s3126_r9364_p4164

A.2. mc16d

gluon-fusion A production

mc16_13TeV.346025.Pythia8EvtGen_A14NNPDF23LO_ggA60_tautau_leplep.deriv.DAOD_HIGG3D1.e7122_a875_r10201_p4164
mc16_13TeV.346026.Pythia8EvtGen_A14NNPDF23LO_ggA70_tautau_leplep.deriv.DAOD_HIGG3D1.e7122_a875_r10201_p4164

```
mc16_13TeV.346027.Pythia8EvtGen_A14NNPDF23LO_ggA80_tautau_leplep.deriv.DAOD_HIGG3D1.e7122_a875_r10201_p4164
mc16_13TeV.346028.Pythia8EvtGen_A14NNPDF23LO_ggA90_tautau_leplep.deriv.DAOD_HIGG3D1.e7122_a875_r10201_p4164
mc16_13TeV.346375.Pythia8EvtGen_A14NNPDF23LO_ggA50_tautau_leplep.deriv.DAOD_HIGG3D1.e7122_a875_r10201_p4164
mc16_13TeV.451705.Pythia8EvtGen_A14NNPDF23LO_ggA40_tautau_leplep.deriv.DAOD_HIGG3D1.e8139_a875_r10201_p4164
mc16_13TeV.801162.Py8EG_A14NNPDF23LO_ggA20_tautau_11314.deriv.DAOD_HIGG3D1.e8307_a875_r10201_p4164
mc16_13TeV.801163.Py8EG_A14NNPDF23LO_ggA30_tautau_11314.deriv.DAOD_HIGG3D1.e8307_a875_r10201_p4164
mc16_13TeV.801827.Py8EG_A14NNPDF23LO_ggA100_tautau_11314.deriv.DAOD_HIGG3D1.e8307_a875_r10201_p4164
mc16_13TeV.801828.Py8EG_A14NNPDF23LO_ggA110_tautau_11314.deriv.DAOD_HIGG3D1.e8307_a875_r10201_p4164
```

$Z/\gamma* \rightarrow \tau\tau$+jets

```
mc16_13TeV.364128.Sherpa_221_NNPDF30NNLO_Ztautau_MAXHTPTV0_70_CVetoBVeto.deriv.DAOD_HIGG3D1.e5307_s3126_r10201_p4164
mc16_13TeV.364129.Sherpa_221_NNPDF30NNLO_Ztautau_MAXHTPTV0_70_CFilterBVeto.deriv.DAOD_HIGG3D1.e5307_s3126_r10201_p4164
mc16_13TeV.364130.Sherpa_221_NNPDF30NNLO_Ztautau_MAXHTPTV0_70_BFilter.deriv.DAOD_HIGG3D1.e5307_s3126_r10201_p4164
mc16_13TeV.364131.Sherpa_221_NNPDF30NNLO_Ztautau_MAXHTPTV70_140_CVetoBVeto.deriv.DAOD_HIGG3D1.e5307_s3126_r10201_p4164
mc16_13TeV.364132.Sherpa_221_NNPDF30NNLO_Ztautau_MAXHTPTV70_140_CFilterBVeto.deriv.DAOD_HIGG3D1.e5307_s3126_r10201_p4164
mc16_13TeV.364133.Sherpa_221_NNPDF30NNLO_Ztautau_MAXHTPTV70_140_BFilter.deriv.DAOD_HIGG3D1.e5307_s3126_r10201_p4164
mc16_13TeV.364134.Sherpa_221_NNPDF30NNLO_Ztautau_MAXHTPTV140_280_CVetoBVeto.deriv.DAOD_HIGG3D1.e5307_s3126_r10201_p4164
mc16_13TeV.364135.Sherpa_221_NNPDF30NNLO_Ztautau_MAXHTPTV140_280_CFilterBVeto.deriv.DAOD_HIGG3D1.e5307_s3126_r10201_p4164
mc16_13TeV.364136.Sherpa_221_NNPDF30NNLO_Ztautau_MAXHTPTV140_280_BFilter.deriv.DAOD_HIGG3D1.e5307_s3126_r10201_p4164
mc16_13TeV.364137.Sherpa_221_NNPDF30NNLO_Ztautau_MAXHTPTV280_500_CVetoBVeto.deriv.DAOD_HIGG3D1.e5307_s3126_r10201_p4164
mc16_13TeV.364138.Sherpa_221_NNPDF30NNLO_Ztautau_MAXHTPTV280_500_CFilterBVeto.deriv.DAOD_HIGG3D1.e5313_s3126_r10201_p4164
mc16_13TeV.364139.Sherpa_221_NNPDF30NNLO_Ztautau_MAXHTPTV280_500_BFilter.deriv.DAOD_HIGG3D1.e5313_s3126_r10201_p4164
mc16_13TeV.364140.Sherpa_221_NNPDF30NNLO_Ztautau_MAXHTPTV500_1000.deriv.DAOD_HIGG3D1.e5307_s3126_r10201_p4164
mc16_13TeV.364141.Sherpa_221_NNPDF30NNLO_Ztautau_MAXHTPTV1000_E_CMS.deriv.DAOD_HIGG3D1.e5307_s3126_r10201_p4164
mc16_13TeV.364210.Sherpa_221_NN30NNLO_Ztt_M110_40_MAXHTPTV0_70_BVeto.deriv.DAOD_HIGG3D1.e5421_s3126_r10201_p4164
mc16_13TeV.364211.Sherpa_221_NN30NNLO_Ztt_M110_40_MAXHTPTV0_70_BFilter.deriv.DAOD_HIGG3D1.e5421_s3126_r10201_p4164
mc16_13TeV.364212.Sherpa_221_NN30NNLO_Ztt_M110_40_MAXHTPTV70_280_CVetoBVeto.deriv.DAOD_HIGG3D1.e5421_s3126_r10201_p4164
mc16_13TeV.364213.Sherpa_221_NN30NNLO_Ztt_M110_40_MAXHTPTV70_280_BVeto.deriv.DAOD_HIGG3D1.e5421_s3126_r10201_p4164
mc16_13TeV.364214.Sherpa_221_NN30NNLO_Ztt_M110_40_MAXHTPTV280_E_CMS_BVeto.deriv.DAOD_HIGG3D1.e5421_s3126_r10201_p4164
```

```
mc16_13TeV.364215.Sherpa_221_NN3ONNLO_Ztt_M110_40_MAXHTPTV280_E_CMS_BFilter.deriv.DAOD_HIGG3D1.e5421_s3126_r10201_p4164
mc16_13TeV.364282.Sherpa_221_NNPDF30NNLO_Ztautau_Ml12M1_MAXHTPTV280_E_CMS.deriv.DAOD_HIGG3D1.e6037_s3126_r10201_p4164
mc16_13TeV.364360.Sherpa_221_NNPDF30NNLO_Ztautau_Ml12M1_MAXHTPTV70_140.deriv.DAOD_HIGG3D1.e6544_a875_r10201_p4164
mc16_13TeV.364363.Sherpa_221_NNPDF30NNLO_Ztautau_Ml12M1_MAXHTPTV140_280.deriv.DAOD_HIGG3D1.e6544_a875_r10201_p4164
```

Diboson

```
mc16_13TeV.363355.Sherpa_221_NNPDF30NNLO_ZqqZvv.deriv.DAOD_HIGG3D1.e5525_s3126_r10201_p4164
mc16_13TeV.363356.Sherpa_221_NNPDF30NNLO_ZqqZll.deriv.DAOD_HIGG3D1.e5525_s3126_r10201_p4164
mc16_13TeV.363357.Sherpa_221_NNPDF30NNLO_WqqZvv.deriv.DAOD_HIGG3D1.e5525_s3126_r10201_p4164
mc16_13TeV.363358.Sherpa_221_NNPDF30NNLO_WqqZll.deriv.DAOD_HIGG3D1.e5525_s3126_r10201_p4164
mc16_13TeV.363359.Sherpa_221_NNPDF30NNLO_WpqqWmlv.deriv.DAOD_HIGG3D1.e5583_s3126_r10201_p4164
mc16_13TeV.363360.Sherpa_221_NNPDF30NNLO_WplvWmqq.deriv.DAOD_HIGG3D1.e5983_s3126_r10201_p4164
mc16_13TeV.363489.Sherpa_221_NNPDF30NNLO_WlvZqq.deriv.DAOD_HIGG3D1.e5525_s3126_r10201_p4164
mc16_13TeV.364250.Sherpa_222_NNPDF30NNLO_llll.deriv.DAOD_HIGG3D1.e5894_s3126_r10201_p4164
mc16_13TeV.364253.Sherpa_222_NNPDF30NNLO_lllv.deriv.DAOD_HIGG3D1.e5916_s3126_r10201_p4164
mc16_13TeV.364254.Sherpa_222_NNPDF30NNLO_llvv.deriv.DAOD_HIGG3D1.e5916_s3126_r10201_p4166
mc16_13TeV.364255.Sherpa_222_NNPDF30NNLO_lvvv.deriv.DAOD_HIGG3D1.e5916_s3126_r10201_p4164
mc16_13TeV.364286.Sherpa_222_NNPDF30NNLO_llvvjj_ss_EW4.deriv.DAOD_HIGG3D1.e6055_s3126_r10201_p4164
mc16_13TeV.364288.Sherpa_222_NNPDF30NNLO_llll_lowM1lPtComplement.deriv.DAOD_HIGG3D1.e6096_s3126_r10201_p4164
mc16_13TeV.364289.Sherpa_222_NNPDF30NNLO_lllv_lowM1lPtComplement.deriv.DAOD_HIGG3D1.e6133_s3126_r10201_p4164
mc16_13TeV.364290.Sherpa_222_NNPDF30NNLO_llvv_lowM1lPtComplement.deriv.DAOD_HIGG3D1.e6096_s3126_r10201_p4164
```

$W \to l\nu$+jets

```
mc16_13TeV.364156.Sherpa_221_NNPDF30NNLO_Wmunu_MAXHTPTV0_70_CVetoBVeto.deriv.DAOD_HIGG3D1.e5340_s3126_r10201_p4164
mc16_13TeV.364157.Sherpa_221_NNPDF30NNLO_Wmunu_MAXHTPTV0_70_CFilterBVeto.deriv.DAOD_HIGG3D1.e5340_s3126_r10201_p4164
mc16_13TeV.364158.Sherpa_221_NNPDF30NNLO_Wmunu_MAXHTPTV0_70_BFilter.deriv.DAOD_HIGG3D1.e5340_s3126_r10201_p4164
mc16_13TeV.364159.Sherpa_221_NNPDF30NNLO_Wmunu_MAXHTPTV70_140_CVetoBVeto.deriv.DAOD_HIGG3D1.e5340_s3126_r10201_p4164
mc16_13TeV.364160.Sherpa_221_NNPDF30NNLO_Wmunu_MAXHTPTV70_140_CFilterBVeto.deriv.DAOD_HIGG3D1.e5340_s3126_r10201_p4164
mc16_13TeV.364161.Sherpa_221_NNPDF30NNLO_Wmunu_MAXHTPTV70_140_BFilter.deriv.DAOD_HIGG3D1.e5340_s3126_r10201_p4164
```

```
mc16_13TeV.364162.Sherpa_221_NNPDF30NNLO_Wmunu_MAXHTPTV140_280_CVetoBVeto.deriv.DAOD_HIGG3D1.e5340_s3126_r10201_p4164
mc16_13TeV.364163.Sherpa_221_NNPDF30NNLO_Wmunu_MAXHTPTV140_280_CFilterBVeto.deriv.DAOD_HIGG3D1.e5340_s3126_r10201_p4164
mc16_13TeV.364164.Sherpa_221_NNPDF30NNLO_Wmunu_MAXHTPTV140_280_BFilter.deriv.DAOD_HIGG3D1.e5340_s3126_r10201_p4164
mc16_13TeV.364165.Sherpa_221_NNPDF30NNLO_Wmunu_MAXHTPTV280_500_CVetoBVeto.deriv.DAOD_HIGG3D1.e5340_s3126_r10201_p4164
mc16_13TeV.364166.Sherpa_221_NNPDF30NNLO_Wmunu_MAXHTPTV280_500_CFilterBVeto.deriv.DAOD_HIGG3D1.e5340_s3126_r10201_p4164
mc16_13TeV.364167.Sherpa_221_NNPDF30NNLO_Wmunu_MAXHTPTV280_500_BFilter.deriv.DAOD_HIGG3D1.e5340_s3126_r10201_p4164
mc16_13TeV.364168.Sherpa_221_NNPDF30NNLO_Wmunu_MAXHTPTV500_1000.deriv.DAOD_HIGG3D1.e5340_s3126_r10201_p4164
mc16_13TeV.364169.Sherpa_221_NNPDF30NNLO_Wmunu_MAXHTPTV1000_E_CMS.deriv.DAOD_HIGG3D1.e5340_s3126_r10201_p4164
mc16_13TeV.364170.Sherpa_221_NNPDF30NNLO_Wenu_MAXHTPTV0_70_CVetoBVeto.deriv.DAOD_HIGG3D1.e5340_s3126_r10201_p4164
mc16_13TeV.364171.Sherpa_221_NNPDF30NNLO_Wenu_MAXHTPTV0_70_CFilterBVeto.deriv.DAOD_HIGG3D1.e5340_s3126_r10201_p4164
mc16_13TeV.364172.Sherpa_221_NNPDF30NNLO_Wenu_MAXHTPTV0_70_BFilter.deriv.DAOD_HIGG3D1.e5340_s3126_r10201_p4164
mc16_13TeV.364173.Sherpa_221_NNPDF30NNLO_Wenu_MAXHTPTV70_140_CVetoBVeto.deriv.DAOD_HIGG3D1.e5340_s3126_r10201_p4164
mc16_13TeV.364174.Sherpa_221_NNPDF30NNLO_Wenu_MAXHTPTV70_140_CFilterBVeto.deriv.DAOD_HIGG3D1.e5340_s3126_r10201_p4164
mc16_13TeV.364175.Sherpa_221_NNPDF30NNLO_Wenu_MAXHTPTV70_140_BFilter.deriv.DAOD_HIGG3D1.e5340_s3126_r10201_p4164
mc16_13TeV.364176.Sherpa_221_NNPDF30NNLO_Wenu_MAXHTPTV140_280_CVetoBVeto.deriv.DAOD_HIGG3D1.e5340_s3126_r10201_p4164
mc16_13TeV.364177.Sherpa_221_NNPDF30NNLO_Wenu_MAXHTPTV140_280_CFilterBVeto.deriv.DAOD_HIGG3D1.e5340_s3126_r10201_p4164
mc16_13TeV.364178.Sherpa_221_NNPDF30NNLO_Wenu_MAXHTPTV140_280_BFilter.deriv.DAOD_HIGG3D1.e5340_s3126_r10201_p4164
mc16_13TeV.364179.Sherpa_221_NNPDF30NNLO_Wenu_MAXHTPTV280_500_CVetoBVeto.deriv.DAOD_HIGG3D1.e5340_s3126_r10201_p4164
mc16_13TeV.364180.Sherpa_221_NNPDF30NNLO_Wenu_MAXHTPTV280_500_CFilterBVeto.deriv.DAOD_HIGG3D1.e5340_s3126_r10201_p4164
mc16_13TeV.364181.Sherpa_221_NNPDF30NNLO_Wenu_MAXHTPTV280_500_BFilter.deriv.DAOD_HIGG3D1.e5340_s3126_r10201_p4164
mc16_13TeV.364182.Sherpa_221_NNPDF30NNLO_Wenu_MAXHTPTV500_1000.deriv.DAOD_HIGG3D1.e5340_s3126_r10201_p4164
mc16_13TeV.364183.Sherpa_221_NNPDF30NNLO_Wenu_MAXHTPTV1000_E_CMS.deriv.DAOD_HIGG3D1.e5340_s3126_r10201_p4164
mc16_13TeV.364184.Sherpa_221_NNPDF30NNLO_Wtaunu_MAXHTPTV0_70_CVetoBVeto.deriv.DAOD_HIGG3D1.e5340_s3126_r10201_p4164
mc16_13TeV.364185.Sherpa_221_NNPDF30NNLO_Wtaunu_MAXHTPTV0_70_CFilterBVeto.deriv.DAOD_HIGG3D1.e5340_s3126_r10201_p4164
mc16_13TeV.364186.Sherpa_221_NNPDF30NNLO_Wtaunu_MAXHTPTV0_70_BFilter.deriv.DAOD_HIGG3D1.e5340_s3126_r10201_p4164
mc16_13TeV.364187.Sherpa_221_NNPDF30NNLO_Wtaunu_MAXHTPTV70_140_CVetoBVeto.deriv.DAOD_HIGG3D1.e5340_s3126_r10201_p4164
mc16_13TeV.364188.Sherpa_221_NNPDF30NNLO_Wtaunu_MAXHTPTV70_140_CFilterBVeto.deriv.DAOD_HIGG3D1.e5340_s3126_r10201_p4164
mc16_13TeV.364189.Sherpa_221_NNPDF30NNLO_Wtaunu_MAXHTPTV70_140_BFilter.deriv.DAOD_HIGG3D1.e5340_s3126_r10201_p4164
mc16_13TeV.364190.Sherpa_221_NNPDF30NNLO_Wtaunu_MAXHTPTV140_280_CVetoBVeto.deriv.DAOD_HIGG3D1.e5340_s3126_r10201_p4164
```

mc16_13TeV.364191.Sherpa_221_NNPDF30NNLO_Wtaunu_MAXHTPTV140_280_CFilterBVeto.deriv.DAOD_HIGG3D1.e5340_s3126_r10201_p4164
mc16_13TeV.364192.Sherpa_221_NNPDF30NNLO_Wtaunu_MAXHTPTV140_280_BFilter.deriv.DAOD_HIGG3D1.e5340_s3126_r10201_p4164
mc16_13TeV.364193.Sherpa_221_NNPDF30NNLO_Wtaunu_MAXHTPTV280_500_CVetoBVeto.deriv.DAOD_HIGG3D1.e5340_s3126_r10201_p4164
mc16_13TeV.364194.Sherpa_221_NNPDF30NNLO_Wtaunu_MAXHTPTV280_500_CFilterBVeto.deriv.DAOD_HIGG3D1.e5340_s3126_r10201_p4164
mc16_13TeV.364195.Sherpa_221_NNPDF30NNLO_Wtaunu_MAXHTPTV280_500_BFilter.deriv.DAOD_HIGG3D1.e5340_s3126_r10201_p4164
mc16_13TeV.364196.Sherpa_221_NNPDF30NNLO_Wtaunu_MAXHTPTV500_1000.deriv.DAOD_HIGG3D1.e5340_s3126_r10201_p4164
mc16_13TeV.364197.Sherpa_221_NNPDF30NNLO_Wtaunu_MAXHTPTV1000_E_CMS.deriv.DAOD_HIGG3D1.e5340_s3126_r10201_p4164

$Z/\gamma* \to \mu\mu$+jets

mc16_13TeV.364100.Sherpa_221_NNPDF30NNLO_Zmumu_MAXHTPTV0_70_CVetoBVeto.deriv.DAOD_HIGG3D1.e5271_s3126_r10201_p4164
mc16_13TeV.364101.Sherpa_221_NNPDF30NNLO_Zmumu_MAXHTPTV0_70_CFilterBVeto.deriv.DAOD_HIGG3D1.e5271_s3126_r10201_p4164
mc16_13TeV.364102.Sherpa_221_NNPDF30NNLO_Zmumu_MAXHTPTV0_70_BFilter.deriv.DAOD_HIGG3D1.e5271_s3126_r10201_p4164
mc16_13TeV.364103.Sherpa_221_NNPDF30NNLO_Zmumu_MAXHTPTV70_140_CVetoBVeto.deriv.DAOD_HIGG3D1.e5271_s3126_r10201_p4164
mc16_13TeV.364104.Sherpa_221_NNPDF30NNLO_Zmumu_MAXHTPTV70_140_CFilterBVeto.deriv.DAOD_HIGG3D1.e5271_s3126_r10201_p4164
mc16_13TeV.364105.Sherpa_221_NNPDF30NNLO_Zmumu_MAXHTPTV70_140_BFilter.deriv.DAOD_HIGG3D1.e5271_s3126_r10201_p4164
mc16_13TeV.364106.Sherpa_221_NNPDF30NNLO_Zmumu_MAXHTPTV140_280_CVetoBVeto.deriv.DAOD_HIGG3D1.e5271_s3126_r10201_p4164
mc16_13TeV.364107.Sherpa_221_NNPDF30NNLO_Zmumu_MAXHTPTV140_280_CFilterBVeto.deriv.DAOD_HIGG3D1.e5271_s3126_r10201_p4164
mc16_13TeV.364108.Sherpa_221_NNPDF30NNLO_Zmumu_MAXHTPTV140_280_BFilter.deriv.DAOD_HIGG3D1.e5271_s3126_r10201_p4164
mc16_13TeV.364109.Sherpa_221_NNPDF30NNLO_Zmumu_MAXHTPTV280_500_CVetoBVeto.deriv.DAOD_HIGG3D1.e5271_s3126_r10201_p4164
mc16_13TeV.364110.Sherpa_221_NNPDF30NNLO_Zmumu_MAXHTPTV280_500_CFilterBVeto.deriv.DAOD_HIGG3D1.e5271_s3126_r10201_p4164
mc16_13TeV.364111.Sherpa_221_NNPDF30NNLO_Zmumu_MAXHTPTV280_500_BFilter.deriv.DAOD_HIGG3D1.e5271_s3126_r10201_p4164
mc16_13TeV.364112.Sherpa_221_NNPDF30NNLO_Zmumu_MAXHTPTV500_1000.deriv.DAOD_HIGG3D1.e5271_s3126_r10201_p4164
mc16_13TeV.364113.Sherpa_221_NNPDF30NNLO_Zmumu_MAXHTPTV1000_E_CMS.deriv.DAOD_HIGG3D1.e5271_s3126_r10201_p4164
mc16_13TeV.364198.Sherpa_221_NN30NNLO_Zmm_M110_40_MAXHTPTV0_70_BVeto.deriv.DAOD_HIGG3D1.e5421_s3126_r10201_p4164
mc16_13TeV.364199.Sherpa_221_NN30NNLO_Zmm_M110_40_MAXHTPTV0_70_BFilter.deriv.DAOD_HIGG3D1.e5421_s3126_r10201_p4164
mc16_13TeV.364200.Sherpa_221_NN30NNLO_Zmm_M110_40_MAXHTPTV70_280_BVeto.deriv.DAOD_HIGG3D1.e5421_s3126_r10201_p4164
mc16_13TeV.364201.Sherpa_221_NN30NNLO_Zmm_M110_40_MAXHTPTV70_280_BFilter.deriv.DAOD_HIGG3D1.e5421_s3126_r10201_p4164
mc16_13TeV.364202.Sherpa_221_NN30NNLO_Zmm_M110_40_MAXHTPTV280_E_CMS_BVeto.deriv.DAOD_HIGG3D1.e5421_s3126_r10201_p4164
mc16_13TeV.364203.Sherpa_221_NN30NNLO_Zmm_M110_40_MAXHTPTV280_E_CMS_BFilter.deriv.DAOD_HIGG3D1.e5421_s3126_r10201_p4164

mc16_13TeV.364281.Sherpa_221_NNPDF30NNLO_Zmumu_M112M1_MAXHTPTV280_E_CMS.deriv.DAOD_HIGG3D1.e6037_s3126_r10201_p4164

mc16_13TeV.364359.Sherpa_221_NNPDF30NNLO_Zmumu_M112M1_MAXHTPTV70_140.deriv.DAOD_HIGG3D1.e6544_a875_r10201_p4164

mc16_13TeV.364362.Sherpa_221_NNPDF30NNLO_Zmumu_M112M1_MAXHTPTV140_280.deriv.DAOD_HIGG3D1.e6544_a875_r10201_p4164

$Z/\gamma* \to ee$+jets

mc16_13TeV.364114.Sherpa_221_NNPDF30NNLO_Zee_MAXHTPTV0_70_CVetoBVeto.deriv.DAOD_HIGG3D1.e5299_s3126_r10201_p4164

mc16_13TeV.364115.Sherpa_221_NNPDF30NNLO_Zee_MAXHTPTV0_70_CFilterBVeto.deriv.DAOD_HIGG3D1.e5299_s3126_r10201_p4164

mc16_13TeV.364116.Sherpa_221_NNPDF30NNLO_Zee_MAXHTPTV0_70_BFilter.deriv.DAOD_HIGG3D1.e5299_s3126_r10201_p4164

mc16_13TeV.364117.Sherpa_221_NNPDF30NNLO_Zee_MAXHTPTV70_140_CVetoBVeto.deriv.DAOD_HIGG3D1.e5299_s3126_r10201_p4164

mc16_13TeV.364118.Sherpa_221_NNPDF30NNLO_Zee_MAXHTPTV70_140_CFilterBVeto.deriv.DAOD_HIGG3D1.e5299_s3126_r10201_p4164

mc16_13TeV.364119.Sherpa_221_NNPDF30NNLO_Zee_MAXHTPTV70_140_BFilter.deriv.DAOD_HIGG3D1.e5299_s3126_r10201_p4164

mc16_13TeV.364120.Sherpa_221_NNPDF30NNLO_Zee_MAXHTPTV140_280_CVetoBVeto.deriv.DAOD_HIGG3D1.e5299_s3126_r10201_p4164

mc16_13TeV.364121.Sherpa_221_NNPDF30NNLO_Zee_MAXHTPTV140_280_CFilterBVeto.deriv.DAOD_HIGG3D1.e5299_s3126_r10201_p4164

mc16_13TeV.364122.Sherpa_221_NNPDF30NNLO_Zee_MAXHTPTV140_280_BFilter.deriv.DAOD_HIGG3D1.e5299_s3126_r10201_p4164

mc16_13TeV.364123.Sherpa_221_NNPDF30NNLO_Zee_MAXHTPTV280_500_CVetoBVeto.deriv.DAOD_HIGG3D1.e5299_s3126_r10201_p4164

mc16_13TeV.364124.Sherpa_221_NNPDF30NNLO_Zee_MAXHTPTV280_500_CFilterBVeto.deriv.DAOD_HIGG3D1.e5299_s3126_r10201_p4164

mc16_13TeV.364125.Sherpa_221_NNPDF30NNLO_Zee_MAXHTPTV280_500_BFilter.deriv.DAOD_HIGG3D1.e5299_s3126_r10201_p4164

mc16_13TeV.364126.Sherpa_221_NNPDF30NNLO_Zee_MAXHTPTV500_1000.deriv.DAOD_HIGG3D1.e5299_s3126_r10201_p4164

mc16_13TeV.364127.Sherpa_221_NNPDF30NNLO_Zee_MAXHTPTV1000_E_CMS.deriv.DAOD_HIGG3D1.e5299_s3126_r10201_p4164

mc16_13TeV.364204.Sherpa_221_NN30NNLO_Zee_M110_40_MAXHTPTV0_70_BVeto.deriv.DAOD_HIGG3D1.e5421_s3126_r10201_p4164

mc16_13TeV.364205.Sherpa_221_NN30NNLO_Zee_M110_40_MAXHTPTV0_70_BFilter.deriv.DAOD_HIGG3D1.e5421_s3126_r10201_p4164

mc16_13TeV.364206.Sherpa_221_NN30NNLO_Zee_M110_40_MAXHTPTV70_280_BVeto.deriv.DAOD_HIGG3D1.e5421_s3126_r10201_p4164

mc16_13TeV.364207.Sherpa_221_NN30NNLO_Zee_M110_40_MAXHTPTV70_280_BFilter.deriv.DAOD_HIGG3D1.e5421_s3126_r10201_p4164

mc16_13TeV.364208.Sherpa_221_NN30NNLO_Zee_M110_40_MAXHTPTV280_E_CMS_BVeto.deriv.DAOD_HIGG3D1.e5421_s3126_r10201_p4164

mc16_13TeV.364209.Sherpa_221_NN30NNLO_Zee_M110_40_MAXHTPTV280_E_CMS_BFilter.deriv.DAOD_HIGG3D1.e5421_s3126_r10201_p4164

mc16_13TeV.364280.Sherpa_221_NNPDF30NNLO_Zee_M112M1_MAXHTPTV280_E_CMS.deriv.DAOD_HIGG3D1.e6037_s3126_r10201_p4164

mc16_13TeV.364358.Sherpa_221_NNPDF30NNLO_Zee_M112M1_MAXHTPTV70_140.deriv.DAOD_HIGG3D1.e6544_a875_r10201_p4164

mc16_13TeV.364361.Sherpa_221_NNPDF30NNLO_Zee_M112M1_MAXHTPTV140_280.deriv.DAOD_HIGG3D1.e6544_a875_r10201_p4164

$t\bar{t}$, single top

mc16_13TeV.410470.PhPy8EG_A14_ttbar_hdamp258p75_nonallhad.deriv.DAOD_HIGG3D1.e6337_s3126_r10201_p4164

mc16_13TeV.410644.PowhegPythia8EvtGen_A14_singletop_schan_lept_top.deriv.DAOD_HIGG3D1.e6527_s3126_r10201_p4164
mc16_13TeV.410645.PowhegPythia8EvtGen_A14_singletop_schan_lept_antitop.deriv.DAOD_HIGG3D1.e6527_s3126_r10201_p4164
mc16_13TeV.410648.PowhegPythia8EvtGen_A14_Wt_DR_dilepton_top.deriv.DAOD_HIGG3D1.e6615_s3126_r10201_p4164
mc16_13TeV.410649.PowhegPythia8EvtGen_A14_Wt_DR_dilepton_antitop.deriv.DAOD_HIGG3D1.e6615_s3126_r10201_p4164
mc16_13TeV.410658.PhPy8EG_A14_tchan_BW50_lept_top.deriv.DAOD_HIGG3D1.e6671_s3126_r10201_p4164
mc16_13TeV.410659.PhPy8EG_A14_tchan_BW50_lept_antitop.deriv.DAOD_HIGG3D1.e6671_s3126_r10201_p4164

SM Higgs

mc16_13TeV.345120.PowhegPy8EG_NNLOPS_nnlo_30_ggH125_tautaul1317.deriv.DAOD_HIGG3D1.e5814_s3126_r10201_p4164

mc16_13TeV.345121.PowhegPy8EG_NNLOPS_nnlo_30_ggH125_tautaulm15hp20.deriv.DAOD_HIGG3D1.e5814_s3126_r10201_p4164
mc16_13TeV.345122.PowhegPy8EG_NNLOPS_nnlo_30_ggH125_tautaulp15hm20.deriv.DAOD_HIGG3D1.e5814_s3126_r10201_p4164
mc16_13TeV.345123.PowhegPy8EG_NNLOPS_nnlo_30_ggH125_tautauh30h20.deriv.DAOD_HIGG3D1.e5814_s3126_r10201_p4164
mc16_13TeV.345211.PowhegPy8EG_NNPDF30_AZNLO_WmH125J_Winc_MINLO_tautau.tautau.deriv.DAOD_HIGG3D1.e5808_s3126_r10201_p4164
mc16_13TeV.345212.PowhegPy8EG_NNPDF30_AZNLO_WpH125J_Winc_MINLO_tautau.tautau.deriv.DAOD_HIGG3D1.e5808_s3126_r10201_p4164
mc16_13TeV.345217.PowhegPy8EG_NNPDF30_AZNLO_ZH125J_Zinc_MINLO_tautau.tautau.deriv.DAOD_HIGG3D1.e5808_s3126_r10201_p4164
mc16_13TeV.345324.PowhegPythia8EvtGen_NNLOPS_NN30_ggH125_WWlvlv_EF_15_5.deriv.DAOD_HIGG3D1.e5769_s3126_r10201_p4166
mc16_13TeV.345948.PowhegPy8EG_NNPDF30_AZNLOCTEQ6L1_VBFH125_WWlvlv.deriv.DAOD_HIGG3D1.e7172_s3126_r10201_p4166
mc16_13TeV.346190.PowhegPy8EG_NNPDF30_AZNLOCTEQ6L1_VBFH125_tautaul1317.deriv.DAOD_HIGG3D1.e7259_s3126_r10201_p4164

A.3. mc16e

gluon-fusion A production

mc16_13TeV.346025.Pythia8EvtGen_A14NNPDF23LO_ggA60_tautau_leplep.deriv.DAOD_HIGG3D1.e7122_a875_r10724_p4164

mc16_13TeV.346026.Pythia8EvtGen_A14NNPDF23LO_ggA70_tautau_leplep.deriv.DAOD_HIGG3D1.e7122_a875_r10724_p4164
mc16_13TeV.346027.Pythia8EvtGen_A14NNPDF23LO_ggA80_tautau_leplep.deriv.DAOD_HIGG3D1.e7122_a875_r10724_p4164
mc16_13TeV.346028.Pythia8EvtGen_A14NNPDF23LO_ggA90_tautau_leplep.deriv.DAOD_HIGG3D1.e7122_a875_r10724_p4164

```
mc16_13TeV.346375.Pythia8EvtGen_A14NNPDF23LO_ggA50_tautau_leplep.deriv.DAOD_HIGG3D1.e7122_a875_r10724_p4164
mc16_13TeV.451705.Pythia8EvtGen_A14NNPDF23LO_ggA40_tautau_leplep.deriv.DAOD_HIGG3D1.e8139_a875_r10724_p4164
mc16_13TeV.801162.Py8EG_A14NNPDF23LO_ggA20_tautau_11314.deriv.DAOD_HIGG3D1.e8307_a875_r10724_p4164
mc16_13TeV.801163.Py8EG_A14NNPDF23LO_ggA30_tautau_11314.deriv.DAOD_HIGG3D1.e8307_a875_r10724_p4164
mc16_13TeV.801827.Py8EG_A14NNPDF23LO_ggA100_tautau_11314.deriv.DAOD_HIGG3D1.e8307_a875_r10724_p4164
mc16_13TeV.801828.Py8EG_A14NNPDF23LO_ggA110_tautau_11314.deriv.DAOD_HIGG3D1.e8307_a875_r10724_p4164
```

$Z/\gamma^* \to \tau\tau$+jets

```
mc16_13TeV.364128.Sherpa_221_NNPDF30NNLO_Ztautau_MAXHTPTV0_70_CVetoBVeto.deriv.DAOD_HIGG3D1.e5307_s3126_r10724_p4164
mc16_13TeV.364129.Sherpa_221_NNPDF30NNLO_Ztautau_MAXHTPTV0_70_CFilterBVeto.deriv.DAOD_HIGG3D1.e5307_s3126_r10724_p4164
mc16_13TeV.364130.Sherpa_221_NNPDF30NNLO_Ztautau_MAXHTPTV0_70_BFilter.deriv.DAOD_HIGG3D1.e5307_s3126_r10724_p4164
mc16_13TeV.364131.Sherpa_221_NNPDF30NNLO_Ztautau_MAXHTPTV70_140_CVetoBVeto.deriv.DAOD_HIGG3D1.e5307_s3126_r10724_p4164
mc16_13TeV.364132.Sherpa_221_NNPDF30NNLO_Ztautau_MAXHTPTV70_140_CFilterBVeto.deriv.DAOD_HIGG3D1.e5307_s3126_r10724_p4164
mc16_13TeV.364133.Sherpa_221_NNPDF30NNLO_Ztautau_MAXHTPTV70_140_BFilter.deriv.DAOD_HIGG3D1.e5307_s3126_r10724_p4164
mc16_13TeV.364134.Sherpa_221_NNPDF30NNLO_Ztautau_MAXHTPTV140_280_CVetoBVeto.deriv.DAOD_HIGG3D1.e5307_s3126_r10724_p4164
mc16_13TeV.364135.Sherpa_221_NNPDF30NNLO_Ztautau_MAXHTPTV140_280_CFilterBVeto.deriv.DAOD_HIGG3D1.e5307_s3126_r10724_p4164
mc16_13TeV.364136.Sherpa_221_NNPDF30NNLO_Ztautau_MAXHTPTV140_280_BFilter.deriv.DAOD_HIGG3D1.e5307_s3126_r10724_p4164
mc16_13TeV.364137.Sherpa_221_NNPDF30NNLO_Ztautau_MAXHTPTV280_500_CVetoBVeto.deriv.DAOD_HIGG3D1.e5307_s3126_r10724_p4164
mc16_13TeV.364138.Sherpa_221_NNPDF30NNLO_Ztautau_MAXHTPTV280_500_CFilterBVeto.deriv.DAOD_HIGG3D1.e5313_s3126_r10724_p4164
mc16_13TeV.364139.Sherpa_221_NNPDF30NNLO_Ztautau_MAXHTPTV280_500_BFilter.deriv.DAOD_HIGG3D1.e5307_s3126_r10724_p4164
mc16_13TeV.364140.Sherpa_221_NNPDF30NNLO_Ztautau_MAXHTPTV500_1000.deriv.DAOD_HIGG3D1.e5307_s3126_r10724_p4164
mc16_13TeV.364141.Sherpa_221_NNPDF30NNLO_Ztautau_MAXHTPTV1000_E_CMS.deriv.DAOD_HIGG3D1.e5307_s3126_r10724_p4164
mc16_13TeV.364210.Sherpa_221_NN30NNLO_Ztt_M110_40_MAXHTPTV0_70_BVeto.deriv.DAOD_HIGG3D1.e5421_s3126_r10724_p4164
mc16_13TeV.364211.Sherpa_221_NN30NNLO_Ztt_M110_40_MAXHTPTV0_70_BFilter.deriv.DAOD_HIGG3D1.e5421_s3126_r10724_p4164
mc16_13TeV.364212.Sherpa_221_NN30NNLO_Ztt_M110_40_MAXHTPTV70_280_BVeto.deriv.DAOD_HIGG3D1.e5421_s3126_r10724_p4164
mc16_13TeV.364213.Sherpa_221_NN30NNLO_Ztt_M110_40_MAXHTPTV70_280_BFilter.deriv.DAOD_HIGG3D1.e5421_s3126_r10724_p4164
mc16_13TeV.364214.Sherpa_221_NN30NNLO_Ztt_M110_40_MAXHTPTV280_E_CMS_BVeto.deriv.DAOD_HIGG3D1.e5421_s3126_r10724_p4164
mc16_13TeV.364215.Sherpa_221_NN30NNLO_Ztt_M110_40_MAXHTPTV280_E_CMS_BFilter.deriv.DAOD_HIGG3D1.e5421_s3126_r10724_p4164
mc16_13TeV.364282.Sherpa_221_NNPDF30NNLO_Ztautau_Ml12M1_MAXHTPTV280_E_CMS.deriv.DAOD_HIGG3D1.e6037_s3126_r10724_p4164
```

mc16_13TeV.364360.Sherpa_221_NNPDF30NNLO_Ztautau_Ml12Ml_MAXHTPTV70_140.deriv.DAOD_HIGG3D1.e6544_a875_r10724_p4164
mc16_13TeV.364363.Sherpa_221_NNPDF30NNLO_Ztautau_Ml12Ml_MAXHTPTV140_280.deriv.DAOD_HIGG3D1.e6544_a875_r10724_p4164

Diboson

mc16_13TeV.363355.Sherpa_221_NNPDF30NNLO_ZqqZvv.deriv.DAOD_HIGG3D1.e5525_s3126_r10724_p4164
mc16_13TeV.363356.Sherpa_221_NNPDF30NNLO_ZqqZll.deriv.DAOD_HIGG3D1.e5525_s3126_r10724_p4164
mc16_13TeV.363357.Sherpa_221_NNPDF30NNLO_WqqZvv.deriv.DAOD_HIGG3D1.e5525_s3126_r10724_p4164
mc16_13TeV.363358.Sherpa_221_NNPDF30NNLO_WqqZll.deriv.DAOD_HIGG3D1.e5525_s3126_r10724_p4164
mc16_13TeV.363359.Sherpa_221_NNPDF30NNLO_WpqqWmlv.deriv.DAOD_HIGG3D1.e5583_s3126_r10724_p4164
mc16_13TeV.363360.Sherpa_221_NNPDF30NNLO_WplvWmqq.deriv.DAOD_HIGG3D1.e5983_s3126_r10724_p4164
mc16_13TeV.363489.Sherpa_221_NNPDF30NNLO_WlvZqq.deriv.DAOD_HIGG3D1.e5525_s3126_r10724_p4164
mc16_13TeV.364250.Sherpa_222_NNPDF30NNLO_llll.deriv.DAOD_HIGG3D1.e5894_s3126_r10724_p4164
mc16_13TeV.364253.Sherpa_222_NNPDF30NNLO_lllv.deriv.DAOD_HIGG3D1.e5916_s3126_r10724_p4164
mc16_13TeV.364254.Sherpa_222_NNPDF30NNLO_llvv.deriv.DAOD_HIGG3D1.e5916_s3126_r10724_p4166
mc16_13TeV.364255.Sherpa_222_NNPDF30NNLO_lvvv.deriv.DAOD_HIGG3D1.e5916_s3126_r10724_p4164
mc16_13TeV.364286.Sherpa_222_NNPDF30NNLO_llvvjj_ss_EW4.deriv.DAOD_HIGG3D1.e6055_s3126_r10724_p4164
mc16_13TeV.364288.Sherpa_222_NNPDF30NNLO_llll_lowMllPtComplement.deriv.DAOD_HIGG3D1.e6096_s3126_r10724_p4164
mc16_13TeV.364289.Sherpa_222_NNPDF30NNLO_lllv_lowMllPtComplement.deriv.DAOD_HIGG3D1.e6133_s3126_r10724_p4164
mc16_13TeV.364290.Sherpa_222_NNPDF30NNLO_llvv_lowMllPtComplement.deriv.DAOD_HIGG3D1.e6096_s3126_r10724_p4164

$W \rightarrow l\nu$+jets

mc16_13TeV.364156.Sherpa_221_NNPDF30NNLO_Wmunu_MAXHTPTV0_70_CVetoBVeto.deriv.DAOD_HIGG3D1.e5340_s3126_r10724_p4164
mc16_13TeV.364157.Sherpa_221_NNPDF30NNLO_Wmunu_MAXHTPTV0_70_CFilterBVeto.deriv.DAOD_HIGG3D1.e5340_s3126_r10724_p4164
mc16_13TeV.364158.Sherpa_221_NNPDF30NNLO_Wmunu_MAXHTPTV0_70_BFilter.deriv.DAOD_HIGG3D1.e5340_s3126_r10724_p4164
mc16_13TeV.364159.Sherpa_221_NNPDF30NNLO_Wmunu_MAXHTPTV70_140_CVetoBVeto.deriv.DAOD_HIGG3D1.e5340_s3126_r10724_p4164
mc16_13TeV.364160.Sherpa_221_NNPDF30NNLO_Wmunu_MAXHTPTV70_140_CFilterBVeto.deriv.DAOD_HIGG3D1.e5340_s3126_r10724_p4164
mc16_13TeV.364161.Sherpa_221_NNPDF30NNLO_Wmunu_MAXHTPTV70_140_BFilter.deriv.DAOD_HIGG3D1.e5340_s3126_r10724_p4164
mc16_13TeV.364162.Sherpa_221_NNPDF30NNLO_Wmunu_MAXHTPTV140_280_CVetoBVeto.deriv.DAOD_HIGG3D1.e5340_s3126_r10724_p4164
mc16_13TeV.364163.Sherpa_221_NNPDF30NNLO_Wmunu_MAXHTPTV140_280_CFilterBVeto.deriv.DAOD_HIGG3D1.e5340_s3126_r10724_p4164

```
mc16_13TeV.364164.Sherpa_221_NNPDF30NNLO_Wmunu_MAXHTPTV140_280_BFilter.deriv.DAOD_HIGG3D1.e5340_s3126_r10724_p4164
mc16_13TeV.364165.Sherpa_221_NNPDF30NNLO_Wmunu_MAXHTPTV280_500_CVetoBVeto.deriv.DAOD_HIGG3D1.e5340_s3126_r10724_p4164
mc16_13TeV.364166.Sherpa_221_NNPDF30NNLO_Wmunu_MAXHTPTV280_500_CFilterBVeto.deriv.DAOD_HIGG3D1.e5340_s3126_r10724_p4164
mc16_13TeV.364167.Sherpa_221_NNPDF30NNLO_Wmunu_MAXHTPTV280_500_BFilter.deriv.DAOD_HIGG3D1.e5340_s3126_r10724_p4164
mc16_13TeV.364168.Sherpa_221_NNPDF30NNLO_Wmunu_MAXHTPTV500_1000.deriv.DAOD_HIGG3D1.e5340_s3126_r10724_p4164
mc16_13TeV.364169.Sherpa_221_NNPDF30NNLO_Wmunu_MAXHTPTV1000_E_CMS.deriv.DAOD_HIGG3D1.e5340_s3126_r10724_p4164
mc16_13TeV.364170.Sherpa_221_NNPDF30NNLO_Wenu_MAXHTPTV0_70_CVetoBVeto.deriv.DAOD_HIGG3D1.e5340_s3126_r10724_p4164
mc16_13TeV.364171.Sherpa_221_NNPDF30NNLO_Wenu_MAXHTPTV0_70_CFilterBVeto.deriv.DAOD_HIGG3D1.e5340_s3126_r10724_p4164
mc16_13TeV.364172.Sherpa_221_NNPDF30NNLO_Wenu_MAXHTPTV0_70_BFilter.deriv.DAOD_HIGG3D1.e5340_s3126_r10724_p4164
mc16_13TeV.364173.Sherpa_221_NNPDF30NNLO_Wenu_MAXHTPTV70_140_CVetoBVeto.deriv.DAOD_HIGG3D1.e5340_s3126_r10724_p4164
mc16_13TeV.364174.Sherpa_221_NNPDF30NNLO_Wenu_MAXHTPTV70_140_CFilterBVeto.deriv.DAOD_HIGG3D1.e5340_s3126_r10724_p4164
mc16_13TeV.364175.Sherpa_221_NNPDF30NNLO_Wenu_MAXHTPTV70_140_BFilter.deriv.DAOD_HIGG3D1.e5340_s3126_r10724_p4164
mc16_13TeV.364176.Sherpa_221_NNPDF30NNLO_Wenu_MAXHTPTV140_280_CVetoBVeto.deriv.DAOD_HIGG3D1.e5340_s3126_r10724_p4164
mc16_13TeV.364177.Sherpa_221_NNPDF30NNLO_Wenu_MAXHTPTV140_280_CFilterBVeto.deriv.DAOD_HIGG3D1.e5340_s3126_r10724_p4164
mc16_13TeV.364178.Sherpa_221_NNPDF30NNLO_Wenu_MAXHTPTV140_280_BFilter.deriv.DAOD_HIGG3D1.e5340_s3126_r10724_p4164
mc16_13TeV.364179.Sherpa_221_NNPDF30NNLO_Wenu_MAXHTPTV280_500_CVetoBVeto.deriv.DAOD_HIGG3D1.e5340_s3126_r10724_p4164
mc16_13TeV.364180.Sherpa_221_NNPDF30NNLO_Wenu_MAXHTPTV280_500_CFilterBVeto.deriv.DAOD_HIGG3D1.e5340_s3126_r10724_p4164
mc16_13TeV.364181.Sherpa_221_NNPDF30NNLO_Wenu_MAXHTPTV280_500_BFilter.deriv.DAOD_HIGG3D1.e5340_s3126_r10724_p4164
mc16_13TeV.364182.Sherpa_221_NNPDF30NNLO_Wenu_MAXHTPTV500_1000.deriv.DAOD_HIGG3D1.e5340_s3126_r10724_p4164
mc16_13TeV.364183.Sherpa_221_NNPDF30NNLO_Wenu_MAXHTPTV1000_E_CMS.deriv.DAOD_HIGG3D1.e5340_s3126_r10724_p4164
mc16_13TeV.364184.Sherpa_221_NNPDF30NNLO_Wtaunu_MAXHTPTV0_70_CVetoBVeto.deriv.DAOD_HIGG3D1.e5340_s3126_r10724_p4164
mc16_13TeV.364185.Sherpa_221_NNPDF30NNLO_Wtaunu_MAXHTPTV0_70_CFilterBVeto.deriv.DAOD_HIGG3D1.e5340_s3126_r10724_p4164
mc16_13TeV.364186.Sherpa_221_NNPDF30NNLO_Wtaunu_MAXHTPTV0_70_BFilter.deriv.DAOD_HIGG3D1.e5340_s3126_r10724_p4164
mc16_13TeV.364187.Sherpa_221_NNPDF30NNLO_Wtaunu_MAXHTPTV70_140_CVetoBVeto.deriv.DAOD_HIGG3D1.e5340_s3126_r10724_p4164
mc16_13TeV.364188.Sherpa_221_NNPDF30NNLO_Wtaunu_MAXHTPTV70_140_CFilterBVeto.deriv.DAOD_HIGG3D1.e5340_s3126_r10724_p4164
mc16_13TeV.364189.Sherpa_221_NNPDF30NNLO_Wtaunu_MAXHTPTV70_140_BFilter.deriv.DAOD_HIGG3D1.e5340_s3126_r10724_p4164
mc16_13TeV.364190.Sherpa_221_NNPDF30NNLO_Wtaunu_MAXHTPTV140_280_CVetoBVeto.deriv.DAOD_HIGG3D1.e5340_s3126_r10724_p4164
mc16_13TeV.364191.Sherpa_221_NNPDF30NNLO_Wtaunu_MAXHTPTV140_280_CFilterBVeto.deriv.DAOD_HIGG3D1.e5340_s3126_r10724_p4164
mc16_13TeV.364192.Sherpa_221_NNPDF30NNLO_Wtaunu_MAXHTPTV140_280_BFilter.deriv.DAOD_HIGG3D1.e5340_s3126_r10724_p4164
```

```
mc16_13TeV.364193.Sherpa_221_NNPDF30NNLO_Wtaunu_MAXHTPTV280_500_CVetoBVeto.deriv.DAOD_HIGG3D1.e5340_s3126_r10724_p4164
mc16_13TeV.364194.Sherpa_221_NNPDF30NNLO_Wtaunu_MAXHTPTV280_500_CFilterBVeto.deriv.DAOD_HIGG3D1.e5340_s3126_r10724_p4164
mc16_13TeV.364195.Sherpa_221_NNPDF30NNLO_Wtaunu_MAXHTPTV280_500_BFilter.deriv.DAOD_HIGG3D1.e5340_s3126_r10724_p4164
mc16_13TeV.364196.Sherpa_221_NNPDF30NNLO_Wtaunu_MAXHTPTV500_1000.deriv.DAOD_HIGG3D1.e5340_s3126_r10724_p4164
mc16_13TeV.364197.Sherpa_221_NNPDF30NNLO_Wtaunu_MAXHTPTV1000_E_CMS.deriv.DAOD_HIGG3D1.e5340_s3126_r10724_p4164
```

$Z/\gamma* \to \mu\mu$+jets

```
mc16_13TeV.364100.Sherpa_221_NNPDF30NNLO_Zmumu_MAXHTPTV0_70_CVetoBVeto.deriv.DAOD_HIGG3D1.e5271_s3126_r10724_p4164
mc16_13TeV.364101.Sherpa_221_NNPDF30NNLO_Zmumu_MAXHTPTV0_70_CFilterBVeto.deriv.DAOD_HIGG3D1.e5271_s3126_r10724_p4164
mc16_13TeV.364102.Sherpa_221_NNPDF30NNLO_Zmumu_MAXHTPTV0_70_BFilter.deriv.DAOD_HIGG3D1.e5271_s3126_r10724_p4164
mc16_13TeV.364103.Sherpa_221_NNPDF30NNLO_Zmumu_MAXHTPTV70_140_CVetoBVeto.deriv.DAOD_HIGG3D1.e5271_s3126_r10724_p4164
mc16_13TeV.364104.Sherpa_221_NNPDF30NNLO_Zmumu_MAXHTPTV70_140_CFilterBVeto.deriv.DAOD_HIGG3D1.e5271_s3126_r10724_p4164
mc16_13TeV.364105.Sherpa_221_NNPDF30NNLO_Zmumu_MAXHTPTV70_140_BFilter.deriv.DAOD_HIGG3D1.e5271_s3126_r10724_p4164
mc16_13TeV.364106.Sherpa_221_NNPDF30NNLO_Zmumu_MAXHTPTV140_280_CVetoBVeto.deriv.DAOD_HIGG3D1.e5271_s3126_r10724_p4164
mc16_13TeV.364107.Sherpa_221_NNPDF30NNLO_Zmumu_MAXHTPTV140_280_CFilterBVeto.deriv.DAOD_HIGG3D1.e5271_s3126_r10724_p4164
mc16_13TeV.364108.Sherpa_221_NNPDF30NNLO_Zmumu_MAXHTPTV140_280_BFilter.deriv.DAOD_HIGG3D1.e5271_s3126_r10724_p4164
mc16_13TeV.364109.Sherpa_221_NNPDF30NNLO_Zmumu_MAXHTPTV280_500_CVetoBVeto.deriv.DAOD_HIGG3D1.e5271_s3126_r10724_p4164
mc16_13TeV.364110.Sherpa_221_NNPDF30NNLO_Zmumu_MAXHTPTV280_500_CFilterBVeto.deriv.DAOD_HIGG3D1.e5271_s3126_r10724_p4164
mc16_13TeV.364111.Sherpa_221_NNPDF30NNLO_Zmumu_MAXHTPTV280_500_BFilter.deriv.DAOD_HIGG3D1.e5271_s3126_r10724_p4164
mc16_13TeV.364112.Sherpa_221_NNPDF30NNLO_Zmumu_MAXHTPTV500_1000.deriv.DAOD_HIGG3D1.e5271_s3126_r10724_p4164
mc16_13TeV.364113.Sherpa_221_NNPDF30NNLO_Zmumu_MAXHTPTV1000_E_CMS.deriv.DAOD_HIGG3D1.e5271_s3126_r10724_p4164
mc16_13TeV.364198.Sherpa_221_NN30NNLO_Zmm_M110_40_MAXHTPTV0_70_BVeto.deriv.DAOD_HIGG3D1.e5421_s3126_r10724_p4164
mc16_13TeV.364199.Sherpa_221_NN30NNLO_Zmm_M110_40_MAXHTPTV0_70_BFilter.deriv.DAOD_HIGG3D1.e5421_s3126_r10724_p4164
mc16_13TeV.364200.Sherpa_221_NN30NNLO_Zmm_M110_40_MAXHTPTV70_280_BVeto.deriv.DAOD_HIGG3D1.e5421_s3126_r10724_p4164
mc16_13TeV.364201.Sherpa_221_NN30NNLO_Zmm_M110_40_MAXHTPTV70_280_BFilter.deriv.DAOD_HIGG3D1.e5421_s3126_r10724_p4164
mc16_13TeV.364202.Sherpa_221_NN30NNLO_Zmm_M110_40_MAXHTPTV280_E_CMS_BVeto.deriv.DAOD_HIGG3D1.e5421_s3126_r10724_p4164
mc16_13TeV.364203.Sherpa_221_NN30NNLO_Zmm_M110_40_MAXHTPTV280_E_CMS_BFilter.deriv.DAOD_HIGG3D1.e5421_s3126_r10724_p4164
mc16_13TeV.364281.Sherpa_221_NNPDF30NNLO_Zmumu_M112M1_MAXHTPTV280_E_CMS.deriv.DAOD_HIGG3D1.e6037_s3126_r10724_p4164
mc16_13TeV.364359.Sherpa_221_NNPDF30NNLO_Zmumu_M112M1_MAXHTPTV70_140.deriv.DAOD_HIGG3D1.e6544_a875_r10724_p4164
```

mc16_13TeV.364362.Sherpa_221_NNPDF30NNLO_Zmumu_M112M1_MAXHTPTV140_280.deriv.DAOD_HIGG3D1.e6544_a875_r10724_p4164

$Z/\gamma* \to ee$+jets

mc16_13TeV.364114.Sherpa_221_NNPDF30NNLO_Zee_MAXHTPTV0_70_CVetoBVeto.deriv.DAOD_HIGG3D1.e5299_s3126_r10724_p4164

mc16_13TeV.364115.Sherpa_221_NNPDF30NNLO_Zee_MAXHTPTV0_70_CFilterBVeto.deriv.DAOD_HIGG3D1.e5299_s3126_r10724_p4164

mc16_13TeV.364116.Sherpa_221_NNPDF30NNLO_Zee_MAXHTPTV0_70_BFilter.deriv.DAOD_HIGG3D1.e5299_s3126_r10724_p4164

mc16_13TeV.364117.Sherpa_221_NNPDF30NNLO_Zee_MAXHTPTV70_140_CVetoBVeto.deriv.DAOD_HIGG3D1.e5299_s3126_r10724_p4164

mc16_13TeV.364118.Sherpa_221_NNPDF30NNLO_Zee_MAXHTPTV70_140_CFilterBVeto.deriv.DAOD_HIGG3D1.e5299_s3126_r10724_p4164

mc16_13TeV.364119.Sherpa_221_NNPDF30NNLO_Zee_MAXHTPTV70_140_BFilter.deriv.DAOD_HIGG3D1.e5299_s3126_r10724_p4164

mc16_13TeV.364120.Sherpa_221_NNPDF30NNLO_Zee_MAXHTPTV140_280_CVetoBVeto.deriv.DAOD_HIGG3D1.e5299_s3126_r10724_p4164

mc16_13TeV.364121.Sherpa_221_NNPDF30NNLO_Zee_MAXHTPTV140_280_CFilterBVeto.deriv.DAOD_HIGG3D1.e5299_s3126_r10724_p4164

mc16_13TeV.364122.Sherpa_221_NNPDF30NNLO_Zee_MAXHTPTV140_280_BFilter.deriv.DAOD_HIGG3D1.e5299_s3126_r10724_p4164

mc16_13TeV.364123.Sherpa_221_NNPDF30NNLO_Zee_MAXHTPTV280_500_CVetoBVeto.deriv.DAOD_HIGG3D1.e5299_s3126_r10724_p4164

mc16_13TeV.364124.Sherpa_221_NNPDF30NNLO_Zee_MAXHTPTV280_500_CFilterBVeto.deriv.DAOD_HIGG3D1.e5299_s3126_r10724_p4164

mc16_13TeV.364125.Sherpa_221_NNPDF30NNLO_Zee_MAXHTPTV280_500_BFilter.deriv.DAOD_HIGG3D1.e5299_s3126_r10724_p4164

mc16_13TeV.364126.Sherpa_221_NNPDF30NNLO_Zee_MAXHTPTV500_1000.deriv.DAOD_HIGG3D1.e5299_s3126_r10724_p4164

mc16_13TeV.364127.Sherpa_221_NNPDF30NNLO_Zee_MAXHTPTV1000_E_CMS.deriv.DAOD_HIGG3D1.e5299_s3126_r10724_p4164

mc16_13TeV.364204.Sherpa_221_NN30NNLO_Zee_Ml110_40_MAXHTPTV0_70_BVeto.deriv.DAOD_HIGG3D1.e5421_s3126_r10724_p4164

mc16_13TeV.364205.Sherpa_221_NN30NNLO_Zee_Ml110_40_MAXHTPTV0_70_BFilter.deriv.DAOD_HIGG3D1.e5421_s3126_r10724_p4164

mc16_13TeV.364206.Sherpa_221_NN30NNLO_Zee_Ml110_40_MAXHTPTV70_280_BVeto.deriv.DAOD_HIGG3D1.e5421_s3126_r10724_p4164

mc16_13TeV.364207.Sherpa_221_NN30NNLO_Zee_Ml110_40_MAXHTPTV70_280_BFilter.deriv.DAOD_HIGG3D1.e5421_s3126_r10724_p4164

mc16_13TeV.364208.Sherpa_221_NN30NNLO_Zee_Ml110_40_MAXHTPTV280_E_CMS_BVeto.deriv.DAOD_HIGG3D1.e5421_s3126_r10724_p4164

mc16_13TeV.364209.Sherpa_221_NN30NNLO_Zee_Ml110_40_MAXHTPTV280_E_CMS_BFilter.deriv.DAOD_HIGG3D1.e5421_s3126_r10724_p4164

mc16_13TeV.364280.Sherpa_221_NNPDF30NNLO_Zee_Ml12M1_MAXHTPTV280_E_CMS.deriv.DAOD_HIGG3D1.e6037_s3126_r10724_p4164

mc16_13TeV.364358.Sherpa_221_NNPDF30NNLO_Zee_Ml12M1_MAXHTPTV70_140.deriv.DAOD_HIGG3D1.e6544_a875_r10724_p4164

mc16_13TeV.364361.Sherpa_221_NNPDF30NNLO_Zee_Ml12M1_MAXHTPTV140_280.deriv.DAOD_HIGG3D1.e6544_a875_r10724_p4164

$t\bar{t}$, single top

mc16_13TeV.410470.PhPy8EG_A14_ttbar_hdamp258p75_nonallhad.deriv.DAOD_HIGG3D1.e6337_s3126_r10724_p4164

mc16_13TeV.410644.PowhegPythia8EvtGen_A14_singletop_schan_lept_top.deriv.DAOD_HIGG3D1.e6527_s3126_r10724_p4164
mc16_13TeV.410645.PowhegPythia8EvtGen_A14_singletop_schan_lept_antitop.deriv.DAOD_HIGG3D1.e6527_s3126_r10724_p4164
mc16_13TeV.410645.PowhegPythia8EvtGen_A14_singletop_schan_lept_antitop.deriv.DAOD_HIGG3D1.e6527_s3126_r9364_p4164
mc16_13TeV.410648.PowhegPythia8EvtGen_A14_Wt_DR_dilepton_top.deriv.DAOD_HIGG3D1.e6615_s3126_r10724_p4164
mc16_13TeV.410649.PowhegPythia8EvtGen_A14_Wt_DR_dilepton_antitop.deriv.DAOD_HIGG3D1.e6615_s3126_r10724_p4164
mc16_13TeV.410658.PhPy8EG_A14_tchan_BW50_lept_top.deriv.DAOD_HIGG3D1.e6671_s3126_r10724_p4164
mc16_13TeV.410659.PhPy8EG_A14_tchan_BW50_lept_antitop.deriv.DAOD_HIGG3D1.e6671_s3126_r10724_p4164
mc16_13TeV.410659.PhPy8EG_A14_tchan_BW50_lept_antitop.deriv.DAOD_HIGG3D1.e6671_s3126_r9364_p4164

SM Higgs

mc16_13TeV.345120.PowhegPy8EG_NNLOPS_nnlo_30_ggH125_tautaul13l7.deriv.DAOD_HIGG3D1.e5814_s3126_r10724_p4164
mc16_13TeV.345121.PowhegPy8EG_NNLOPS_nnlo_30_ggH125_tautaulm15hp20.deriv.DAOD_HIGG3D1.e5814_s3126_r10724_p4164
mc16_13TeV.345122.PowhegPy8EG_NNLOPS_nnlo_30_ggH125_tautaulp15hm20.deriv.DAOD_HIGG3D1.e5814_s3126_r10724_p4164
mc16_13TeV.345123.PowhegPy8EG_NNLOPS_nnlo_30_ggH125_tautauh30h20.deriv.DAOD_HIGG3D1.e5814_s3126_r10724_p4164
mc16_13TeV.345211.PowhegPy8EG_NNPDF30_AZNLO_WmH125J_Winc_MINLO_tautau.deriv.DAOD_HIGG3D1.e5808_s3126_r10724_p4164
mc16_13TeV.345212.PowhegPy8EG_NNPDF30_AZNLO_WpH125J_Winc_MINLO_tautau.deriv.DAOD_HIGG3D1.e5808_s3126_r10724_p4164
mc16_13TeV.345217.PowhegPy8EG_NNPDF30_AZNLO_ZH125J_Zinc_MINLO_tautau.deriv.DAOD_HIGG3D1.e5808_s3126_r10724_p4164
mc16_13TeV.345324.PowhegPythia8EvtGen_NNLOPS_NN30_ggH125_WW1v1v_EF_15_5.deriv.DAOD_HIGG3D1.e5769_s3126_r10724_p4166
mc16_13TeV.345948.PowhegPy8EG_NNPDF30_AZNLOCTEQ6L1_VBFH125_WW1v1v.deriv.DAOD_HIGG3D1.e7172_s3126_r10724_p4166
mc16_13TeV.346190.PowhegPy8EG_NNPDF30_AZNLOCTEQ6L1_VBFH125_tautaul13l7.deriv.DAOD_HIGG3D1.e7259_s3126_r10724_p4164

B. Additional plots and event numbers for the Fake Factor estimation

This section contains all ncessary Plots and the corresponding event numbers used for the fake factor estimation.

Region	SR m_A=(20-70) GeV	SR m_A=(80-90) GeV	$Z \rightarrow \tau\tau$-CR	Top-CR
$Z \rightarrow \tau\tau$	122	477	9084	148
Top	35	204	1438.36	2154
Wlnu	25	144	8690	130
Diboson	12	64	578	20
SM Higgs	6	38	635	10
$Z \rightarrow ee/\mu\mu$	4	75	878	31
Sum	205	1002	21303	2494
Data	647	3551	36373	3685

Table B.1.: Event-numbers in the A-region used for FF estimation

Region	SR m_A=(20-70) GeV	SR m_A=(80-90) GeV	$Z \rightarrow \tau\tau$-CR	Top-CR
$Z \rightarrow \tau\tau$	39	111	3076	35
Top	11	49	378	486
$W \rightarrow l\nu$	9	69	3120	57
Diboson	3	17	173	5
SM Higgs	1	8	189	2
$Z \rightarrow ee/\mu\mu$	8	47	382	22
Sum	72	302	7318	607
Data	1449	7201	41283	3138

Table B.2.: Event-numbers in the B-region used for FF estimation

Region	SR m_A=(20-70) GeV	SR m_A=(80-90) GeV	$Z \to \tau\tau$-CR	Top-CR
$Z \to \tau\tau$	364	1431	22203	324
Top	41	232	1734	3570
$W \to l\nu$	131	539	18330	148
Diboson	27	131	1240	36
SM Higgs	16	92	1302	20
$Z \to ee/\mu\mu$	15	148	1719	63
Sum	594	2573	46528	4161
Data	1046	5619	61242	5613

Table B.3.: Event-numbers in the C-region used for FF estimation
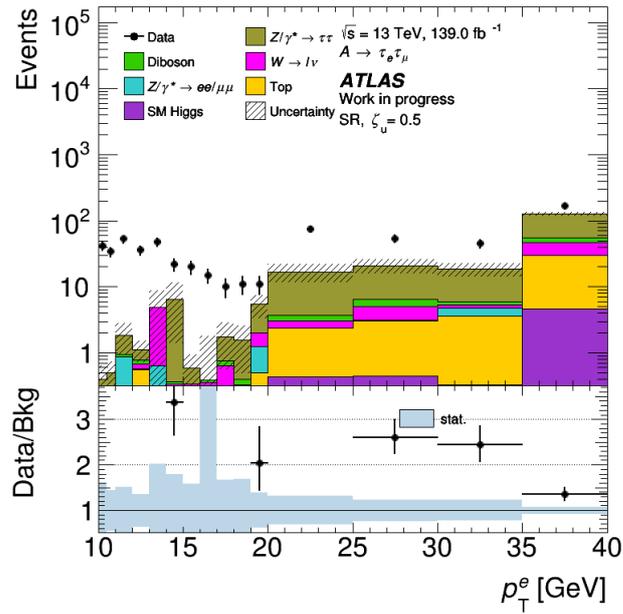
Figure B.1.: A region of the signal region for A masses of 40, 50, 60 and 70 GeV
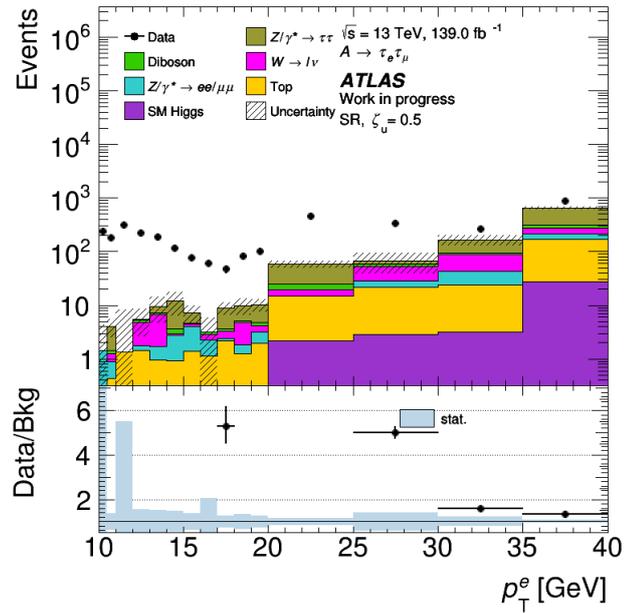
Figure B.2.: A region of the signal region for A masses of 70 and 90 GeV
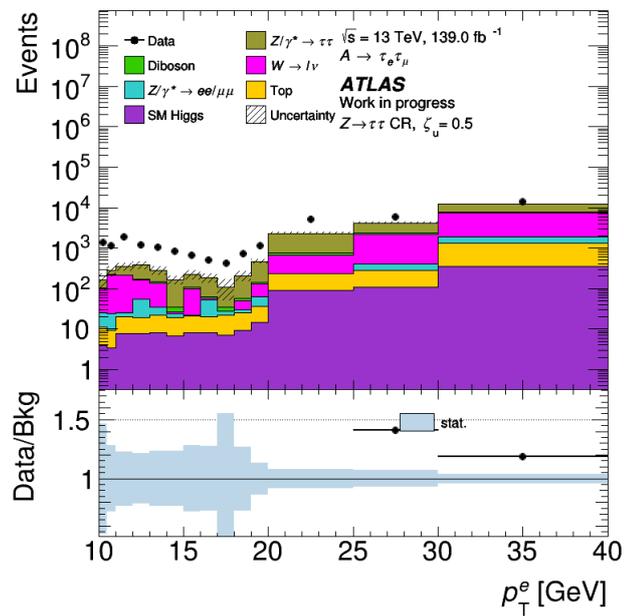
Figure B.3.: A region of the $Z \to \tau\tau$-CR
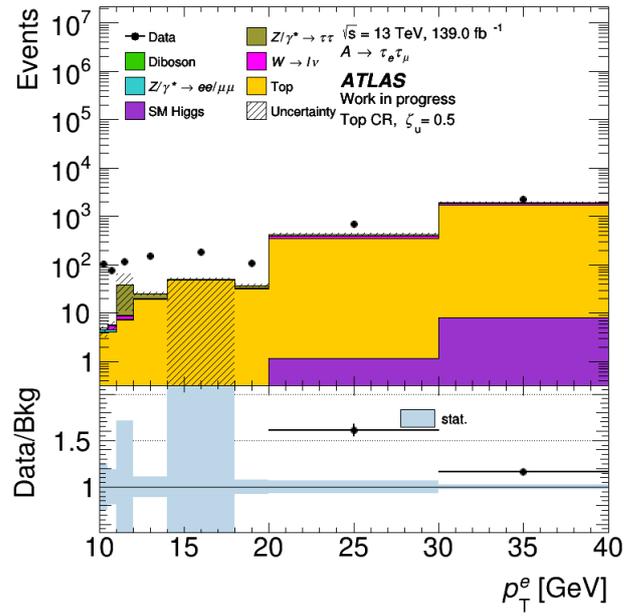
Figure B.4.: A region of the TOP-CR
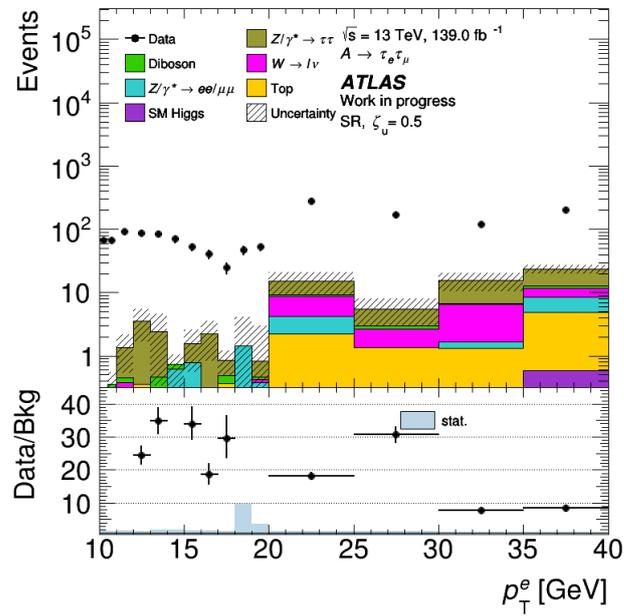
Figure B.5.: B region of the signal region for A masses of 40, 50, 60 and 70 GeV
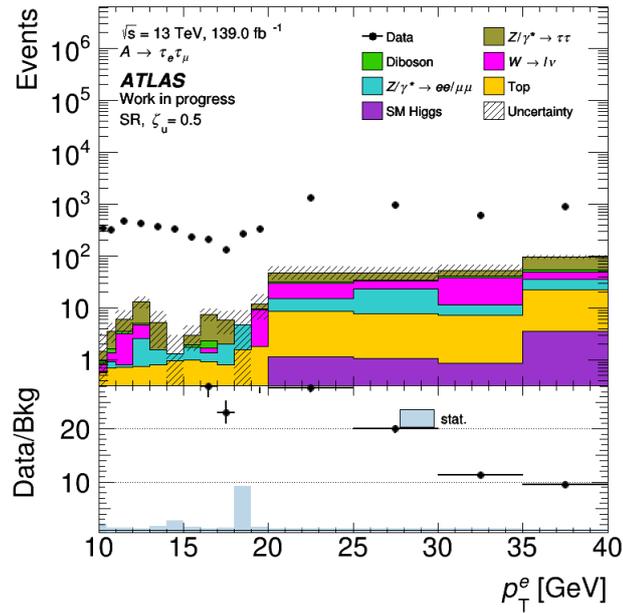
Figure B.6.: B region of the signal region for A masses of 70 and 90 GeV
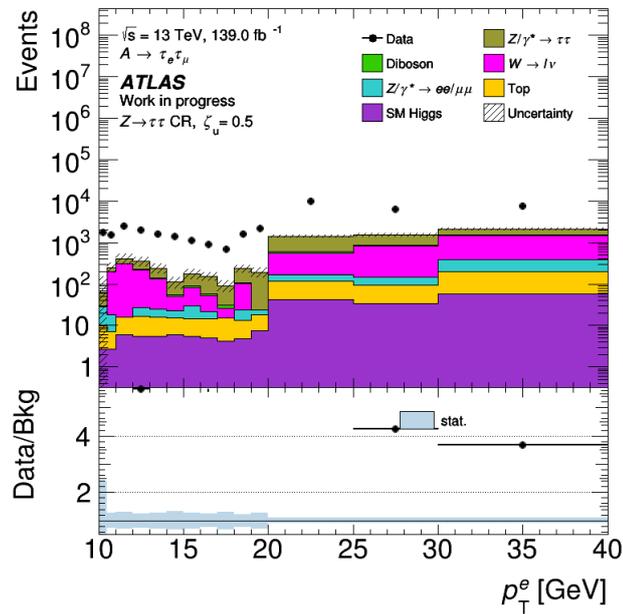
Figure B.7.: B region of the $Z \rightarrow \tau\tau$-CR
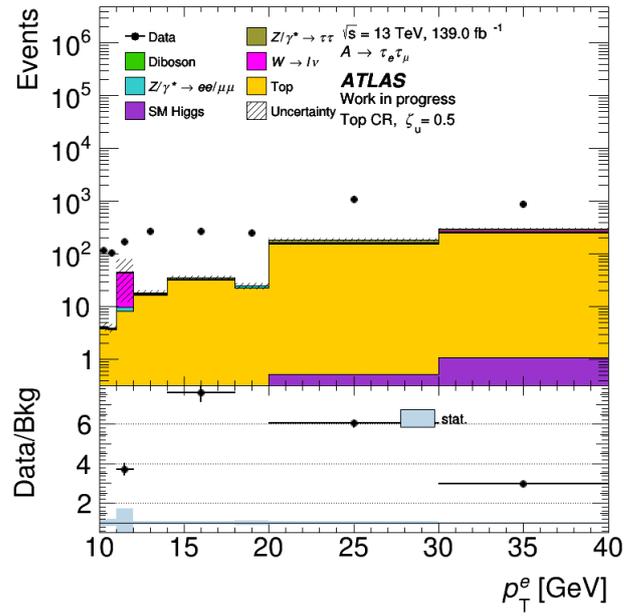
Figure B.8.: B region of the TOP-CR
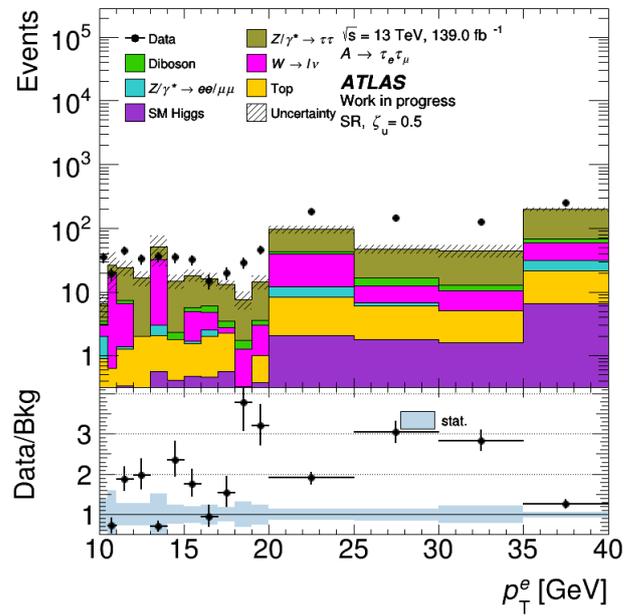
Figure B.9.: C region of the signal region for A masses of 40, 50, 60 and 70 GeV
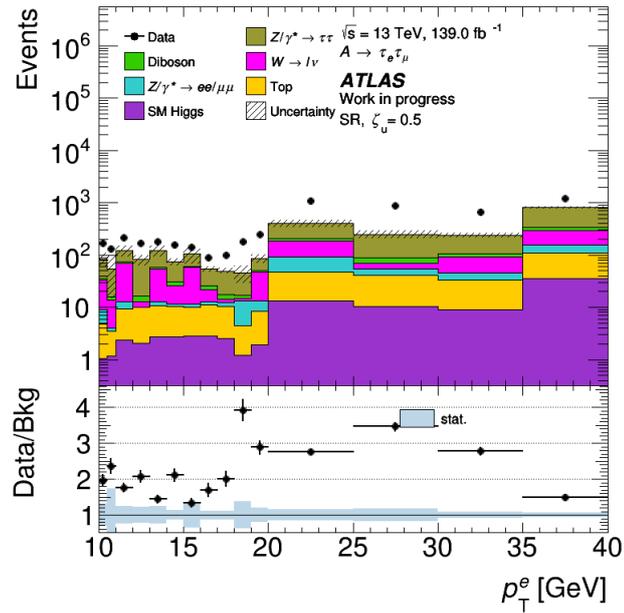
Figure B.10.: C region of the signal region for A masses of 70 and 90 GeV
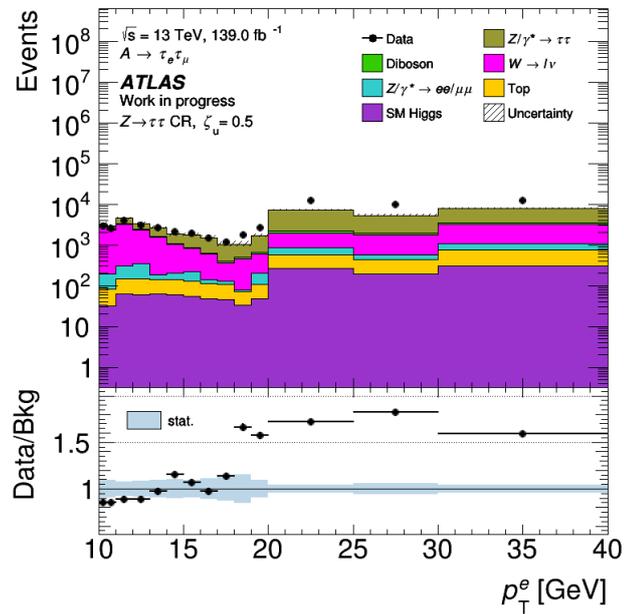
Figure B.11.: C region of the $Z \to \tau\tau$-CR
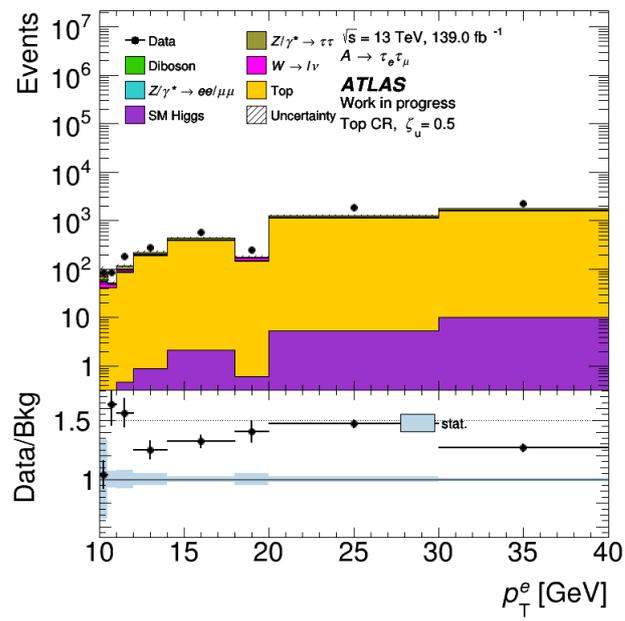
Figure B.12.: C region of the TOP-CR

C. Additional PNN score plots
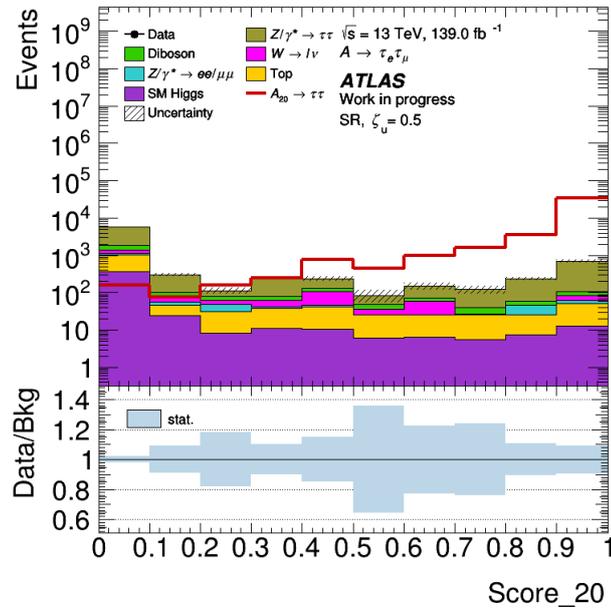
Figure C.1.: Score of the PNN with the mass parameter set to $m_A = 20\,\text{GeV}$ in the signal region
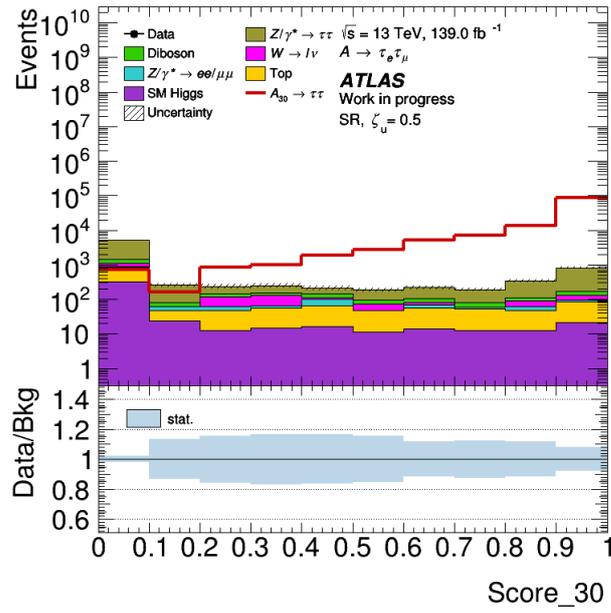
Figure C.2.: Score of the PNN with the mass parameter set to $m_A = 30\,\mathrm{GeV}$ in the signal region
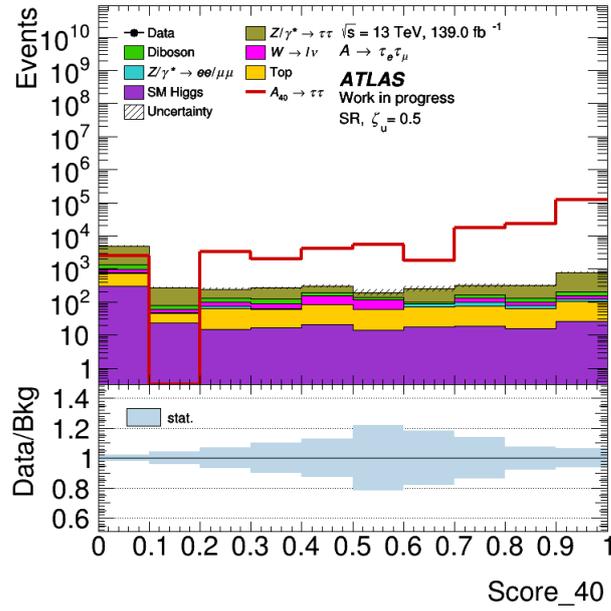
Figure C.3.: Score of the PNN with the mass parameter set to $m_A = 40\,\mathrm{GeV}$ in the signal region
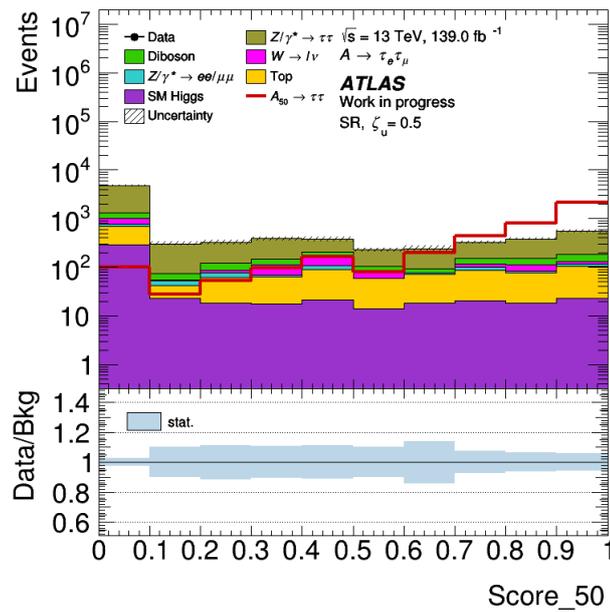
Figure C.4.: Score of the PNN with the mass parameter set to $m_A = 50\,\text{GeV}$ in the signal region
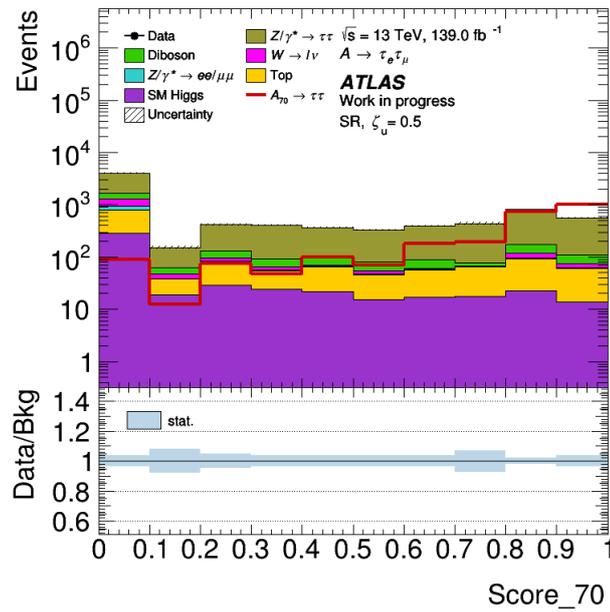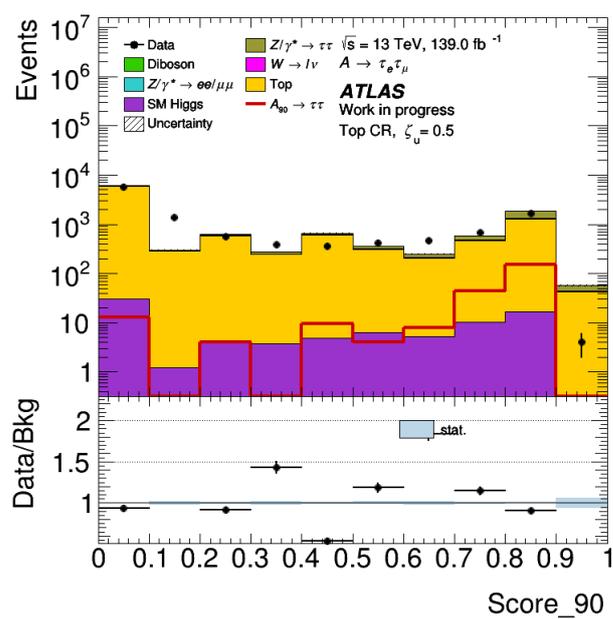

Figure C.5.: Score of the PNN with the mass parameter set to $m_A = 70\,\text{GeV}$ in the signal region
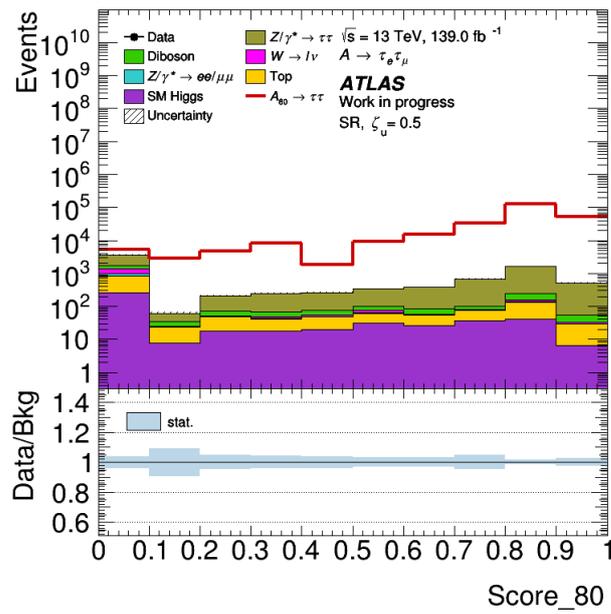
Figure C.6.: Score of the PNN with the mass parameter set to $m_A = 80\,\text{GeV}$ in the signal region
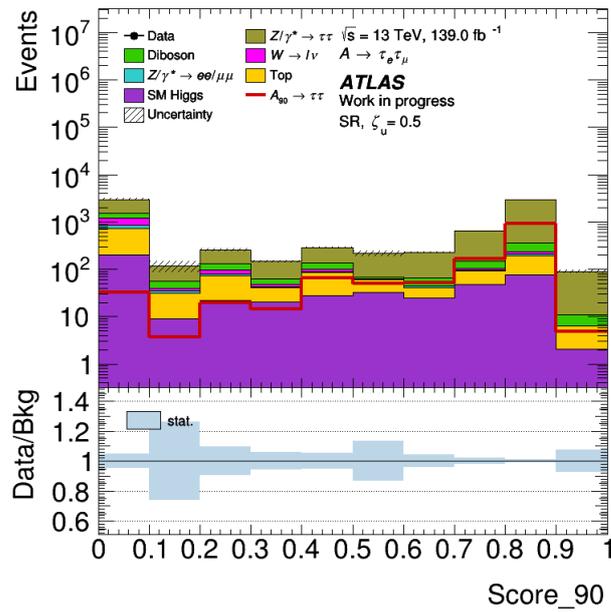
Figure C.7.: Score of the PNN with the mass parameter set to $m_A = 90\,\text{GeV}$ in the signal region
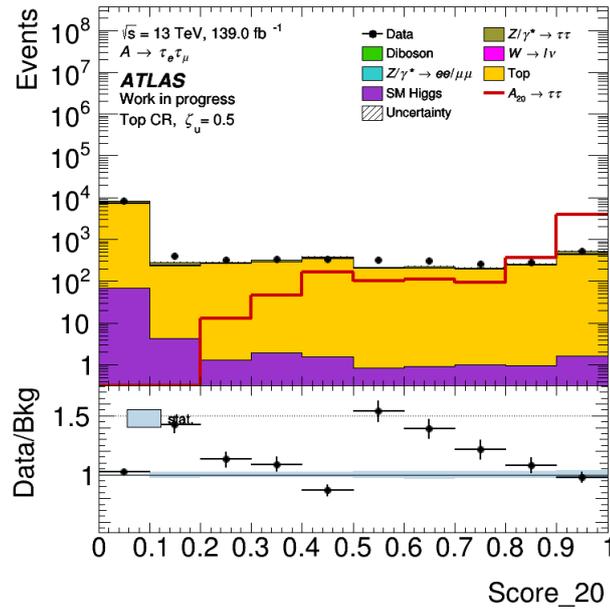
Figure C.8.: Score of the PNN with the mass parameter set to $m_A = 20\,\text{GeV}$ in the Top CR
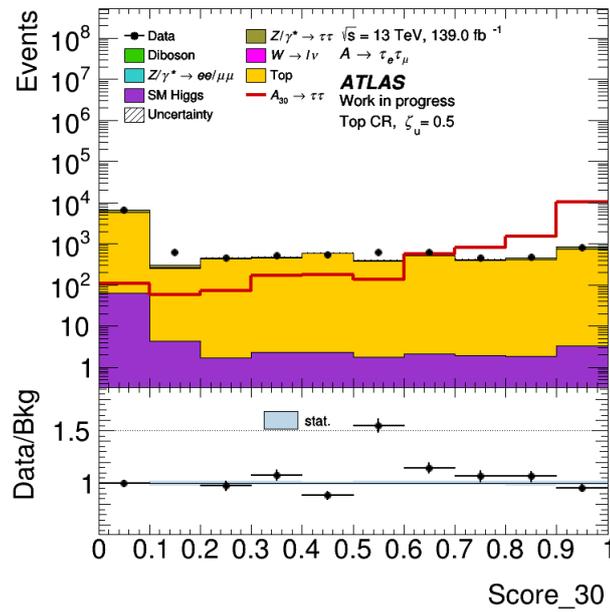
Figure C.9.: Score of the PNN with the mass parameter set to $m_A = 30\,\text{GeV}$ in the Top CR
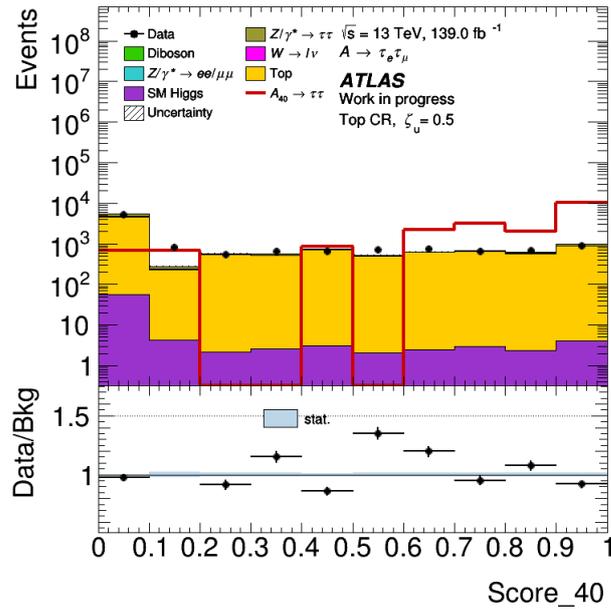
Figure C.10.: Score of the PNN with the mass parameter set to $m_A = 40\,\text{GeV}$ in the Top CR
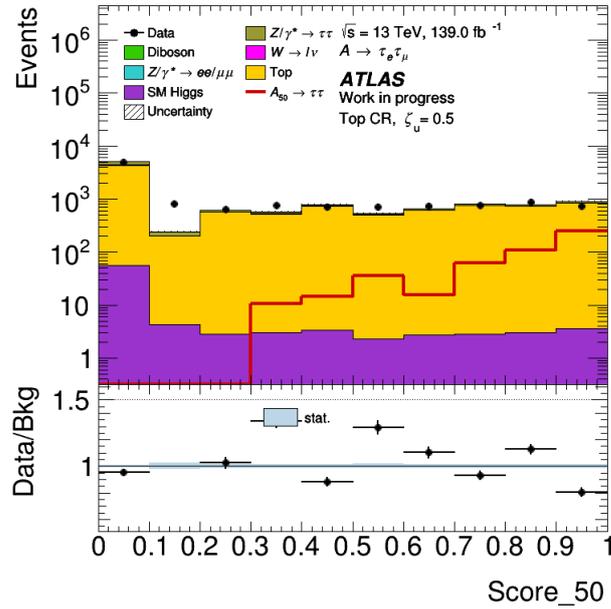
Figure C.11.: Score of the PNN with the mass parameter set to $m_A = 50\,\text{GeV}$ in the Top CR
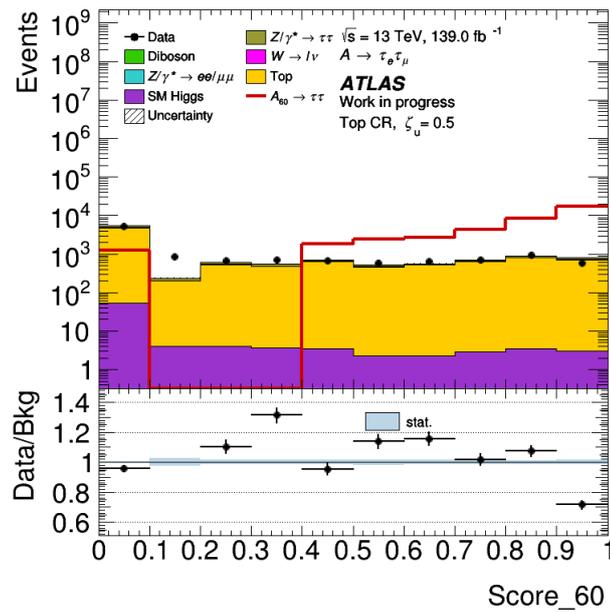
Figure C.12.: Score of the PNN with the mass parameter set to $m_A = 60\,\text{GeV}$ in the Top CR
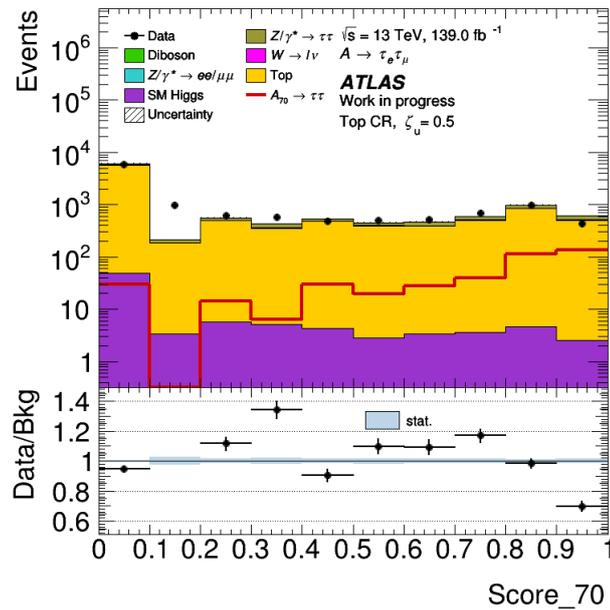
Figure C.13.: Score of the PNN with the mass parameter set to $m_A = 70\,\text{GeV}$ in the Top CR
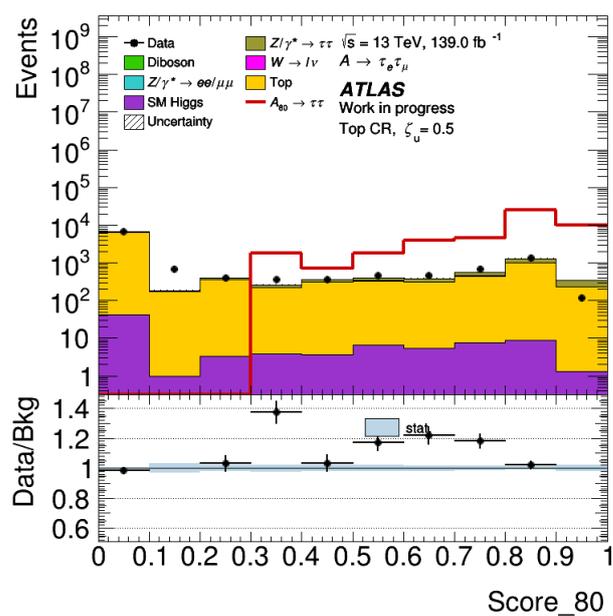
Figure C.14.: Score of the PNN with the mass parameter set to $m_A = 80\,\mathrm{GeV}$ in the Top CR

Figure C.15.: Score of the PNN with the mass parameter set to $m_A = 90\,\mathrm{GeV}$ in the Top CR
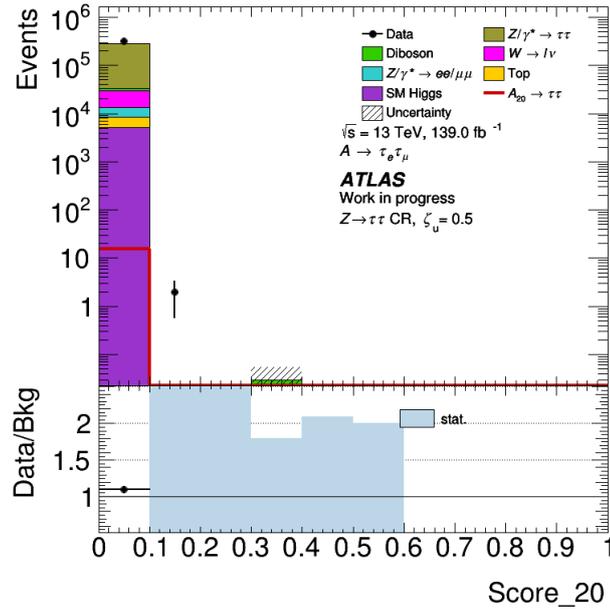
Figure C.16.: Score of the PNN with the mass parameter set to $m_A = 20\,\text{GeV}$ in the $Z \to \tau\tau$ CR
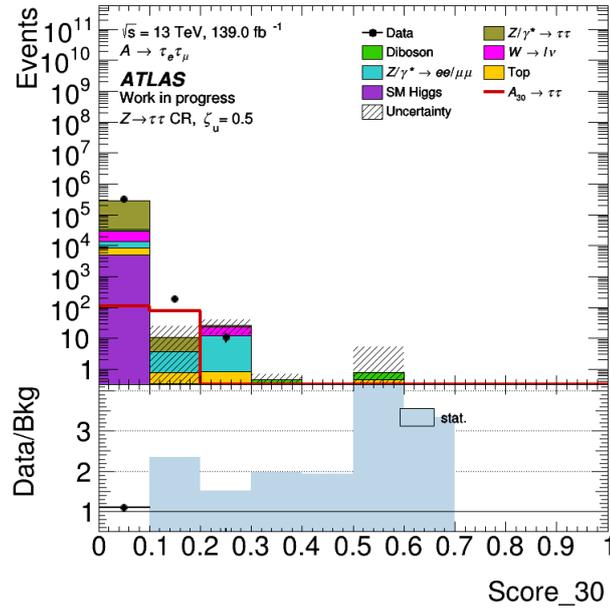
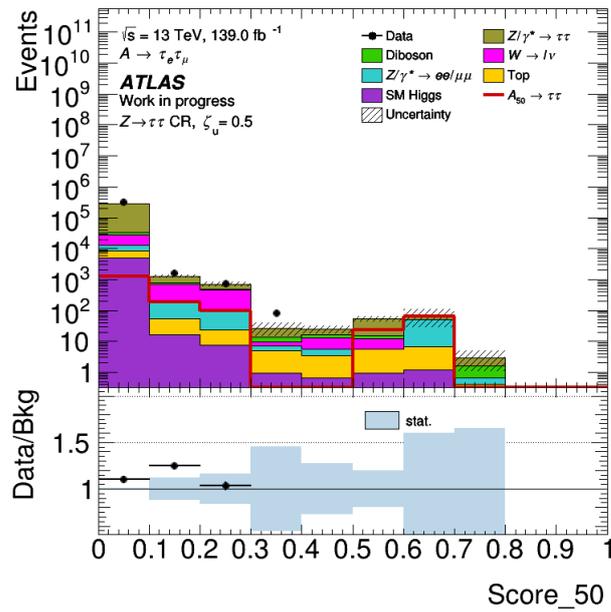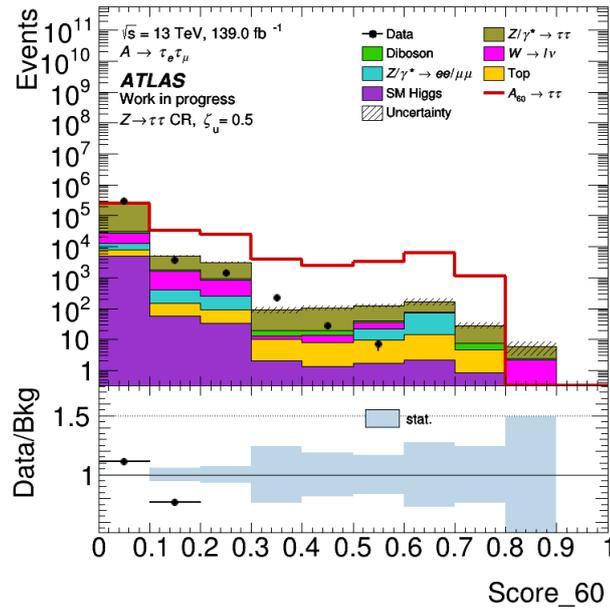Figure C.17.: Score of the PNN with the mass parameter set to $m_A = 30\,\text{GeV}$ in the $Z \to \tau\tau$ CR
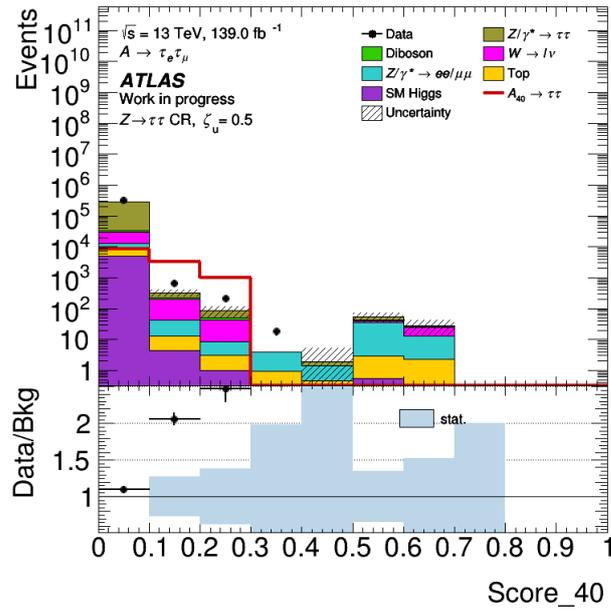
Figure C.18.: Score of the PNN with the mass parameter set to $m_A = 40\,\mathrm{GeV}$ in the $Z \to \tau\tau$ CR

Figure C.19.: Score of the PNN with the mass parameter set to $m_A = 50\,\mathrm{GeV}$ in the $Z \to \tau\tau$ CR

Figure C.20.: Score of the PNN with the mass parameter set to $m_A = 60\,\text{GeV}$ in the $Z \to \tau\tau$ CR
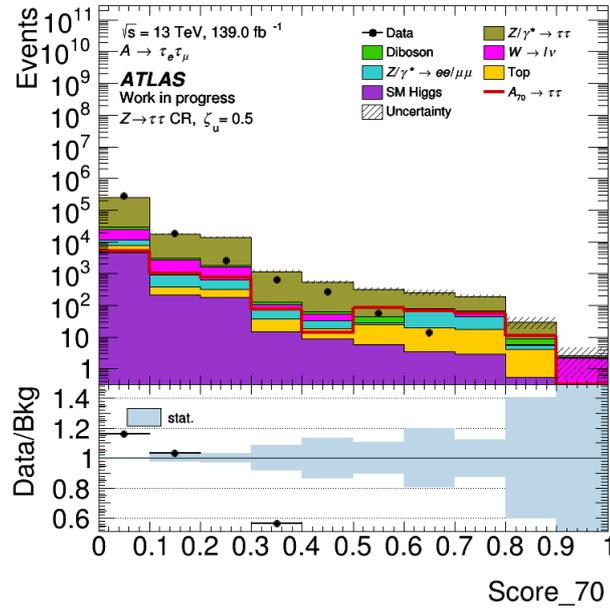

Figure C.21.: Score of the PNN with the mass parameter set to $m_A = 70\,\text{GeV}$ in the $Z \to \tau\tau$ CR
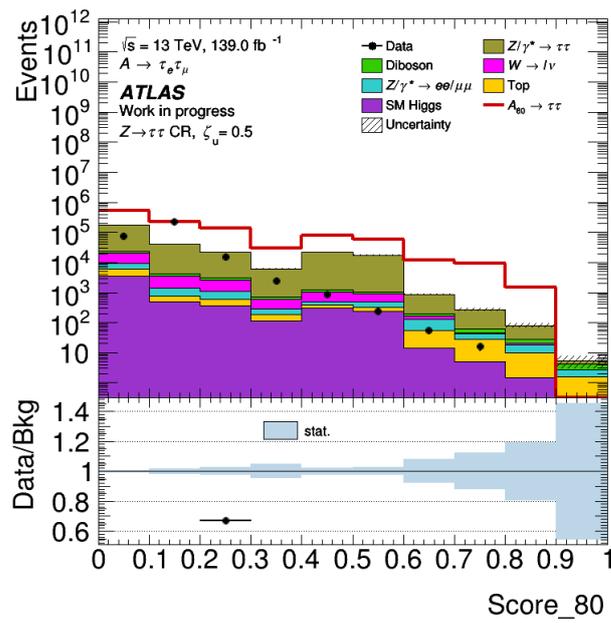
Figure C.22.: Score of the PNN with the mass parameter set to $m_A = 80\,\text{GeV}$ in the $Z \to \tau\tau$ CR
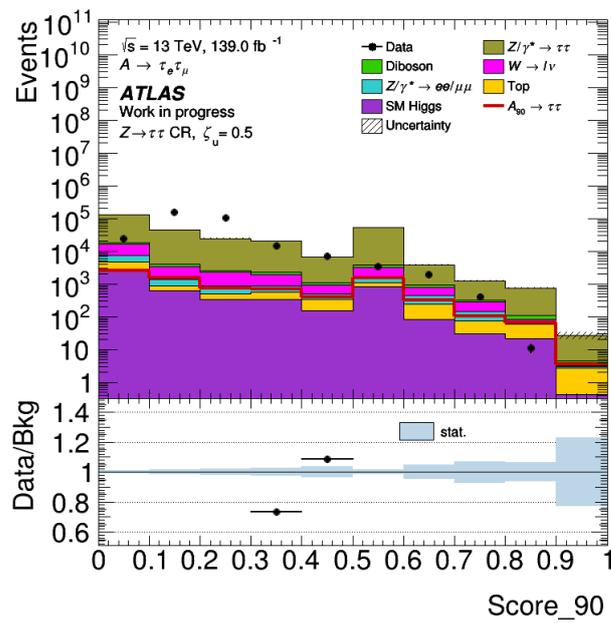

Figure C.23.: Score of the PNN with the mass parameter set to $m_A = 90\,\text{GeV}$ in the $Z \to \tau\tau$ CR

Bibliography

[1] J. J. T. M. F.R.S., "Xl. cathode rays," The London, Edinburgh, and Dublin Philosophical Magazine and Journal of Science **44**, 293 (1897).

[2] R. A. Millikan, "The isolation of an ion, a precision measurement of its charge, and the correction of stokes's law," Phys. Rev. (Series I) **32**, 349 (1911).

[3] S. H. Neddermeyer and C. D. Anderson, "Note on the nature of cosmic-ray particles," Phys. Rev. **51**, 884 (1937).

[4] M. L. Perl et al., "Evidence for anomalous lepton production in $e^+ - e^-$ annihilation," Phys. Rev. Lett. **35**, 1489 (1975).

[5] A. Einstein, "The foundation of the general theory of relativity," Annalen Phys. **49**, 769 (1916).

[6] J. Schwinger, "Quantum electrodynamics. i. a covariant formulation," Phys. Rev. **74**, 1439 (1948).

[7] S. Tomonaga, "On a Relativistically Invariant Formulation of the Quantum Theory of Wave Fields*," Progress of Theoretical Physics **1**, 27 (1946).

[8] R. P. Feynman, "Mathematical formulation of the quantum theory of electromagnetic interaction," Phys. Rev. **80**, 440 (1950).

[9] S. L. Glashow, "Partial-symmetries of weak interactions," Nuclear Physics **22**, 579 (1961).

[10] S. Weinberg, "A model of leptons," Phys. Rev. Lett. **19**, 1264 (1967).

[11] A. Salam, "Renormalizability of gauge theories," Phys. Rev. **127**, 331 (1962).

[12] G. Arnison et al., "Experimental observation of lepton pairs of invariant mass around 95 gev/c2 at the cern sps collider," Physics Letters B **126**, 398 (1983).

[13] M. Banner et al., "Observation of single isolated electrons of high transverse momentum in events with missing transverse energy at the cern pp collider," Physics Letters B **122**, 476 (1983).

[14] P. W. Higgs, "Broken symmetries and the masses of gauge bosons," Phys. Rev. Lett. **13**, 508 (1964).

[15] F. Englert and R. Brout, "Broken symmetry and the mass of gauge vector mesons," Phys. Rev. Lett. **13**, 321 (1964).

[16] S. Weinberg, "Non-abelian gauge theories of the strong interactions," Phys. Rev. Lett. **31**, 494 (1973).

[17] H. Fritzsch et al., "Advantages of the color octet gluon picture," Physics Letters B **47**, 365 (1973).

[18] Paul Moder, "search for a light cp-odd higgs boson decaying into a $\tau\tau$ pair," MA thesis (TU Dresden, Germany, 2018).

[19] Tom Kresse, "search for a light cp-odd higgs boson decaying into a pair of τ-leptons with the atlas detector," MA thesis (TU Dresden, Germany, 2020).

[20] Xynia-Magdalena Sonntag, "optimized search for alight cp-odd higgs boson decaying into two τ-leptons using the atlas detector," MA thesis (TU Dresden, Germany, 2021).

[21] M. Gell-Mann, "A schematic model of baryons and mesons," Physics Letters **8**, 214 (1964).

[22] G. Zweig, "An su(3) model for stron interacction symmetry and its breaking," Physical Review 80 (1964).

[23] J. Schwinger, "Quantum electrodynamics. i. a covariant formulation," Physical Review 74 (1948).

[24] R. Feynman, "On a relativistically invariant formulation of the quantum theory of wave fields," Progress of Theoretical Physics 1 (1950).

[25] S. Tomonaga, "Mathematical formulation of the quantum theory of electromagnetic interaction," Physical Review 80 (1946).

[26] A. Salam and J. Ward, "Electromagnetic and weak interactions," Physics Letters **13**, 168 (1964).

[27] P. Langacker, "Introduction to the standard model and electroweak physics," in The dawn of the LHC era (Aug. 2010).

[28] W. N. Cottingham and D. A. Greenwood, *An introduction to the standard model of particle physics*, 2nd ed. (Cambridge University Press, 2007).

[29] *Standard model*, `https://www.physik.uzh.ch/en/researcharea/lhcb/outreach/StandardModel.html`.

[30] P. Langacker, "Introduction to the standard model and electroweak physics," in *The dawn of the lhc era* (), pp. 3–48.

[31] A. Djouadi, "The anatomy of electroweak symmetry breaking: tome i: the higgs boson in the standard model," Physics Reports **457**, 1 (2008).

[32] P. D. Group et al., "Review of Particle Physics," Progress of Theoretical and Experimental Physics **2020**, 083C01, `10.1093/ptep/ptaa104` (2020).

[33] J. Ellis, *Higgs physics*, 2013.

[34] B. Abi et al., "Measurement of the positive muon anomalous magnetic moment to 0.46 ppm," Physical Review Letters **126**, `10.1103/physrevlett.126.141801` (2021).

[35] H. Haber and G. Kane, "The search for supersymmetry: probing physics beyond the standard model," Physics Reports **117**, 75 (1985).

[36] L. Fromme et al., "Baryogenesis in the two-higgs doublet model," Journal of High Energy Physics **2006**, 038 (2006).

[37] G. Branco et al., "Theory and phenomenology of two-higgs-doublet models," Physics Reports **516**, 1 (2012).

[38] I. Chakraborty and A. Kundu, "Two-higgs doublet models confront the naturalness problem," Physical Review D **90**, `10.1103/physrevd.90.115017` (2014).

[39] A. Cherchiglia et al., "Muon $g - 2$ in the 2hdm: maximum results and detailed phenomenology," Physical Review D **98**, `10.1103/physrevd.98.035001` (2018).

[40] A. Pich and P. Tuzón, "Yukawa alignment in the two-higgs-doublet model," Physical Review D **80**, `10.1103/physrevd.80.091702` (2009).

[41] J. F. Gunion and H. E. Haber, "Cp-conserving two-higgs-doublet model: the approach to the decoupling limit," Phys. Rev. D **67**, 075019 (2003).

[42] E. J. Chun and J. Kim, "Leptonic precision test of leptophilic two-higgs-doublet model," Journal of High Energy Physics **2016**, `10.1007/jhep07(2016)110` (2016).

[43] "Searches for neutral higgs bosons in extended models," The European Physical Journal C **38**, 1 (2004).

[44] S. Chatrchyan et al., "Search for neutral higgs bosons decaying to tau pairs in pp collisions at $\sqrt{s} = 7$ tev," Physics Letters B **713**, 68 (2012).

[45] G. Cowan et al., "Asymptotic formulae for likelihood-based tests of new physics," The European Physical Journal C **71**, `10.1140/epjc/s10052-011-1554-0` (2011).

[46] S. S. Wilks, "The Large-Sample Distribution of the Likelihood Ratio for Testing Composite Hypotheses," The Annals of Mathematical Statistics **9**, 60 (1938).

[47] A. Wald, "Tests of statistical hypotheses concerning several parameters when the number of observations is large," Transactions of the American Mathematical Society **54**, 426 (1943).

[48] A. L. Read, "Presentation of search results: the CL_s technique," Journal of Physics G: Nuclear and Particle Physics **28**, 2693 (2002).

[49] I. Asimov, *The complete stories*, 1990.

[50] L. Evans and P. Bryant, "LHC machine," Journal of Instrumentation **3**, S08001 (2008).

[51] A. Collaberation, *The cern accelerator complex*, `https://cds.cern.ch/images/OPEN-PHO-ACCEL-2013-056-1`.

[52] T. ATLAS-Collaboration, *Physics at a High-Luminosity LHC with ATLAS*, tech. rep., All figures including auxiliary figures are available at https://atlas.web.cern.ch/Atlas/GROUPS/PHYSICS/PUBNOTES/ATL-PHYS-PUB-2012-001 (CERN, Geneva, 2012).

[53] T. C. Collaboration et al., "The CMS experiment at the CERN LHC," Journal of Instrumentation **3**, S08004 (2008).

[54] T. L. Collaboration et al., "The LHCb detector at the LHC," Journal of Instrumentation **3**, S08005 (2008).

[55] T. T. Collaboration et al., "The TOTEM experiment at the CERN large hadron collider," Journal of Instrumentation **3**, S08007 (2008).

[56] T. A. Collaboration et al., "The ALICE experiment at the CERN LHC," Journal of Instrumentation **3**, S08002 (2008).

[57] G. Aad et al., "Observation of a new particle in the search for the standard model higgs boson with the ATLAS detector at the LHC," Physics Letters B **716**, 1 (2012).

[58] T. A. Collaboration et al., "The ATLAS experiment at the CERN large hadron collider," Journal of Instrumentation **3**, S08003 (2008).

[59] M. Aaboud et al., "Study of the material of the ATLAS inner detector for run 2 of the LHC," Journal of Instrumentation **12**, P12009 (2017).

[60] K. Potamianos, "The upgraded pixel detector and the commissioning of the inner detector tracking of the atlas experiment for run-2 at the large hadron collider," `10.48550/ARXIV.1608.07850` (2016).

[61] B. Mandelli, "The pixel detector of the atlas experiment for the run 2 at the large hadron collider," Nuclear and Particle Physics Proceedings **273-275**, 37th International Conference on High Energy Physics (ICHEP), 1166 (2016).

[62] J. R. Pater, "The ATLAS SemiConductor tracker operation and performance," Journal of Instrumentation **7**, C04001 (2012).

[63] M. Aaboud et al., "Performance of the ATLAS transition radiation tracker in run 1 of the LHC: tracker properties," Journal of Instrumentation **12**, P05002 (2017).

[64] *ATLAS liquid-argon calorimeter: Technical Design Report*, Technical design report. ATLAS (CERN, Geneva, 1996).

[65] H. Wilkens and the ATLAS LArg Collaboration, "The ATLAS liquid argon calorimeter: an overview," Journal of Physics: Conference Series **160**, 012043 (2009).

[66] P. K. and, "Calibration and performance of the ATLAS tile calorimeter during the LHC run 2," Journal of Physics: Conference Series **1162**, 012003 (2019).

[67] T. A. collaboration, "Operation of the ATLAS trigger system in run 2," Journal of Instrumentation **15**, P10004 (2020).

[68] *Atlas experiment - public results*, (Sept. 2022) `https://twiki.cern.ch/twiki/bin/view/AtlasPublic/LuminosityPublicResultsRun2`.

[69] T. Sjöstrand, *Monte carlo generators*, 2006.

[70] M. H. Seymour and M. Marx, *Monte carlo event generators*, 2013.

[71] Z. M. and, "Simulation of pile-up in the ATLAS experiment," Journal of Physics: Conference Series **513**, 022024 (2014).

[72] C. Oleari, "The POWHEG BOX," Nuclear Physics B - Proceedings Supplements **205-206**, 36 (2010).

[73] T. Sjöstrand et al., "An introduction to PYTHIA 8.2," Computer Physics Communications **191**, 159 (2015).

[74] E. Bothmann et al., "Event generation with sherpa 2.2," SciPost Physics **7**, `10.21468/scipostphys.7.3.034` (2019).

[75] S. Amoroso et al., *PMG references document*, tech. rep. (CERN, Geneva, 2019).

[76] M. Kobayashi and T. Maskawa, "CP-Violation in the Renormalizable Theory of Weak Interaction," Progress of Theoretical Physics **49**, 652 (1973).

[77] T. Müller, "Preparations for the spin and parity measurement of the higgs boson in the $H \rightarrow \tau\tau$ channel," (2014).

[78] W. Lampl et al., *Calorimeter Clustering Algorithms: Description and Performance*, tech. rep., All figures including auxiliary figures are available at https://atlas.web.cern.ch/Atlas/GROUPS/PHYSICS/PUBNOTES/ATL-LARG-PUB-2008-002 (CERN, Geneva, 2008).

[79] M. Aaboud et al., "Electron reconstruction and identification in the ATLAS experiment using the 2015 and 2016 LHC proton–proton collision data at $\sqrt{s} = 13$ TeV," The European Physical Journal C **79**, `10.1140/epjc/s10052-019-7140-6` (2019).

[80] G. Aad et al., "Muon reconstruction performance of the ATLAS detector in proton–proton collision data at $\sqrt{s} = 13$ TeV," The European Physical Journal C **76**, `10.1140/epjc/s10052-016-4120-y` (2016).

[81] A. Hrynevich, "ATLAS jet and missing energy reconstruction, calibration and performance in LHC run-2," Journal of Instrumentation **12**, C06038 (2017).

[82] M. Cacciari et al., "The anti-k_t jet clustering algorithm," Journal of High Energy Physics **2008**, 063 (2008).

[83] *Identification of Jets Containing b-Hadrons with Recurrent Neural Networks at the ATLAS Experiment*, tech. rep., All figures including auxiliary figures are available at https://atlas.web.cern.ch/Atlas/GROUPS/PHYSICS/PUB-NOTES/ATL-PHYS-PUB-2017-003 (CERN, Geneva, 2017).

[84] Connelly, Ian, "Performance and calibration of b-tagging with the atlas experiment at lhc run-2," EPJ Web Conf. **164**, 07025 (2017).

[85] J. Montejo, *Lowest un-prescaled triggers per data-taking period*, (2021) `https://twiki.cern.ch/twiki/bin/viewauth/Atlas/LowestUnprescaled`.

[86] K. Nagano, *Trigger naming run 2*, (2019) `https://twiki.cern.ch/twiki/bin/viewauth/Atlas/TriggerNamingRun2`.

[87] G. Aad et al., "Electron and photon performance measurements with the ATLAS detector using the 2015–2017 LHC proton-proton collision data," Journal of Instrumentation **14**, P12006 (2019).

[88] M. Maerker, "Search for heavy neutral Higgs bosons decaying into the fully hadronic di-tau final state with ATLAS," (2022).

[89] J. H. Friedman, "Data analysis techniques for high energy particle physics," 96 p (1974).

[90] I. Goodfellow et al., *Deep learning*, `http://www.deeplearningbook.org` (MIT Press, 2016).

[91] M. A. Nielsen, "Neural Networks and Deep Learning," (2015).

[92] D. P. Kingma and J. Ba, *Adam: a method for stochastic optimization*, 2014.

[93] Ludwig Zschuppe, "Neural Networks for the search of heavy Higgs bosons $H/A \to \tau_{\text{had}}\tau_{\text{had}}$," MA thesis (TU Dresden, Germany, 2020).

[94] S. Chatrchyan et al., "Observation of a new boson at a mass of 125 GeV with the CMS experiment at the LHC," Physics Letters B **716**, 30 (2012).

[95] Y. Nakahama, "The ATLAS trigger system: ready for run-2," Journal of Physics: Conference Series **664**, 082037 (2015).

Acknowledgements

Erklärung

Hiermit erkläre ich, dass ich die vorliegende Arbeit im Rahmen der Betreuung am Institut für Kern- und Teilchenphysik ohne unzulässige Hilfe Dritter verfasst habe und alle verwendeten Quellen als solche gekennzeichnet habe.

_____

Ort, Datum   Unterschrift